



HAL
open science

Design and fabrication of a compact gas sensor integrating a polymer micro resonator and a 850nm VCSEL source

Qingyue Li

► **To cite this version:**

Qingyue Li. Design and fabrication of a compact gas sensor integrating a polymer micro resonator and a 850nm VCSEL source. Micro and nanotechnologies/Microelectronics. Université Paul Sabatier - Toulouse III, 2021. English. NNT : 2021TOU30048 . tel-03299372v2

HAL Id: tel-03299372

<https://laas.hal.science/tel-03299372v2>

Submitted on 4 Oct 2021

HAL is a multi-disciplinary open access archive for the deposit and dissemination of scientific research documents, whether they are published or not. The documents may come from teaching and research institutions in France or abroad, or from public or private research centers.

L'archive ouverte pluridisciplinaire **HAL**, est destinée au dépôt et à la diffusion de documents scientifiques de niveau recherche, publiés ou non, émanant des établissements d'enseignement et de recherche français ou étrangers, des laboratoires publics ou privés.



THÈSE

**En vue de l'obtention du
DOCTORAT DE L'UNIVERSITÉ DE TOULOUSE
Délivré par l'Université Toulouse 3 - Paul Sabatier**

Présentée et soutenue par

Qingyue LI

Le 24 juin 2021

**Conception et fabrication d'un capteur de gaz compact intégrant
un micro résonateur polymère et une source VCSEL 850nm**

Ecole doctorale : **GEETS - Génie Electrique Electronique, Télécommunications et
Santé : du système au nanosystème**

Spécialité : **MicroNano Systèmes**

Unité de recherche :

LAAS - Laboratoire d'Analyse et d'Architecture des Systèmes

Thèse dirigée par

Philippe MENINI et Vincent RAIMBAULT

Jury

Mme Virginie NAZABAL, Rapporteur

Mme Aurore VICET, Rapporteur

Mme Hélène TAP, Examinatrice

M. Olivier SOPPERA, Examineur

M. Philippe MENINI, Directeur de thèse

M. Vincent RAIMBAULT, Co-directeur de thèse

Special thanks to Pr. Véronique BARDINAL for her selfless guidance and great contribution to this work.

Résumé

Il existe une demande croissante en capteurs de gaz portables, émanant à la fois des sciences de l'environnement, de la santé ainsi que de l'industrie. Les capteurs optiques résonants, en particulier les micro résonateurs planaires, combinent forte sensibilité et faibles dimensions, ce qui en fait de bons candidats pour ces applications. Le principe de détection de ces capteurs à champ évanescent est basé sur une variation de leur réponse optique liée à une modification de l'indice effectif en présence des molécules cibles. Si de nombreux travaux montrent l'efficacité de cette approche, sa mise en œuvre aux dimensions sub-microniques passe par l'emploi de bancs optiques complexes, encombrants, et difficilement miniaturisables.

Nous proposons ici une approche globale basée sur l'ensemble du système de mesure, en exploitant des compétences pluridisciplinaires sur (i) les diodes à cavité verticales émettant par la surface (VCSEL) et la mise en forme de leur faisceau ; (ii) la conception et la fabrication de micro résonateurs optiques polymères et de réseaux de couplage ; (iii) les capteurs de gaz et la fonctionnalisation de surface. L'utilisation d'un VCSEL accordable en courant sur 5nm, combinée à une mise en forme du faisceau et l'emploi de réseaux de couplage, permet d'obtenir une meilleure tolérance au désalignement entre la source et l'entrée du guide d'ondes, et simplifier ainsi l'injection de lumière. Un couplage vertical du micro-résonateur est favorisé pour faciliter le dépôt de la couche sensible et isoler les réseaux de couplage et les guides d'ondes. La longueur d'onde de 850 nm ne permettant pas une détection directe de l'absorption des molécules de gaz d'intérêt, une couche sensible de polyaniline (PANI) est ajoutée afin d'apporter sélectivité et sensibilité à l'ammoniac (NH_3). Son exposition au NH_3 entraîne un dédopage, réversible à température ambiante, qui se traduit par des modifications de son indice optique et une variation du spectre de résonance en sortie du micro-résonateur mesurable à l'aide d'une simple photodiode grâce à l'accordabilité de la source. La compacité et l'intégrabilité des micro-résonateurs, des sources VCSELs et des photodétecteurs permet d'envisager des matrices de micro-résonateurs fonctionnalisés pour une détection multi-cibles.

Le manuscrit débute par une présentation globale du microsysteme et son positionnement par rapport à l'état de l'art. L'intérêt des matériaux et technologies polymères est discuté pour réaliser un système « lab-on-chip » à faible coût, en se basant sur nos travaux antérieurs et nos contraintes technologiques. L'intégration d'éléments micro-optiques polymères sur VCSEL est théoriquement et expérimentalement étudiée pour obtenir une collimation et une taille de spot appropriées pour la distance de travail considérée, afin de diminuer sa divergence naturelle et maximiser le couplage. Deux méthodes post-production sont employées, discutées et comparées : une méthode basée sur la lithographie laser et le dépôt par jet d'encre, et une méthode 3D par stéréolithographie 2-photons. Une étude de dimensionnement basée sur du calcul analytique et de la modélisation FDTD incluant

les contraintes technologiques est présentée pour concevoir les réseaux de couplage, les guides d'ondes et les micro-résonateurs. L'intégration d'un photodétecteur silicium est discutée pour réaliser une intégration complète. Ensuite, plusieurs approches technologiques sont présentées pour créer la structure conçue dans la section technologie et fabrication. Les plates-formes de caractérisation optique permettant l'évaluation des performances de chacun des éléments du microsysteme sont détaillées. Les résultats préliminaires sont présentés et de nouvelles pistes sont proposées. Enfin, l'intégration d'un matériau chimiquement sensible à la surface du matériau guide d'ondes est développée et testée. Les perspectives de recherches futures sont également discutées.

Mots clés : Capteur du gaz ; détection optique ; résonateur en anneau ; polymère ; SU-8 ; impression en 3D ; VCSEL ; proche infra-rouge

Abstract

There is a growing demand for portable gas sensors, from both environmental and health sciences as well as the industry. Resonant optical sensors, in particular planar micro resonators, combine high sensitivity and small dimensions, which makes them good candidates for these applications. The sensing principle of these evanescent field sensors is based on a variation in their optical response linked to a modification of the effective index in the presence of the target molecules. While many studies show the effectiveness of this approach, its implementation on sub-micron dimensions requires the use of complex optical benches, bulky, and difficult to miniaturize.

We propose here a global approach based on the complete measurement system, by exploiting multidisciplinary skills on (i) vertical cavity surface emitting diodes (VCSEL) and the shaping of their beam; (ii) the design and manufacture of polymer optical micro resonators and coupling networks; (iii) gas sensors and surface functionalization. The use of a VCSEL source tunable in current over 5nm, combined with beam shaping and the use of grating couplers, provides better tolerance to misalignment between the source and the waveguide input, and thus simplify the injection of light into micrometric or submicronic structures in a portable system. Vertical coupling of the micro-resonator is favored to facilitate the deposition of the sensitive layer and to isolate the coupling networks and the waveguides. Since the 850nm wavelength does not allow direct detection of the absorption of the gas molecules of interest, a polyaniline (PANI) sensitive layer is added in order to provide selectivity and sensitivity to ammonia (NH_3). Its exposure to NH_3 causes dedoping, which is reversible at room temperature, and results in changes in its optical index and a variation in the resonance spectrum at the output of the micro-resonator, which can be measured using a simple photodiode thanks to the tunability. The compactness and integrability of micro-resonators, VCSELs sources and photodetectors makes it possible to envision arrays of functionalized micro-resonators for multi-target detection.

The manuscript begins with an overall presentation of the microsystem and its positioning in relation to the state of the art. The interest of polymer materials and technologies is discussed to achieve a low-cost lab-on-chip system, based on our previous work and our technological constraints. The integration of polymeric micro-optical elements on VCSEL is theoretically and experimentally studied to obtain a collimation and a spot size appropriate for the working distance considered, in order to reduce its natural divergence and to maximize coupling efficiency. Two post-production methods are used, discussed and compared: a method based on laser lithography and inkjet printing, and a 3D method using 2-photon stereolithography. Analytical calculation and FDTD modeling including technological constraints is presented to design coupling networks, waveguides and micro-resonators. The integration of a silicon photodetector is discussed to achieve complete integration. Next, several technological approaches are presented to create the structure designed in the technology and manufacturing section. The optical characterization platforms allowing the performance evaluation of each of the elements of the microsystem are detailed.

Preliminary results are presented and novel ideas to improve the test method are proposed. Finally, the integration of a chemically sensitive material at the surface of the waveguide material for NH₃ sensing is developed and tested. The prospects for future research are also discussed.

Keywords: gas sensor ; optical detection ; micro ring resonator ; polymer ; SU-8 ; 3D printing ; VCSEL ; near infrared

Acknowledgements

At the end of this unforgettable journey, I would like to express my sincere gratitude to everyone who helped or encouraged me during this PHD study time. I am grateful to University of Paul Sabatier for funding this research and supporting me during the difficult period of the epidemic. My acknowledgement is also given to LAAS for providing me with a platform for in-depth exploration in my favorite field. I also own my thanks to my committee members, as Ms. Virginie NAZABAL and Ms. Aurore VICET for accepting to be the reviewers of my thesis, as well as Ms. H el ene TAP and Mr. Olivier SOPPERA for their valuable comments and advice for improving this work.

I extend my greatest gratitude to my four thesis directors: Pr. V eronique Bardinal, Dr. Vincent Raimbault, Pr. Thierry Camps and Pr. Philippe Menini. Saying thank you just doesn't seem to be enough, they were an integral part of me being able to make it to the end. In the aspect of work, they teach me the professional content in their respective field and accompany me to overcome difficulties in exploring new fields. With a wealth of experience, they give me a variety of valuable advice. I appreciate a lot their availabilities with strong support for every moment when I need, all their suggestions are very precious to me. In the aspect of spare time, I will never forget the frequent "chocolate surprise" from V eronique, this provides me a lot of energy during work and brings me happy mood under pressure. Vincent always gives full of encouragement to me when I feel depressed for encountering bottleneck. By picking up positive thinking, there could be more solutions than difficulties. Thierry likes to tell anecdotes in coffee time, these stories are a good relaxation for switching brain thinking, his ideas often make me discover another way in the work. The BBQ organised by Philippe is a good occasion to gather people together, I am also very grateful for his help to me in administrative affairs. The years of time passed so quickly, the life in LAAS-CNRS leaves me a deep and pleasant memory with them, for their rigorous attitudes in the research, their earnest guidance, and their charming personalities.

I would also thank the entire TEAM group with whom I spent a lot of time improving the fabrication processes in the clean room. I would like to send a lot of thanks to Jean-Baptiste DOUCET for the technical support in chemistry domain, he is always patient to reply all the questions. I am also very thankful to Pierre Fran ois CALMON for laser writing and 3D print part, we got beautiful results for the collimation of light source. Many thanks to Laurent MAZENQ for all his support and advice for the photolithography process, especially with stepper. Special thanks also to Benjamin REIG for the characterisation trainings. Besides the professional advice and helps from Aur elie LECESTRE on plasma etching, Fabien MESNILGRENTE on inkjet deposition, Samuel CHARLOT on assembling, I will also express my gratitude to engineers: Adrian LABORDE, Guillaume LIBAUDE, Ludovic SALVAGNAC, Laurent BOUSCAYROL, V eronique CONEDERA, DARAN Emmanuelle, and DUBREUIL Pascal, your valuable support in terms of technology allows me to complete my work more smoothly.

I will give my appreciation to engineer Julien ROUL, for all his support in optical design, optical platform construction, and analysis software development. I've learned a lot of things with him in this aspect.

I would also express my appreciation to former PhD students Yu ZHAO, Miguel DIEZ and Aymen SENDI, their work experience in related projects helped me to get on track very fast at the beginning.

My thanks also go to my other colleagues and friends who stay with me in this time, in worktime and weekend. Even though I usually don't talk too much, but I enjoy the time sharing with you. My sincere heart is sent to all of you.



Last but not least, I am very grateful to my parents. Only with their selfless support, concern and love, can I overcome those difficulties and pursue my study till now. I am deeply indebted to my parents who always support me and share with me all my frustrations and happiness, wherever I am, and whenever I want. I am proud to be their daughter, and I am also becoming their proud.

Contents

Résumé.....	1
Abstract.....	3
Acknowledgements.....	5
I. General introduction/background	11
I.1 History and recent achievements	15
I.2 Theoretical fundamentals	17
I.3 Objective of this work	20
I.4 Overview of sensor structure and materials.....	21
I.4.1 Global presentation of sensor structures	21
I.4.2 Material selection.....	23
I.4.3 Conclusions	28
II. Design and fabrication of a collimated 850nm VCSEL chip.....	33
II.1 Principle of operation	33
II.2 Brief state of the art and main applications of NIR VCSELs	34
II.3 VCSEL beam shaping.....	35
II.3.1 State of the art and methods	35
II.3.2 Zemax modeling.....	36
II.3.3 Collimation results	38
II.4 Lens fabrication on a single VCSEL chip	40
II.4.1 Characterization of VCSEL chip before lens fabrication.....	42
II.4.2 Micro-lens fabrication by direct laser writing (DLW) and inkjet printing.....	44
II.4.3 Micro-lens fabrication by 3D laser printing	56
II.5 Conclusions on lensed VCSEL source fabrication	66
III. Analytical models and simulations of optical gas sensor.....	71
III.1 Waveguide dimension calculations for single-mode transmission.....	71
III.2 Design of grating coupler.....	75
III.3 Taper waveguide dimensioning	79
III.4 Calculation of micro-ring radius.....	80
III.5 Calculation of the vertical gap between the waveguide and the micro-ring resonator	81
III.6 CYTOP lower cladding thickness dimensioning.....	83

III.7 Design of the photomasks	84
IV Fabrication of the microresonators	91
IV.1 Fabrication of the reticles for stepper lithography	91
IV.2 Fabrication process of designed system	92
IV.2.1 Preparation of substrate coated by CYTOP	92
IV.2.2 Fabrication of Aluminum grating coupler on CYTOP lower cladding	95
IV.2.3 Fabrication of SU-8 waveguide and taper	106
IV.2.4 Fabrication of CYTOP gap between waveguide layer and the micro-ring layer	109
IV.2.5 Optical characterization for preliminary achievement	111
IV.2.6 Grating coupler on SiO₂ lower cladding	114
IV.2.7 Optical test setup evolution	124
V. Towards a NH₃ gas sensor with a PANI sensitive layer	129
V.1 Method of deposition of the PANI	129
V.1.1 Deposition of PANI in-situ	130
V.1.2 Deposition of PANI by spin-coating	130
V.2 Characterization of the PANI sensitive layer	131
V.2.1 Thickness and morphology	131
V.2.2 PANI optical parameters upon NH₃ exposure	134
V.2.3 Towards an integrated optical NH₃ gas sensor	135
Conclusion and perspectives	137
References	139
LIST OF FIGURES	145
LIST OF TABLES	151

Chapter I

General introduction/background

I. General introduction/background

Gas detection is involved in a wide range of applications in the environment and health fields. It is not only used in atmospheric science, but also for the monitoring of air quality in buildings or vehicles and for some breath diagnostics in health applications. Many kinds of gas sensors are exploited to monitor the rapid change of hazardous species in the working area or during an industrial process. There is an emerging demand for miniaturized, portable, and efficient sensors for many applications. Generally, the common detection targets include greenhouse gases (CO_2 , CH_4 , NO_2 , O_3 ...), carbon monoxide, Volatile Organic Compounds (VOC), as well as specific targets like ammoniac (NH_3) whose emissions are mostly attributed to organic wastes from breeding or fertilizer production units.

Among current detection methods, semiconductor metal oxide (SMO commonly named MOS) gas sensors are the most investigated category, mainly due to their high sensitivity (ppm or lower), their contained manufacturing costs and their suitability to integration into portable systems [1]. Electrochemical gas sensors can be relatively specific to individual gases like O_2 , CO , H_2S and various toxic species with sensitivities at ppm or ppb levels [2], but they usually suffer from drift or some cross-sensitivity issues toward interferents, but also strong dependency to ambient humidity and temperature [3]. To detect a specific gas at very low concentration, the optical gas sensors emerge as solid alternatives thanks to their high sensitivity, strong selectivity, response time, durability, stability, and also, ability to work at room temperature compared to other types of gas sensors. Their main drawbacks reside in their poor suitability for integration into portable instruments due to their high overall power consumption and cost [4].

In the specific field of optical sensors that can potentially be deployed in portable form factors, spectroscopic sensors, SPR (Surface Plasmon Resonance) sensors, and waveguide-based microresonator sensors are commonly encountered in academic research. In the scope of the present work, we mostly focus our attention on waveguide-based microresonator sensors due to their interesting potential regarding integration, parallelization, and suitability to collective manufacturing based on planar technologies which is a strong advantage for developing cost-effective sensors. Waveguide-based optical sensors have experienced rapid growth based on a variety of designs developed for integration. There has been great interest in the use of gas cells in which a high finesse cavity is created within an optical fiber, by looping the fiber to form a resonator [5]. Cavity-enhanced techniques are of particular interest, especially for miniature sensors: the use of resonant cavities allows one to enhance the light pathlength for a fixed physical length, and consequently enhance the interaction with the gas molecules under study [6]. As enhancement factors of 10^5 or higher can be achieved, this can be used to make sensors sensitive down to trace levels, or make highly integrated, portable sensors with a sufficient sensitivity for the targeted application. As our main objective is to propose a microsystem which is conceived with portability

in mind, we focused our attention on planar micro-resonator-based sensors, as these offers the advantage of cavity-enhanced techniques in a small form factor.

Planar micro-resonator based optical sensors stand out because they can deliver high light confinement in a small volume for a given spectral range, which leads to a significant decrease of the device dimensions that allows multiple detection areas, as illustrated in **Figure 1**. The working principle of these sensors is based on light-analyte interactions, with the aim of converting the presence of target species into an optical signal that can be measured. As for cavity-enhanced techniques, maximizing the interaction length between the optical signal and the analytes allows to improve the performance of the device. A common classification of resonant-based sensors is to separate sensors using refractive index (RI sensors) as the chemical-to-optical transduction principle, and sensors using other mechanisms like fluorescence, surface plasmon resonance (SPR), or optical absorption (non-RI sensors) [7].

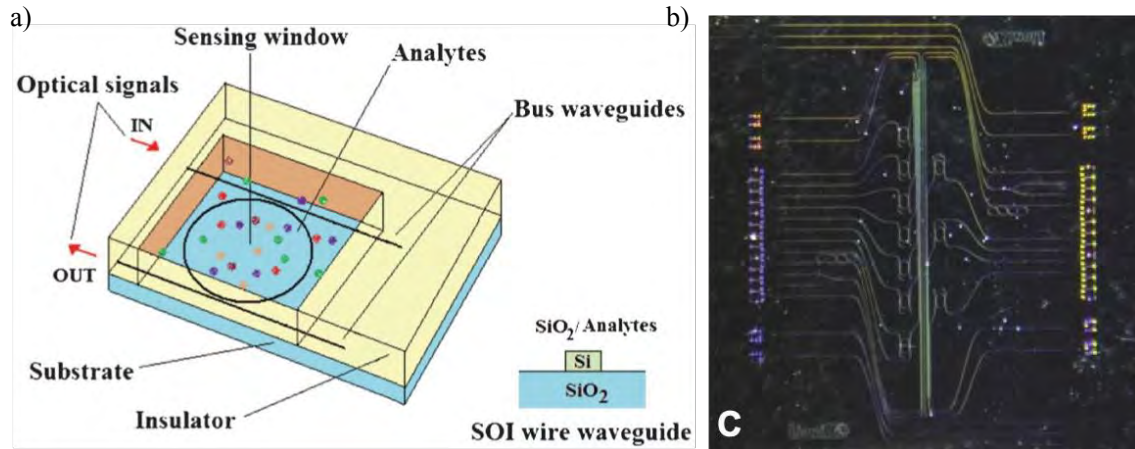


Figure 1. a) Schematic of a planar micro-resonator implemented in Silicon On Insulator technology [7]. b) Illustration of high density integration of micro ring resonators on a 1x1 cm chip using the TriPlex technology [8].

While the platform shown in **Figure 1-b** [8] is impressive in term of integration, it should be noted that it does not represent the whole sensing system, which requires excitation light sources and photodetectors to operate. For the light source part of this kind of detection system, a laser in the near infrared range (NIR) is often used, with a lot of research focused on 850, 1300 and 1550 nm sources. These wavelengths are inherited from all the developments that have been made in the optical fiber area for communications. This NIR spectral range has a much lower attenuation when passing through optical fibers than the visible one and due to the size of the communications market, relies on mature mass manufacturing device technologies. Moreover, as shown in **Figure 2**, this range avoids some specific absorption bands (called water bands) and have a relatively small scattering rate. The photodetectors at these wavelengths are also commonly available in the market and can provide a more economical and wider range of options.

In this work, we set our goal to design and fabricate a gas sensor based on the integration of technologies that we identified as suitable for a compact, affordable, and integrated system. These technologies include: (i) an 850 nm VCSEL (vertical-cavity surface-emitting laser) for the light source, which are very suitable for a miniaturized system, combined with a classic Si photodetector; (ii) a polymer-based microring resonator, a RI-based sensor that can attain very high sensitivities in a small area; (iii) a polyaniline (PANI) sensitive layer that is known to be well suited to selective sensing of NH_3 . While NH_3 has been arbitrary selected as the target in this work to meet agribusiness and health needs, the selectivity of this RI-based platform is obtained by the sensitive layer, hence different gases can be detected with suitable sensitive layer.

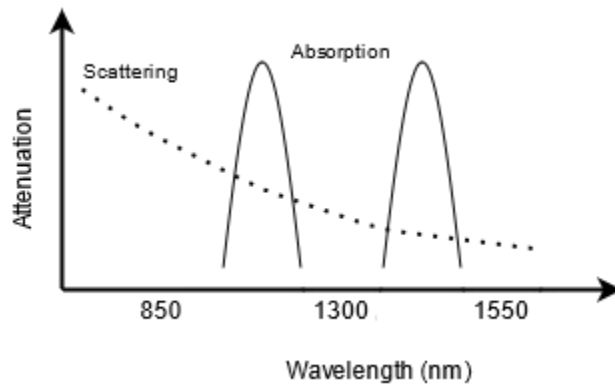


Figure 2. Schematic diagram of scattering attenuation of light in the air and the absorption attenuation of light in the glass fiber in the near infrared range.

The work presented in this thesis was carried out within LAAS (Laboratory for Analysis and Architecture of Systems – UPR8001) in Toulouse, a part of the French National Centre for Scientific Research (CNRS), within MICA (Microsystems of Analysis) team. This team has been developing microsensors for health, environmental, or industrial applications in liquid and gas detection domains. Recently, these research activities enlarged to optical sensors, which are more suitable for detection in harsh environments and taking benefits of the development of dedicated VCSELs sources for optical instrumentation. [9]

This work was supported by LAAS-CNRS micro and nanotechnologies platform, a member of the Renatech french national network. It offers access to its equipment which enables the development, shaping and processing of materials for the prototyping of micro and nano components in a wide variety of technological fields. All the micro components mentioned in the thesis were prepared in the cleanroom of LAAS, which adheres to ISO 7 standard (in ISO 14644-1 standard, the number of micro dust larger than $0.5\mu\text{m}$ is limited to 352,000 per cubic meter). A technical and equipment service group (TEAM) works in this clean room to provide support for research activities, on an issue related to their expertise.

This manuscript is organized in five main parts.

Above all, the overall design of the microsystem is presented, considering state of the art. The interest of polymer materials and technologies are discussed to realize a low cost “lab-on-chip” system, taking into account a previous work done in our laboratory for another spectral range, as well as our technological limitations. Afterwards, each key components of this integrated system are presented in dedicated chapters, from the light source part, to the grating coupler injection part, the micro resonator part, and the sensitive layer part.

In chapter II, the integration of polymer micro optics on a single VCSEL chip is studied to achieve a sufficient laser beam collimation and beam size reduction. Despite their numerous advantages, the natural divergence of a VCSEL is indeed too large for most applications, it has to be decreased for a proper coupling of the input beam in the microresonator and for insuring a good final detection sensitivity. Two different methods have been explored to integrate a polymer microlens on a single VCSEL chip at a post processing step. The results of both approaches are discussed and compared.

In chapter III, both analytical calculation and modeling simulations are presented to design the optimize the geometry of the grating couplers, the waveguides, and the microring resonator part based on the selected materials discussed in chapter I. A particular attention has been paid to integrate the technological constraints, both in terms of critical dimensions and micro/nano-fabrication tolerances. The integration of a silicon photo-detector is discussed to realize a full “lab-on-chip” system, instead of using external power-meter detector.

Chapter IV deals with the fabrication and subsequent characterization of the microring resonator, including the grating couplers. Several methods are implemented to create the designed structure, all the technical details are presented. Adapted optical detection platforms and analyzing softwares are built, to test the performance of the corresponding parts. Preliminary results are shown, and new solutions to improve the testing method are proposed. The advantages and drawbacks of these fabrication methods are described in this section.

In chapter V, the integration of a polyaniline sensitive layer for ammoniac gas sensing on the surface of the waveguide is developed and tested. The perspectives of this work are also discussed.

I.1 History and recent achievements

Optical gas sensors are devices that translates the variation of optical properties in presence of the targeted species to an interpretable signal, the optical signal variations being used as their transduction principle. Their operating principle can be based on specific optical properties like absorption, fluorescence, light scattering, or refractive index changes. They are effective in detecting the presence of gases or chemical compounds. This type of detection has an advantage for dangerous working environments surrounded by explosive or toxic gas, and they have less need for adding reagent and maintenance [10].

Among the different types of optical sensors, the most commonly encountered ones are based on the measurement of optical absorption at specific wavelengths that depends on the gas species. Most of the organic and inorganic molecules of interest possess absorption lines in the mid-infrared as shown in **Figure 3** [11], these absorption lines being linked to their vibrational and rotational energy transitions. In order to make low-loss guiding optical structured in the mid-infrared, different materials choices have been adopted in the literature (silicon, germanium or gallium arsenide typically) with promising results for chalcogenide glasses that covers a broad range of transparency up to 20 μm for telluride glasses [12]. Although recent advances have been made in the field [13], mid-IR key components remain hard to integrate into low-cost portable devices, due to issues related to their cost, form factor or reliability.

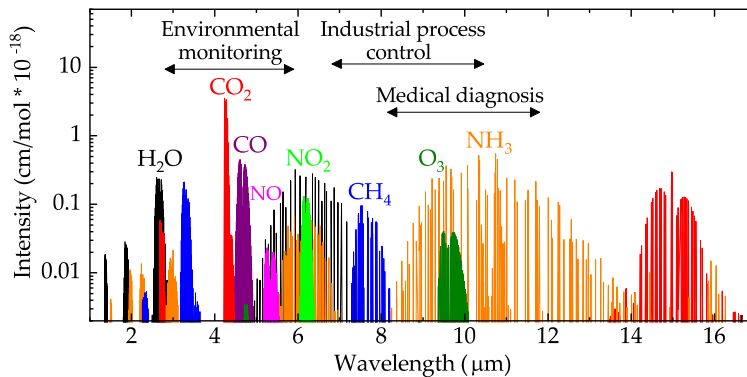


Figure 3. Absorption spectra of common gas molecules. [11]

On another hand, among indirect absorption gas sensors mechanisms, we focus on microresonator optical gas sensors, which are very suitable to collective manufacturing and system integration, with a simple structure and a low cost.

With an objective of making “lab-on-chip” type gas sensors, resonant-based methods are the most sensitive. Among the different optical resonators, the micro resonator sensors offer the highest quality factors, with reported values of 9×10^9 in air [14], and even exceeding 10^{10} [15]. micro

resonator sensors not only provide a high-quality factor (Q) [16], but also dramatically improve the sensitivity when used as sensors [17] by trapping the light path to travel multiple times inside the resonator, thus maximizing the light interaction with the species of interest. All these properties have pushed micro resonator sensors to the forefront of photonic sensors in recent decades [18] [19]. As the interaction length is used to accumulate sufficient phase shift to be detected, a coherent light source like a laser is preferred most of the time.

The first microresonator sensor was developed by Vollmer and Arnold in 2002 for detecting the proteins in aqueous environment, by monitoring the waveform shift. A microsphere resonator was used in this application [20]. Furthermore, microresonator sensors began to be applied to chemical sensing.

There are several kinds of micro resonator structures, like microspheres, microtoroids, and micro rings [21]. The highest reported Q-factor are obtained with microsphere resonators, but their 3D shape leads to a very challenging integration which limits their application outside of research laboratories. The optical modes confined in microtoroids resonators are more compact than in a microsphere for an equal diameter, but it is not suitable for an easier integration with other wafer-based technologies. While microresonator sensors based on planar structures like microring and microdisk resonators cannot match the Q-factors obtained with microspheres, with state-of-the-art values approaching $Q = 10^6$ [22] [23], they compensate by much better suitability for integration, even in as arrays for multiple target sensing. Among them, the microring resonator is more compatible with the photolithography process and chip scale integration, and as such has been retained in this work as the core of our resonant RI-based gas sensor.

Typically, micro ring resonator have achieved a Q factor on order of 10^4 - 10^5 for polymer materials [24] [25] a value somehow smaller than what is achieved with inorganic materials. The relative low Q factor is linked to the roughness of surface due to fabrication issues and light losses in the underlying substrate, as well as to propagation losses in the guiding material [26]. Otherwise, polymer materials also have other potential advantages in terms of manufacturing costs, low temperature processing, and also compatibility with vertically coupled microring resonators layouts, which are more suited to sensors than their laterally coupled counterparts [27].

A microresonator sensor is based on the modification of its evanescent field in the presence of analytes in the surrounding medium or at the sensor surface, and its output is affected by refractive index changes. This kind of Refractive Index (RI) based sensors can be separated in two categories [28] (**Figure 4**): (i) homogeneous RI-based sensors where the sensor response is produced by a change in the effective index in the sensing window; (ii) surface RI-based sensors, where the sensor response is influenced by specific absorption on the sensing area, the specificity being generally obtained by the addition of a sensitive layer on the sensing area.

Homogeneous detection does not offer selectivity, unless the excitation wavelength matches the analyte absorption bands. So when selectivity is required, a sensitive coating dedicated to the target gas is added on the microring surface. This is referred as surface detection.

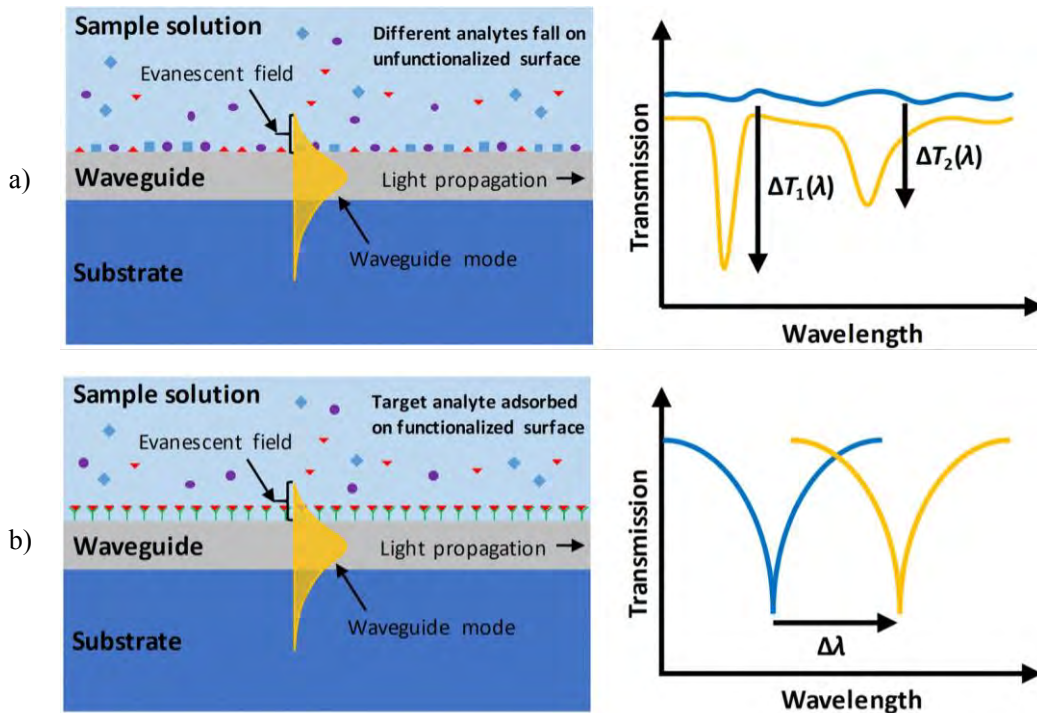


Figure 4. Two detection modes of microresonator sensors. [28]

If the sensitive layer can bring significant refractive index changes in the NIR range, we will have more options on low cost mature light source and detectors, as plenty of integrated, reliable, and cost-effective sources and photodetectors exists at lower wavelengths (850 nm, 1300 nm or 1550 nm being the most ubiquitous, for the reasons mentioned in the introduction section). While they cannot be used for direct absorption measurements due to the lack of absorption lines at these wavelengths, other sensing strategies can be implemented.

I.2 Theoretical fundamentals

In recent years, following the development of nanofabrication techniques, microring resonators gathered interest as passive label-free sensors [29]. They offer some numerous valuable features as Refractive Index (RI) sensing devices because of their high sensitivity, robustness, fast response time and compatibility with collective manufacturing cleanroom processes. Compared with the other types, the resonant properties of micro resonators with planar shapes (e.g., rings, racetracks) offer the ability to obtain high sensitivity in a compact form factor; this has the advantage of being

easier to integrate in an array arrangement on a chip, while collective planar technologies involved ensure a good reproducibility and controllability of the manufacturing process.

The operating principle of these micro resonators relies on the total internal reflection (TIR) of light confined in a ring-shaped cavity. At the resonance condition, the constructive interference appears at a group of specific frequencies/wavelengths, which indicates the “resonant” modes trapped by the micro-resonator light path circulation (**Figure 5-a**). When used as a RI-based sensor, the presence of target molecules at the surface of the micro resonators modifies the resonant condition in the micro ring, leading to significant shifts of its output spectrum (**Figure 5-b**).

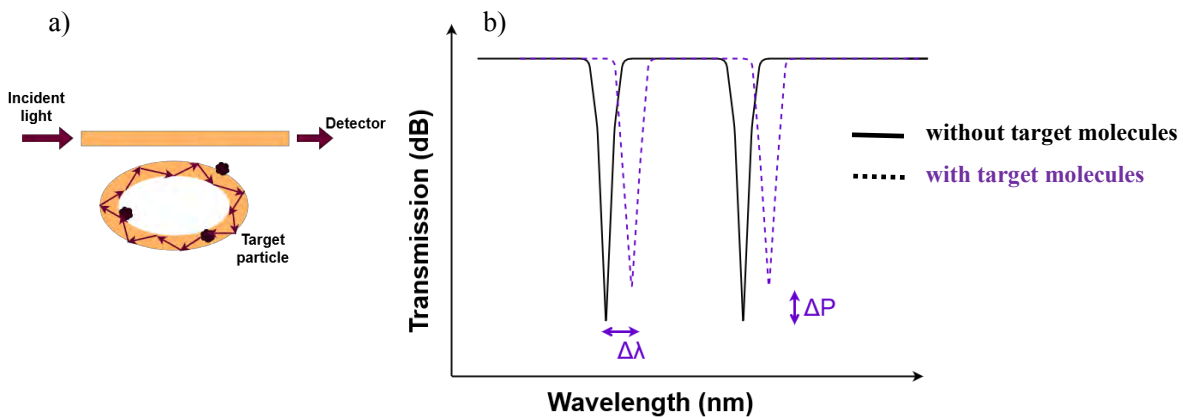


Figure 5. a) Specific wavelengths trapped by the micro resonator light path circulation. b) The presence of target molecules at the surface of the micro resonator will lead to a red shift in the resonance mode.

The detection is based on the measurement of the change in the effective index of the guided mode circulating in the micro resonator, induced by the interaction between the optical evanescent field and the target particles. This measurement is performed on the optical transduction signal which is the optical response of the micro resonator.

The presence of target molecules on the surface of the micro-resonator is observed via a spectral shift of the resonance peaks. In detection applications, in order to quantify the present molecules, two main methods are used in the literature [30]: using a shift of the resonance wavelength ($\Delta\lambda$) or the variation of the intensity at a fixed wavelength (ΔP). However, for detection of very low concentrations, the fluctuations in the intensity of the optical system should also be considered [31].

Intuitively, when the target particle with a refractive index greater than the medium around the resonator is adsorbed in the resonator, it pulls a part of the optical field outward, which increases the optical path length and leads to a red shift (**Figure 5-b**) of the resonance mode. [26]

The micro resonators can be designed to detect specific gases for environmental monitoring. For gas sensing, a relatively simple, and ascertainable set-up is to coat a sensitive layer specific for the gas of interest, onto the surface of resonator. The target gas absorbed onto the sensitive layer

induces some modifications of the effective index of the micro ring, and consequently increases the detecting sensitivity. This added benefit provided by the sensitive layer specificity towards the target gas has been adopted in a variety of research. A wide range of analytes can be targeted, such as ammonia, organic compounds, helium, argon and many others. Without this layer, the sensor would be sensitive to a lot of different elements and would therefore require operating complicated gas sample preparation steps (like separation columns, pre-concentrators...) in order to be able to measure some specific one.

In addition, an appropriate choice of both the optical component and the sensitive chemical coating significantly improves the response of sensor. The following table represents recent optical gas sensors using different materials coatings that are compatible with our device. All these sensors work in gas, with the exception of the work from C. Delezoide [27] that operates in water but shares similar materials and structure with our present work.

Table 1. Materials involved in various optical waveguide gas sensors

Sensitive layer material	Device structure (Substrate/cladding/waveguide/ring)	Target species	Operating wavelength	Sensitivity toward target	Remarks	Ref.
PHMB	Si/SiO ₂ /Si	CO ₂	1550nm	0-500ppm, with 6.10 ⁻⁹ RIU/ppm, LOD 20 ppm		[32]
Pd	Si/SiO ₂ /Si/HSQ	H ₂	1550nm	0.3% H ₂ S=9.15 10 ⁻⁴ pm/ppm		[33] [34]
MOF and ZIF-8	SiO ₂ /Si ₃ N ₄ /SiO ₂	VOCs	1575.67nm	Methanol 58 ppb Propylene 29 ppb Benzene 35 ppb Toluene 76 ppb Styrene 99 ppb		[35]
SU-8 based ligand	Si/SiO ₂ /CYTOP/SU-8	Cd ²⁺	1550nm	38.9 ± 10.6 ng/L in tap water 33.9 ± 7.8 ng/L in deionized water		[36]
Polyaniline (PANI)	Si/SiO ₂ /SU-8/ PMMA	NH ₃	980nm	37% for 4618ppm (power ratio P/P ₀)	500nm thick sensitive layer. Exposed waveguide length 5mm	[37] [38]
	Si/SiO ₂ /SU-8			26% for 4618ppm (absorbance ratio A/A ₀)	1µm thick sensitive layer	

Ammonia (NH₃) is of particular interest as it represents an important hazard to human health due to its toxic and corrosive nature. There is a strong demand on precise monitoring of its levels in the atmosphere, as well as for efficient breath analysers as NH₃ is an important biomarker for lung or

renal diseases [39]. Polyaniline (PANI) is widely used for NH_3 sensing; upon exposures it undergoes deprotonation (de-doping) which lowers its conductivity, with the advantage for this reaction to be reversible. This de-doping modification is also associated to modifications in refractive index of the PANI film as well as to its absorption properties [40], making the use of a PANI sensitive layer a straightforward choice to NH_3 sensing. It also has some interesting practical features as it is stable, soft, cheap, and easy to prepare. Considering all these factors, our first step focuses on this combination for the detection of NH_3 .

The reported PANI sensors in **Table 1** work at 980nm are very near to our spectral range, a PANI sensitive layer coated to SU-8 waveguide will dramatically increase the sensitivity of detection, by optical absorption changes. The experimental results in these articles show that the PANI/SU-8 optical sensor has a rapid response and can regenerate easily, this property provides good reference for our system design.

I.3 Objective of this work

The objective of this work is to develop an integrated optical micro-sensor for gas detection. A 850nm VCSEL (vertical-cavity surface-emitting laser) combined with a polymer micro-lens will be used as the light source. The light will be coupled in the waveguides through grating couplers. This kind of structure can achieve better tolerance to misalignment between the source and the waveguide input, as well as simplify the injection of light into micron or sub-micron structures and is well suited to a portable system.

The micro-resonator is vertically coupled to the near field of the waveguide, by a subwavelength gap. The vertical coupling scheme is favored over the lateral coupling scheme as it offers several key advantages for the further deposition of the sensitive layer: in particular, it isolates the waveguides by an upper cladding, thus limiting the interaction of the evanescent field generated by the micro ring to the sensitive layer.

In the case of NH_3 sensing with a PANI layer, gas adsorption will modify the refractive index of the upper layer and influence the guiding conditions, causing a variation in the spectrum at the output port waveguide. The variation will be monitored using a photodetector on the output. Taking advantage of the small form factors achievable with micro ring resonators, our ultimate goal can be expanded to integrate arrays of resonators with various sensitive layers for multitarget sensing.

I.4 Overview of sensor structure and materials

In this report, the discussion will focus on polymer materials which are easier and cheaper to process (spin-coating, low temperature processes), while offering interesting optical and chemical properties for sensing applications. The use of polymer materials is also particularly well suited to the vertical coupling scheme compared to other popular technologies like SOI. Based on previous works, SU-8 polymer material will be used for the waveguide and the microring.

Both in the literature [27] and in our group [41] [42], the combination of SU-8 ($n=1.57 @850\text{nm}$) as the guiding material and CYTOP ($n=1.34 @850\text{nm}$) as the cladding material has shown some promising results for sensing applications. The CYTOP amorphous structure makes this material highly transparent. Combined with its low refractive index, it is a material of choice for guided optics, providing good confinement as well as loss reduction to the substrate compared to silica [27]. Due to its excellent stability and optical performance, it has been extensively used as a cladding material in plastic optical fibers where it outperforms silica glass for material dispersion for example [40].

In this work, the structure under study will use both these materials, and VCSEL optical sources at a working wavelength of 850nm, a wafer of Si will be used as the substrate as it is easier to process than glass, both in terms of photolithography as in terms of wafer dicing.

I.4.1 Global presentation of sensor structures

The overall system, described in **Figure 6**, is envisioned as an affordable, portable optical analysis microsystem is designed to measure NH_3 gas concentration in the environment or in breath analyses as well.

A microring resonator represents the core of this microsystem. A sub-micron gap between the waveguide and the microring with a smaller refractive index let the light transmitted in the waveguide coupling into microring, and then form a comb-shaped wave at the output port, because of the emergence of resonating light inside the resonator. In presence of NH_3 , the PANI sensitive layer undergoes a change in its Refractive Index that influence the resonant conditions in the microring, then the output wave spectrum gives a response simultaneously that occurs as a wavelength shift of the transmission peaks, an interval change between two resonance peaks, or a change of intensity at a given wavelength (as shown in **Figure 5-b**), These optical variations are related to the gas concentration according to the degree of perturbation. This label-free method does not rely on separation or preconcentration techniques and is based on a reaction that is reversible at room temperature.

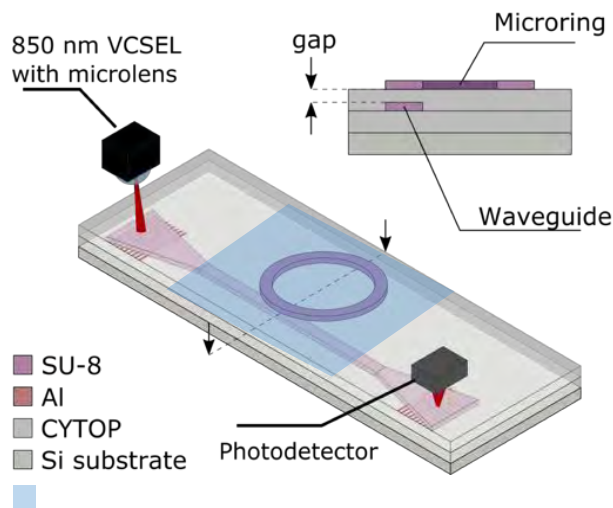


Figure 6. Schematic view of the optical micro-sensor for compact gas sensing

A single mode VCSEL is used as the light source, it has many advantages because of its compactness, low consumption, and adaptation for parallel analysis. The source what we are going to use in our system operates at a wavelength of 850nm (**Figure 7**), for which VCSELs technology is very mature with a stable performance and for which detection with low-cost standard silicon photodiodes is possible.

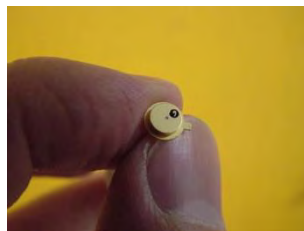


Figure 7. Image of a VCSEL chip mounted on a TO-46 header.

In addition, the emission wavelength can be slightly tuned with the current or the temperature with no mode hopping over few new nanometers, according to previous experiments. By designing the micro ring resonator accordingly, this wavelength tunability should allow us to scan at least two minima corresponding to two resonances in the output signal.

A polymer micro lens is integrated on the emitting surface of the VCSEL to focus the laser beam onto a grating coupler, which can offer a better tolerance to misalignment between the source and the waveguide input and simplify the injection coupling process.

Coupling between the waveguide and the micro ring can be achieved in two manners: lateral coupling, where both are in the same plane, and vertical coupling, where both are out of plane.

Vertical coupling has been favored here, with the gap being formed by a thin layer of CYTOP, so the waveguide is surrounded by the cladding. This configuration is particularly interesting for a sensor, as only the micro ring is exposed to the target. This is beneficial in both sensing configurations, homogeneous sensing as well as specific sensing where the micro ring is covered by an additional sensitive material.

The symmetric cladding configuration for the waveguide favors a centered evanescent field which can limit propagation losses, but also offers a better protection of the waveguides. Finally, due to the typical dimensions required for the gap (100 to 300nm typical), this coupling method is easier to implement as the gap is controlled by the thickness of the CYTOP layer and not the lithography resolution. While these devices are generally obtained by e-beam lithography, the vertical coupling scheme can still be fabricated using photolithography.

At the last step, in order to obtain the sensitivity and selectivity to detect NH_3 , a Polyaniline PANI sensitive layer is deposited on the SU-8 microring resonator. Other gases could be detected by the use of different sensitive layers, making the overall system potentially generic, depending on the availability of suitable sensitive layers.

I.4.2 Material selection

a) CYTOP as cladding

CYTOP is an amorphous fluoropolymer (**Figure 8**), with high optical transparency in the visible and infrared bands. With a refractive index similar to the one of water ($n=1.34$), this property is very suitable for microfluidic applications, for which the device must be surrounded by a liquid. This low refractive index makes it a material of choice for guided optics as it offers good confinement as well as loss reduction in the substrate compared to silica [27]. Its good lamination properties, excellent chemical, thermal, electrical stabilities, and surface properties attract a lot of interests for guided optics applications. It has been extensively used as a cladding material in plastic optical fibers where it outperforms silica glass for material dispersion for example [40] as well as in the design of planar guide [27] [41]. CYTOP also has functional groups to make a direct deposition on silicon substrates, and it is a solvent of high boiling point, high viscosity, and is hardly volatilized at room temperature.

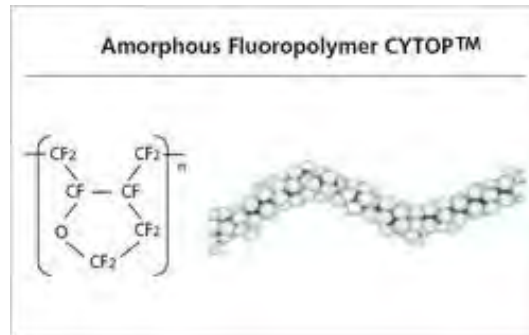


Figure 8. Chemical structure of amorphous CYTOP™

b) Aluminium as grating coupler material

At the beginning of the project, both polymer grating coupler and metal grating coupler were considered to fit our design. For the polymer grating coupler case, we majorly considered SU-8 as grating coupler material in order to match with the waveguide part. The fabrication process is presented in **Figure 9**.

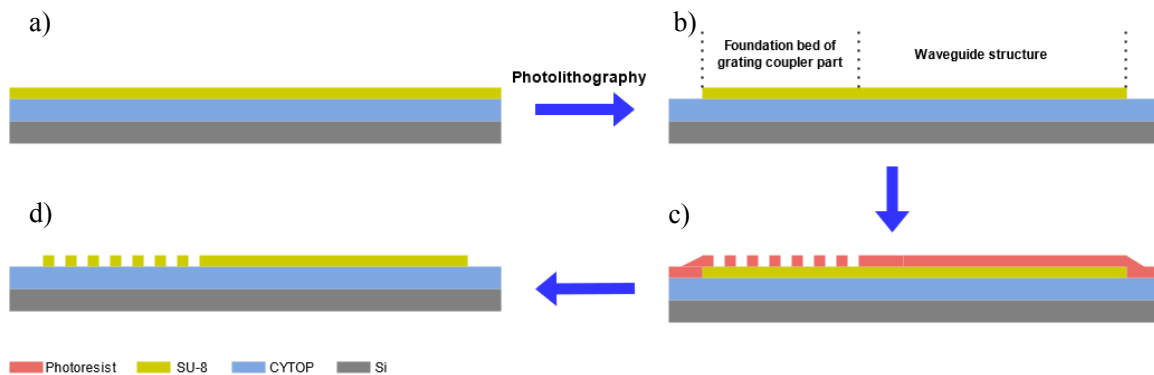


Figure 9. Schematic diagram of manufacturing process of SU-8 grating coupler by using stepper.

In the first step, the CYTOP and SU-8 layers are deposited by spin-coating on the Si wafer (a). A first exposure is applied on SU-8 layer to form the substrate of the grating coupler part and the waveguide structure (b). A second high-resolution photoresist is coated to cover all the structures below, and then exposed to form the adapted structure for the grating coupler (c). A plasma O₂+SF₆ etching can be used to partially etch the SU-8 layer [43]. Another thin layer of photoresist is deposited on the structured surface of SU-8 layer (shown in **Figure 9-c**), the surface planarization of the second coating is not ideal. Besides, the partial engraving of SU-8 structure is not easy to

implement, if the desired etching depth of grating coupler from calculation is inappropriate to the etching speed difference between the photoresist layer and SU-8 layer, the etching process may need to be done twice, with each time covering a part of the device. So, we quickly abandoned this idea and turned our attention to metallic materials, which usually has higher coupler efficiency compared with polymer grating couplers due to a higher index contrast [44] [45].

Considering CYTOP is a fluoropolymer that can be considered as highly hydrophobic (DI water contact angle $> 103^\circ$), and as such does not offer good adhesion properties for additional layer deposition by spin-coating while working as substrate, therefore some research teams have been using various plasma etching recipe to promote adherence.

An oxygen plasma treatment can induce hydrophilic response on silicon surface, because of a formation of hydroxide groups [46]. Unfortunately, this method is not suited for our case as shown in **Figure 10-a**. We did not observe a significant decrease of contact angle for the CYTOP surface after an oxygen plasma. Other plasma-based approaches have also been used, but our previous experiments have shown that their reproducibility is not satisfactory.

Among them, we tested successfully the method used by Bjorn Agnarsson et al. [47] that consists in coating CYTOP with a thin layer (30nm typ.) of aluminum, followed by wet etching. As shown in **Figure 10-b**, this treatment significantly decreases the DI water contact angle of the CYTOP ($< 40^\circ$) and gives highly reproducible wetting conditions for further spin-coating of SU-8 waveguide layer.

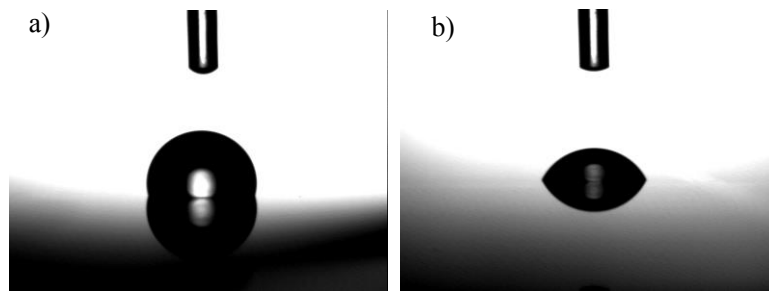


Figure 10. Contact angle of deionized water on the CYTOP surface. a) Water droplet before Al treatment. b) Water droplet after Al treatment.

Considering the high reflectance of aluminum, we choose to take advantage of this step to use this layer as the material of our grating couplers.

This approach also offers advantage: in the case of a vertical coupling scheme where an upper-cladding covers the waveguides, an additional technological step is required to avoid covering the

grating area with the upper-cladding material. This would lead to a drastic reduction in the refractive index contrast which would be detrimental to the grating coupler efficiency. For a polymer grating coupler made of the same material as the waveguide (**Figure 11-a**), the grating is uncovered and thus unprotected from degradations or contaminations during manipulations. Having a metallic grating located between the bottom cladding and the waveguide (**Figure 11-b**) solves these issues, as it offers a high refractive index contrast (Al vs SU-8) and a protection by both the waveguide and the upper-cladding.

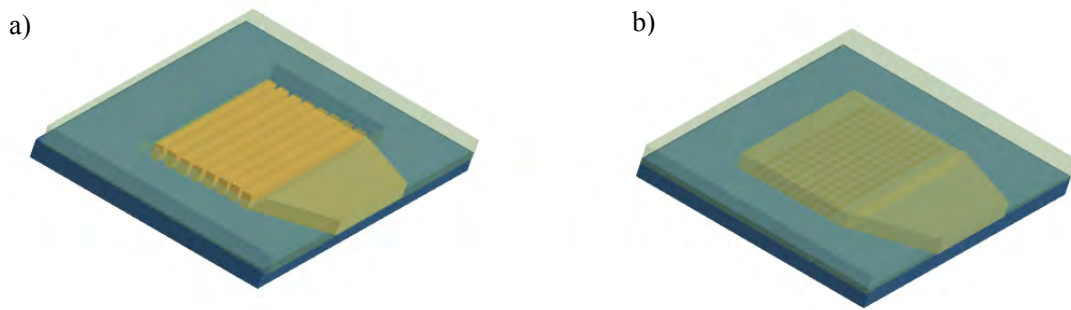


Figure 11. a) Polymer grating coupler, needs to etch the upper cladding leaving gratings unprotected. b) Al metallic grating coupler, where the grating is protected by both the waveguide and upper cladding.

c) SU-8 Polymer as waveguide/taper/micro resonator material

SU-8 is a commonly used epoxy-based negative photoresist, it was invented by IBM company in 1989 [48]. As shown in the structural diagram **Figure 12**, SU-8 derives its name from the presence of 8 epoxy groups. This is a statistical average per moiety. It is these epoxies that cross-link to give the final structure [49]. Its properties of transparency in near-infrared spectral band leads to a low optical loss. It has great ease of structuring, and a high heat resistance (degradation temperature around 380°C) [50]. Thus, it is suitable for electronic lithography as well as optical lithography for MEMS (Micro Electro Mechanical System) and optical micro-components [51] [52] fabrication. With a refractive index of 1.57, the RI contrast at 850nm wavelength between SU-8 waveguide and CYTOP cladding layer is around 0.22, a relatively high value for polymeric materials, which allows a strong optical confinement.

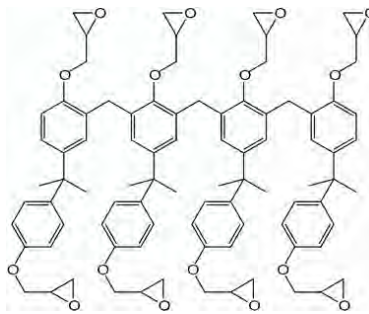


Figure 12. Chemical structure of SU-8.

d) PANI layer as sensitive coating on the surface of SU-8

Polyaniline (PANI) is a generic name for an entire family of polymers, the formula of which is given in **Figure 13**. This family of polymers is the direct result of the oxidation, under certain conditions, of a combination of monomers. It is one of the most interesting conductive polymers, and has a controllable electrical conductivity which can vary between that of an insulator, a

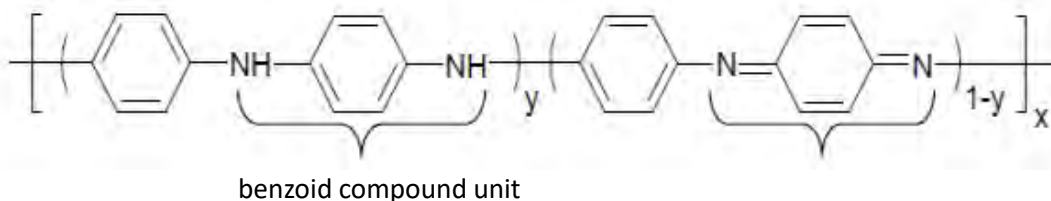


Figure 13. General structure of polyaniline. The term y denotes the degree of oxidation of the material.

semiconductor and a metal [53], its basic molecular formula consists of 3 ($-C_6H_4 - NH-$) benzoid compound unit and one quinoid unit ($-N = C_6H_4 = N-$) [54].

Interest has focused on polyaniline in the field of conductive polymers for several important reasons: its monomer (aniline) is relatively inexpensive, the polymerization of the monomer to polyaniline is straightforward, and the polymerization reaction proceeds with high efficiency.

In addition, its conductive form has excellent chemical stability as well as a relatively high electrical conductivity [55]. Its chemical structure made it suitable for the detection of ammonia [56].

Most of all, the absorption spectrum of PANI strongly varies in the NIR range in presence of gaseous ammonia (**Figure 14**) [57]. Therefore, it will be possible to make an indirect detection of this gas using a microsystem sensitive in this range. The variation is particularly high at 850 nm, which should translate into a high sensitivity of our sensor.

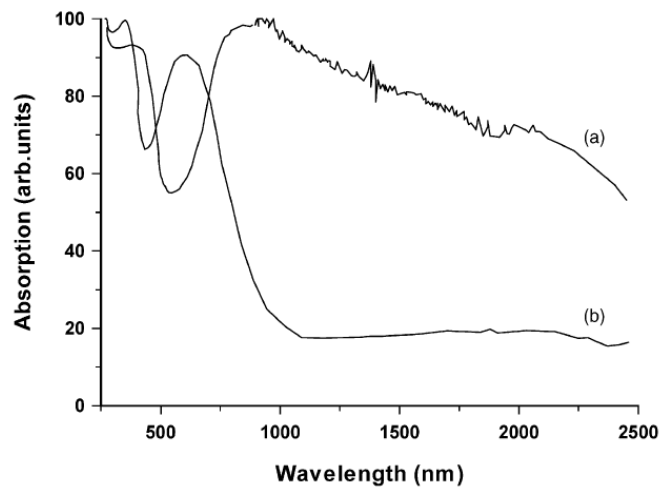


Figure 14. Absorption spectra of the polyaniline with (a) and without (b) gaseous ammonia. [57]

In the experiment shown **Figure 14**, the polyaniline thin film was coated on quartz substrate by using electrochemical method; the thickness of the sensing films was over 10 μ m. In our work, new deposition methods should be developed to control the thickness of film at nanometer level to match the microresonator dimensions.

I.4.3 Conclusions

To conclude, the design choices initially made for our microsystem resulted from a trade-off between materials compatibility and relative efficiency. They are reported in the table below.

Table 2. Initial design conception for microsystem.

	Needs	Answers
Sensor	<ul style="list-style-type: none"> • High sensitivity/ compacity • Low cost • Collective technology (stepper) 	<ul style="list-style-type: none"> • Optical microresonator • Polymer on silicon wafer • NIR Range
Light source	<ul style="list-style-type: none"> • Coherence, compacity • Efficiency, low cost • Tuning over few nm • Working distance few mm and small coupling area 	<ul style="list-style-type: none"> • VCSEL on PCB • 850nm • Tuning by current • Integrated collimation lens
Microresonator	<ul style="list-style-type: none"> • Transparent in NIR range • Adaptation with microfluidic system for further extended applications • Suitable for optical injection 	<ul style="list-style-type: none"> • SU8 waveguide • CYTOP cladding • Embedded metallic grating coupler with a surface suited to VCSEL beam size
Sensing layer	Sensitive to ammoniac in the NIR	PANI thin film above the resonator
Detection	Low cost	Silicon photodiodes

Chapter II

Design and fabrication of a collimated 850nm VCSEL chip

II. Design and fabrication of a collimated 850nm

VCSEL chip

In this chapter, a general presentation of 850nm electrically-pumped VCSELs on GaAs is stated. A brief introduction of its operating principle, state of the art and main applications are presented. This kind of source is chosen in this work because of its compactness, low consumption, and its possibility to be slightly tuned with the applied current. The integration of polymer micro optics on a VCSEL chip is then theoretically and experimentally studied to achieve a sufficient laser beam collimation. Two complementary methods are explored to integrate a polymer microlens on a single VCSEL chip at a post processing stage. The results of both approaches are discussed and compared.

II.1 Principle of operation

The term “laser” comes from the acronym for “light amplification by stimulated emission of radiation” [58], The laser emission arises from the interaction between the matter and electromagnetic radiation and the emitted beam is coherent, convergent, and monochromatic.

A laser is based on an active material which can generate optical gain at specific wavelength. This material is placed in a Fabry-Perot-type resonant cavity, which can be defined by two parallel mirrors. The distance between two mirrors and the resonant wavelength obey to the law: $2nL=k\lambda$, here L represents the distance (length of the cavity), k is the order of interference, n is the optical index of cavity, and λ is the wavelength.

To get a stimulated emission, a population inversion is necessary, that means sufficient energy should be brought to the electrons by optical or electrical pumping, to turn the higher energy levels to be more populated. Thanks to the contribution of incident energy, the lifetime of the electrons in the higher energy level becomes greater than the one of the electrons in the lower energy level, these electrons on higher level can recombine with holes in the valence band and emitting photons with a coherent phase and the same energy. The Fabry-Perot cavity then makes it possible to amplify the emission and obtain the continuous inversion of population by forcing the photons to make many round trips in the cavity. When the gain becomes greater than the losses, a laser effect occurs. For a sufficiently long cavity, several longitudinal modes are lasing, whereas if the cavity is very short, we can get a single-mode laser emission without any mode hopping.

Among laser devices, VCSEL diodes based on III-V semiconductor materials have the particularity of having the emission perpendicular to the surface, thanks to a vertical microcavity geometry (**Figure 15**).

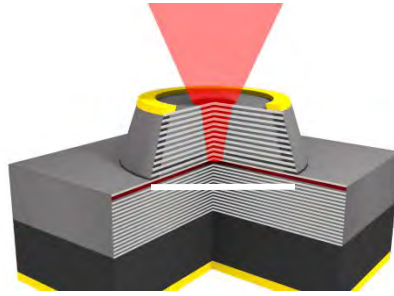


Figure 15. Schematic view of a typical GaAs vertical cavity surface emitting laser (VCSEL) with a short cavity length ($\sim 1\mu\text{m}$) and a small, buried oxide aperture ($\sim 4\mu\text{m}$) respectively leading to longitudinal and transverse single mode confinement and single mode operation.

In VCSELs, the optical cavity is composed of an optical gain zone of very small thickness ($\sim \mu\text{m}$) containing several quantum wells, leading to inherent longitudinal single mode emission. This central zone is surrounded by two high reflectivity DBRs (Distributed Bragg Reflectors). A DBR consists of a bilayer stack of alternate optical index materials. In the case of GaAs VCSELs emitting at 850nm, it is composed by the alternances of $\text{Ga}_{1-x}\text{Al}_x\text{As}$ alloy layers, with a variable x of Al composition between 15% and 90%. Each layer has a quarter-wave optical thickness so that the beams reflected by each interface are in phase. The high reflectivity stop-band of the DBRs is centered with the resonant wavelength, over a spectral range that depends on the index contrast in the DBR. The maximum reflectivity at the resonance depends on the number of stacked periods in the DBRs. Thanks to the high reflectivity achievable in the DBRs ($> 99\%$), it is possible to compensate for the very small thickness of the gain area ($\sim \mu\text{m}$) and to reach the laser conditions with a low threshold current ($\sim \text{mA}$).

II.2 Brief state of the art and main applications of NIR

VCSELs

The first concept of VCSEL was proposed by Kenechi Iga at the Tokyo Institute of Technology in 1977 and the first structure was developed by his team in 1979 [59]. This device was not made on GaAs and did not include DBRs, its emission wavelength was around $1.2\mu\text{m}$. The active region was formed by GaInAsP quantum wells. As for the two mirrors forming the amplifying cavity, they were simply defined on the surface by polishing surfaces parallel to the active area. This device demonstrated the proof of concept.

Two years later, the first VCSEL based on GaAs quantum wells emitting at room temperature in pulsed mode has been demonstrated [60]. A few years later, in 1987 [61], a laser structure emitting continuously with a threshold current of 2 mA (compared to 50 mA for first devices) was reported, thanks to better reflectivity and better electrical conductivity of mirrors [62]. Thanks to the

evolution of epitaxy techniques such as MBE, (Molecular Beam Epitaxy and MOCVD (Metal Organic Chemical Vapor Deposition) [63], GaAs-based VCSEL devices developed rapidly in the last 30 years.

In 1994, the insertion of a buried oxide aperture allowed to confine the current lines at the center of the active zone and greatly reduced the power consumption [64], this made it possible to obtain high efficiencies, as well as transverse single-mode devices emitting a Gaussian beam. This is of most interest for most applications and in particular for sensing and imaging. Another key advantage is the high modulation rate of these devices explaining the rapid development of GaAs VCSELs for optical interconnects.

In addition, the collective manufacturing method of VCSELs makes them very attractive for parallel operation. The first applications of VCSELs therefore mainly concerned in communications for local area networks and datacom, Research on VCSELs emitting in other spectral ranges is also very active. One can cite GaN-based devices for short-wavelength emission, InP-based VCSELs for telecom/sensing in the NIR range, as well as GaSb-based devices for TDLAS/sensing in the MIR [65].

The applications of GaAs VCSELs have greatly diversified these last years [66]. They range now from optical interconnections to miniaturized instrumentation, to laser printing and sensors [67]. Today, the field of sensors based on single-mode VCSELs is growing in the areas of miniaturized detection and 3D imaging [68].

The applications accessible to single-mode GaAs VCSELs are continuously developing in the field of instrumentation [69], notably thanks to the extension of device functionalities (integrated detection, spectral tuning features), with applications also varied as LiDARs (Laser Detection And Ranging), atomic clocks, or even SS-OCT imaging [70]. In this context, we target in this thesis work to develop a dedicated source suited for our integrated lab-on-chip sensing system.

II.3 VCSEL beam shaping

II.3.1 State of the art and methods

Despite numerous advantages, the natural divergence of a VCSEL is often too large to avoid the use of a microoptical element as the full divergence ranging from 10° to 22° FWHM (full width at half maximum), depending on the technology. In our case, the divergence of the single mode VCSEL has to be sufficiently decreased for a proper coupling of the input beam in the microresonator (maximal size of the coupling area: $100\mu\text{m}$ at a working distance of 2mm) and for

insuring a good detection sensitivity. We therefore study here the collimation conditions for a working distance of few millimeters.

Most VCSEL beam shaping techniques are based on an assembly of commercial microlens close to the VCSELs surface. However, these methods are long and expensive, and the control of the lens plane position is very tricky [71]. For these reasons, a direct integration of polymer microlens at the VCSEL surface is often preferable.

Several approaches have been reported in literatures, such as thermal photoresist reflow [72], deep lithography by protons [73], ink-jet [74], photopolymerization [75] etc. In all cases, a transparent pedestal is inserted precisely to set the position of lens plane in the first place, then a hemispherical refractive micro lens is added on top for beam control. The transparent pedestal and micro lens are added separately, and they are not limited to be the same material. In 2005, the ink-jet printing technique was firstly applied to fabricate lens on the SU-8 cylindrical pedestals for VCSEL beam focusing [76]. More recently, our lab developed a low-volume liquid deposition technique which demonstrated precise positioning and self-alignment of micro lens with a robotized silicon cantilever [77].

Following these works, we developed two different fabrication methods suited for an integration on single chip and not only on a wafer. Before detailing them, we present the design of such micro lenses (**Figure 16**).

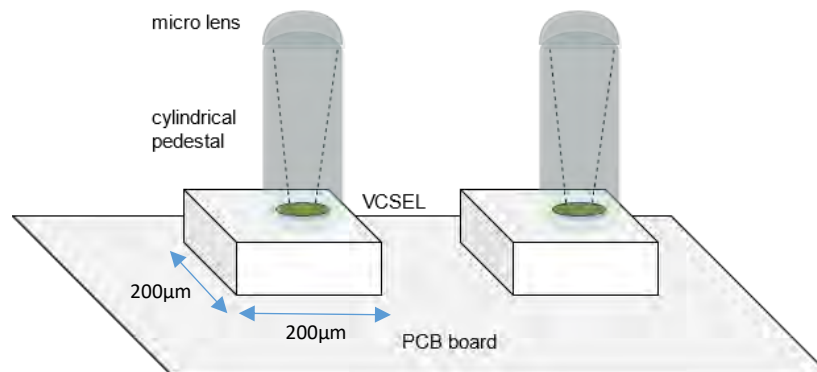


Figure 16. Schematic view of integrated polymer micro lens on VCSEL arrays

II.3.2 Zemax modeling

To define the geometry of micro lens, we used ZEMAX optical simulation software. ZEMAX is an optical design software commonly used for both imaging and illumination systems. It relies on ray tracing modelling the propagation of rays through an optical system. It can model the effect of optical elements such as simple lenses, gradient-index lenses, diffractive optical elements, and so

on, and produce standard analysis diagrams. It also includes tools to improve an initial lens design by automatically adjusting parameters and maximize performances [78].

Based on the previous work of a former PhD student Y. Zhao (under the supervision of V. Bardinal in our team and Julien Perchoux in OASIS team), on a microfluidic self-mixing based microsystem using a VCSEL [9], a similar ZEMAX program is used to minimize the beam divergence of output light of the VCSEL chip based on different combination of pedestal heights and ROC (radius of curvature) of micro lenses. Considering the usual numerical apertures of VCSEL source and technological constraints for micro lens fabrication, the typical pedestal height has to be at least higher than $90\mu\text{m}$ to obtain a sufficient divergence reduction [9].

The lens diameter D is fixed here to $80\mu\text{m}$. This value is generally limited by the pitch between adjacent VCSELs of an array in a wafer. In our case, it is limited by the footprint on the single VCSEL chip.

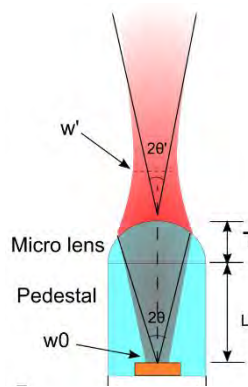


Figure 17. Dimensions involved in microlens design

For choosing the material in the software, we need to consult the Cauchy curve of material at Fraunhofer lines. Among them, we focus on several major Fraunhofer lines presented in **Table 3**, to calculate parameters n_d and V_d .

Table 3. Wavelengths of several major Fraunhofer lines.

Designation	Wavelength	Associated element
D_3 or d	587.6nm	He
F	486.1nm	$H\beta$
C	656.3nm	$H\alpha$

Here n_d means the refractive index of optical material on D_3 line (at 587.6nm), V_d is decided by the formula

$$V_d = \frac{n_d - 1}{n_F - n_C} \nu \quad (1)$$

Here n_F and n_c represents the refractive index of optical materials at 486.1nm and 656.3nm. By comparing the calculated n_d and V_d values of selected lens material with list of built-in material parameters in the software, here we choose the material B96-67 in Zemax database, it also has a similar optical parameter as SU-8.

Note that we also used another material named ip-dip in the following sections to fabricate a part of our micro lenses. Its optical parameters are similar with the built-in material named B48-46 in the software. However, these two materials have very tiny differences on the change in the final dimensions of the pedestal and lens. This change of refractive index can be therefore negligible.

II.3.3 Collimation results

The simulation results are shown in **Table 4**. Optimal lens geometry configurations of different pedestal heights retrieved by ZEMAX optimization for the collimation of a 80 μ m diameter lens. The GBPD (gaussian beam paraxial divergence) module returns the minimal divergence at the desired working distance.

Table 4. Optimal lens geometry configurations of different pedestal heights retrieved by ZEMAX optimization [9]

Pedestal height L(μ m)	Pedestal diameter D (μ m)	Lens ROC (μ m)	Lens height T(μ m)	beam diameter at 1mm 2 ω (μ m)	1/e ² full divergence angle2 θ ($^\circ$)
90	80	45	25	66	3.6
95	80	46	22	62	3.5
100	80	48	22	60.8	3.42
105	80	49	21	60.2	3.32
110	80	51	20	58.2	3.24
115	80	52	19	56	3.2
120	80	54	18	54	3.1
125	80	56	17	54	3.01
130	80	57	16	53	2.86
135	80	58	16	50	2.86
140	80	60	15	49	2.76
145	80	62	15	47.5	2.7
150	80	63	14	46.5	2.6

The result in **Table 4** indicates that using a polymer material closed to SU-8 resist, a 120 μm height, 80 μm diameter pedestal with a 18 μm height lens, minimizes the divergence down to 3 degrees at $1/e^2$ full angle or FWHM. At a working distance of 2mm, the spot of size on the grating coupler surface can be lower to 60 μm in an optimal way.

We can conclude from these results that we can reduce the divergence below 3° at the desired working distance, provided the pedestal height is at least equal to 120 μm . Moreover, whatever the height value above 120 μm , a satisfactory collimation can be achieved by simply playing on the lens ROC and height. The divergence could be even lower if we use a higher pedestal height but considering the maximal aspect-ratio of the polymer pedestal acceptable for keeping a good stability and considering its footprint on the surface of the VCSEL, a 120 μm to 150 μm pedestal height range is chosen to develop the fabrication process. This optimization result allows us to significantly improve incident beam coupling efficiency, reduce losses, and reach the requirements for the microsystem.

To get a more intuitive illustration of collimation, a simulation function named POP (Physical Optics Propagation) of ZEMAX software is also used to evaluate the wavefront transformation. In POP, the beam wavefront is graphically viewed in the geometry of ray tracing (**Figure 18**). If the dimensions of objects are far greater than the wavelength, the interference and diffraction effects can be ignored, but this obviously does not apply to our situation. In our case, the diffraction should be considered. The optical path goes through a pedestal then a micro lens with specific optical index, each point offers the complex amplitude information.

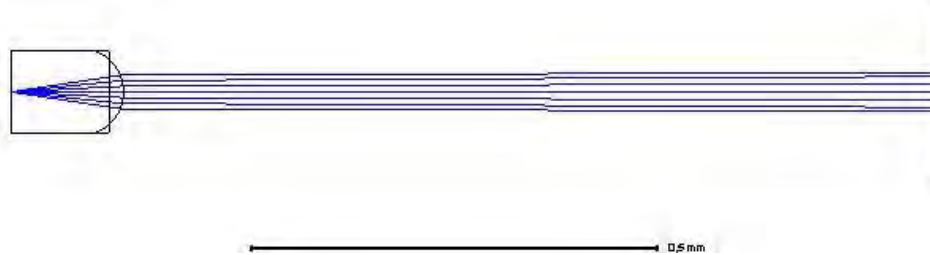


Figure 18. Illustration of ray tracing for VCSEL beam shaping in ZEMAX.

By changing the thickness of lens, the radius of lens curve is calculated automatically, then the optical path can be visualized as shown in **Figure 18**. When the exit beam on the right approaches parallel, it means that the beam divergence is collimated to the minimum by the added polymer pedestal and microlens.

A study of the tolerance to misalignments between the micro lens center and the output laser center was also carried out, to estimate the influence of undesired manufacturing error. To this aim, we considered a $1\mu\text{m}$ decenter and $0.5\mu\text{m}$ slant in case of the VCSEL surface is not parallel to the PCB (tilt), or a misalignment due to the limitations of the lithography set-ups. In this worse scenario, the divergence would increase by 40%-65%, to about 5° et $1/e^2$, while the spot size projected onto the grating coupler would increase from $60\mu\text{m}$ to $100\mu\text{m}$. This data will provide reference for our subsequent design of the sensor part.

II.4 Lens fabrication on a single VCSEL chip

As discussed above, the natural divergence of VCSEL can be higher than 14 degrees at $1/e^2$ full angle, which can lead to difficulties for injecting light into the coupling area in an efficient manner. In order to improve coupling efficiency, a micro lens is added above the emitting area of the VCSEL to reduce its divergence angle, then the beam spot size can be decreased dramatically at a working distance of several millimeters.

Compared with the hybrid assembly of commercial micro lens, a micro lens directly integrated on the VCSEL surface to collimate the output beam is more advantageous as the dimensions can be adapted as a function of the effective shape of the device beam.

In our project, the VCSEL light source is an oxide-confined top emitting GaAs diode chip from Trumpf photonics performing a single mode emission at 850 nm (**Figure 19-a**). Moreover, the beam has a stabilized polarization state because of a shallow etched grating at its surface (**Figure 19-b**). [79]

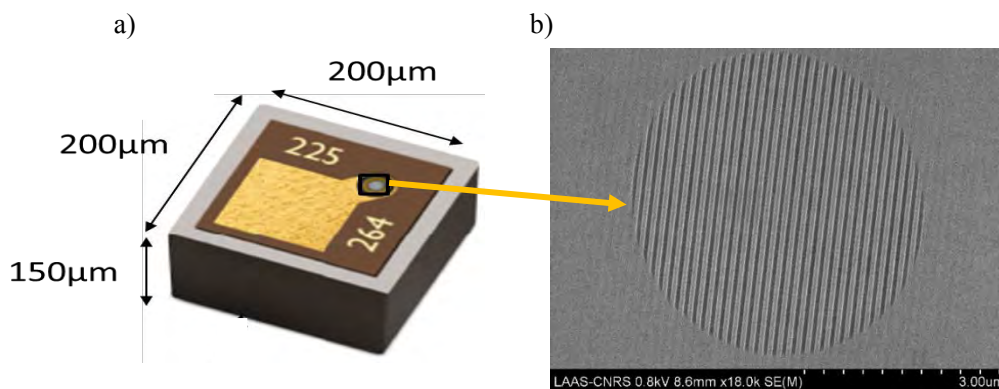


Figure 19. Single 850nm VCSEL chip with shallow etched grating at its surface (Trumpf).

The anode of VCSEL chip is connected to a $100\mu\text{m}^2$ bond pad, while its cathode is the backside metallization ($200\times 200\mu\text{m}^2$). This commercial 850nm VCSEL chip has a thickness of only $150\mu\text{m}$

and is mounted on a specific PCB (Printed Circuit Board). The PCB can be designed with different patterns to be easily inserted in the fabrication set-ups and in the final detection system (microfluidic or gas sensing applications). In this work, we used two different kinds of PCBs (**Figure 20**), corresponding to the application of former PhD student Yu Zhao in his thesis work, and the tray of nanoscribe set-up we used in this work.

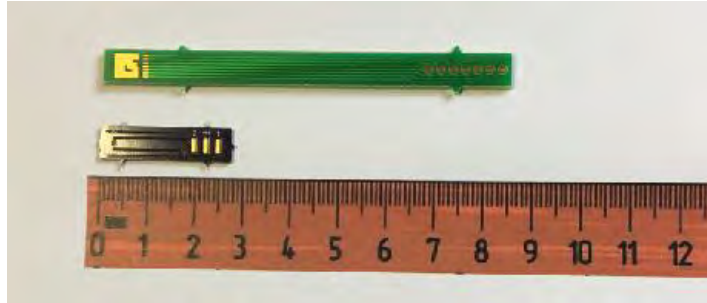


Figure 20. Illustration of the two kinds of PCB used in this study: the previous version on the top (green PCB) with a conventional thickness of 1.57 mm, and an optimized, thinner version at the bottom (purple PCB) with a lower thickness of 0.8 mm to fit the constraints of the Nanoscribe tray.

II.4.1 Characterization of VCSEL chip before lens fabrication

We measured the light-current curve of the used VCSEL chips using the optical set-up shown in **Figure 21**. This VCSEL set-up was also used to measure the evolution of the emission spectrum as a function of the applied current using an optical miniaturized NIR spectrometer (MAYA800Pro) through an optical fiber connected to the microscope stage.

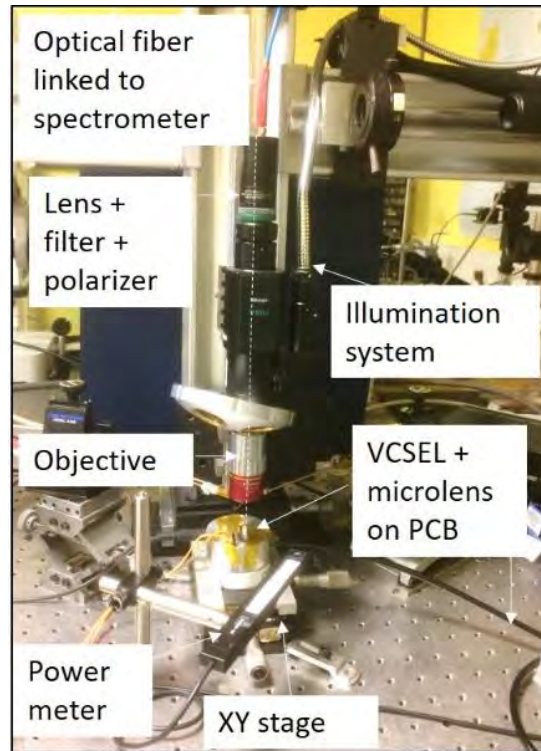


Figure 21. Image of the set-up used for VCSEL characterization (L-I-V and spectrum)

These VCSELs chips are polarization-stable devices (**Figure 22**) and are also indicated as single mode with a minimal SMSR (side mode suppression ratio) of 10dB for an emitting power of 1.4mW, which corresponds to a current of 3mA. The SMSR of the emitted beam is defined by the following equation:

$$SMSR = 10 * \log_{10} \frac{P_{fund}}{P_{sec}} \quad (2)$$

with P_{fund} and P_{sec} being the emitted powers for the fundamental and second order modes, respectively. As seen in **Figure 23**, the emission peak can be red shifted over several nanometers by simply increasing the applied current, as expected.

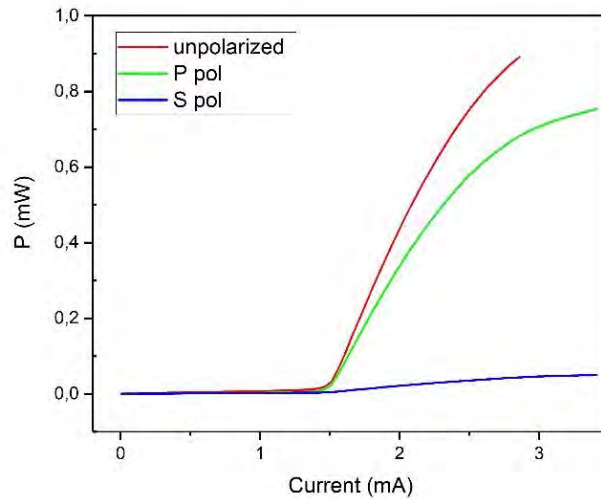


Figure 22. Measurement of polarization selection of the VCSEL emission as a function of the applied current.

It is not possible to precisely check the absolute value of the SMSR with our set-up because of the limited resolution of our miniaturized NIR spectrometer ($\sim 0.13\text{nm}$). However, we can calculate an approximative value from the acquired spectra. We obtained a SMSR higher than 10dB for applied currents in the range [2-9] mA. This corresponds to an available tuning range of $\sim 7\text{nm}$, which is in good agreement with our application requirements. Nevertheless, as the power emitted by the laser is varying with the current, a calibration will have to be done before its use in the sensor.

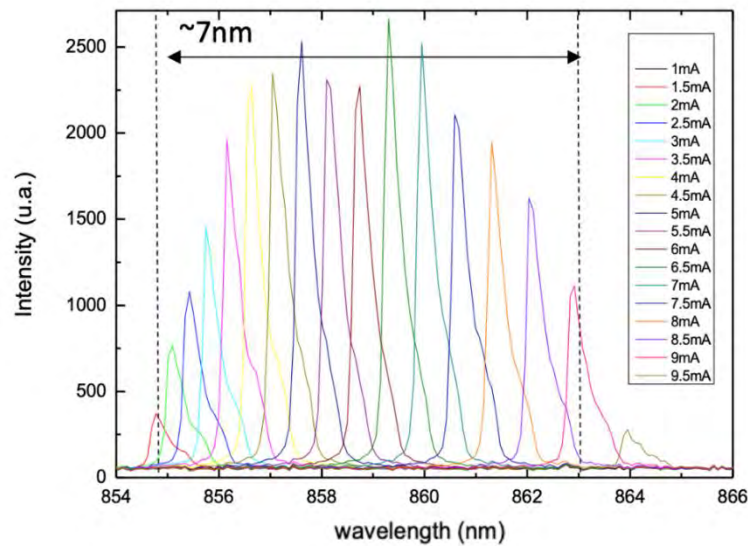


Figure 23. Measurement of the evolution of the emission spectrum of a typical single mode VCSEL chip according to the applied current.

Moreover, a beam shaping has to be developed to reduce the beam divergence and to achieve an efficient coupling into the waveguide besides optical micro-resonator. As the size of VCSEL chip

is only $200\ \mu\text{m}\times 200\ \mu\text{m}\times 150\ \mu\text{m}$, making a micro lens on an individual chip constitutes a new challenge. Methods based on spin-coating and conventional photolithography are indeed not applicable here. Integrating a micro lens on a VCSEL chip which is already mounted on a PCB therefore is tricky. For these reasons, we developed two different methods to solve these issues.

II.4.2 Micro-lens fabrication by direct laser writing (DLW) and inkjet printing

In a standard way, i.e, during collective fabrication at a wafer scale, the pedestal is usually made of a thick photoresist such as SU-8 which is deposited by spin-coating. However, when considering fabrication on a single VCSEL chip having a small surface ($200\ \mu\text{m}\times 200\ \mu\text{m}$ typ.), we cannot use spin coating anymore. The use of a dry film photoresist instead is therefore chosen to provide a good thickness uniformity, without edge beads [80]. Compared with a more than 10% thickness deviation produced by spin-coating, the formed dry film has smaller variation in thickness, so it performs better in terms of uniformity. This film is usually deposited using lamination. In our case, we take advantage of a softer method recently developed in our lab and based on the use of a nanoimprinting set-up [81].

According to previous works and existing equipment conditions in LAAS, we designed and proposed a specific process based on photoresist dry film and further ink-jet deposition of the micro lenses. The full process is shown **Figure 24** [82]. This part of the work was done in collaboration with Y. Zhao [9]. This method exploits a nanoimprint equipment that makes the soft printing of polymer films on fragile samples possible.

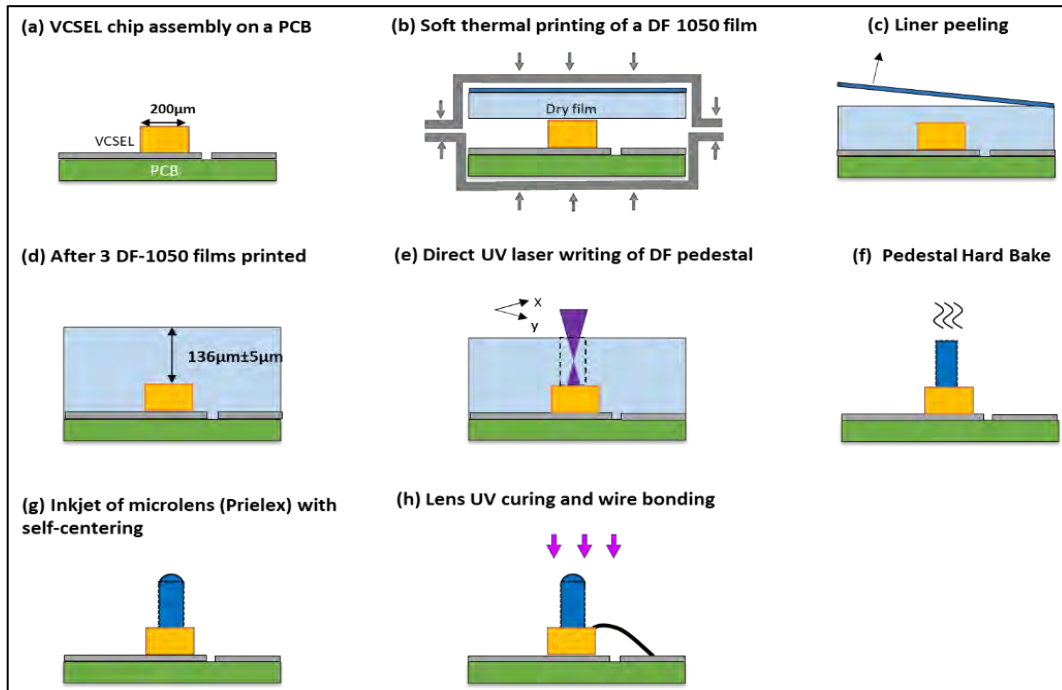


Figure 24. Procedure of VCSEL based micro-optical system fabrication. [82]

II.4.2.1 Pedestal fabrication by DLW in DF-1050 films

Firstly, the VCSEL chip is mounted on a PCB (Printed circuit board) with conductive epoxy (**Figure 24-a**). This adhesive is insoluble in organic solutions as acetone or isopropanol, in order to avoid falling off the VCSEL from PCB in the subsequent developing process. The bonding layer needs to be thin and uniform, to ensure that the emission angle of the VCSEL beam is perpendicular to the PCB plane.

After this assembly, a soft plasma O₂ process is carried out to remove impurities on the surface of VCSEL chip which is already mounted on the PCB circuit board. Afterwards, a stack of commercial dry epoxy negative photoresist film of DF-1000 series is deposited using soft thermal imprinting. This soft thermal imprint step is realized with a Nanonex NX-2500 Nanoprinting set-up. It is a machine dedicated to nanoimprint which allows a sufficient vacuum between the mold and the substrate, in order to avoid bubbles, and able to apply an isostatic pressure (from 0 to 450 PSI/31bars) thanks to flexible membranes, as shown in **Figure 25**. This technique is especially well suited to imprint onto non-planar, small and fragile samples.

The nominal thickness of the used DF-1050 dry films is 48µm, so we have to print 3 films to reach a pedestal height higher than 120µm, as aimed.

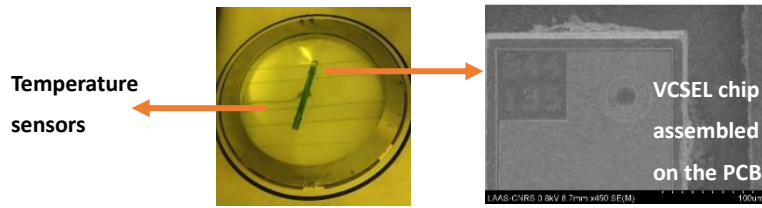


Figure 25. View of the VCSEL chip assembled on a PCB is sandwiched by two elastic films. A sufficient vacuum is used to imprint dry film on the non-planar sample. A temperature detector is used to control the temperature in the pressure chamber.

After these successive printing steps, the thickness of three-layer DF film slightly retracts and the final height is lower than the target value. By applying an equivalent pressure, a smaller stressed area leads indeed to a stronger film deformation. During this printing, the chip's small protrusion deforms the film above it, and compressed the final thickness of the films. A lower printing pressure can help to increase the final thickness, but we also need an enough adhesion which is positively related to the pressure. So a trade-off is made on the applied pressure which is set to 5PSI during the printing.

In the case of a 3-layer stack, the final thickness is 135 μm instead of the 144 μm expected value. We studied the effect of relaxation time elapsed between the printing step and the direct laser writing. A time interval greater than 12 hours at room temperature is recommended for the laminar polymers to restore the most natural state of relaxation. A soft baking at 50 $^{\circ}\text{C}$ for several hours can also accelerate this evolution. Without this step, the height of the pedestal may be shorter and non-reproducible.

A stack of several DF-1050 (thickness 48 $\mu\text{m}\pm 3$) films is preferred over the DF-1100 (100 μm thick) as it is more heat-resistant and limits the constraints in the material and from our experience, it offers better adhesion on the VCSEL surface and reproducibility.

The pedestal height will set the microlens focus plane position. To reach a 120 μm height as simulated before, 3 layers of DF-1050 are imprinted onto the surface of VCSEL by soft thermal printing.

As standard lithography cannot be applied on such small surfaces, Direct Laser Writing (DLW) has then to be used to pattern a well-aligned cylindrical pedestal on the VCSEL surface. This method allows a good alignment for individual VCSEL dies (0.5 μm).

This laser writing process is implemented by a Kloe Dilase 750 (L-2D). It provides UV laser irradiation at 405, 375 and 325nm, and a set of 3 optical tubes that offers different resolution capabilities: 0.4 μm , 2 μm and 15 μm . The equipment can write on planar or three-dimensional samples with thicknesses up to 10mm. Thanks to a high depth of field and a control over the focus

of the laser beam, it is adapted to thick photoresists as well (up to 1mm) and can form 2D patterns as well as 2.5D patterns.

The 80 μm diameter pedestal has to be written on a $200 \times 200 \mu\text{m}^2$ surface. Alignment of the pedestal with the emission area is critical for the performance of the micro-lens: the alignment precision of 400-500nm achieved with the DLW equipment ensures that polymer cylindrical pedestals can be photo-patterned at the top of VCSEL chips with a good centring. After the DLW step, a post exposure bake at 120°C curing for 20mins is used to stabilize the printed features and provide optimum performance. After development in Cyclohexanone (99%) solution, pedestals are ready for polymer lenses to be added on their top surface.

With this method, one can see that the shapes of pedestals are not perfect cylinders. The top part diameter is indeed slightly larger than the lower part, as shown in **Figure 26**. In particular, the dry-film stack has a moderate tapered shape which can be attributed to the laser writing process, and so some extent to a non-optimal vertical position of the laser focal writing plane. This focal plane has to be fixed before laser writing, and it is directly dependent of the exact pedestal height which is not known at this stage due to the afore mentioned uncertainty on the final thickness after the soft imprint step. However, this slightly tapered shape does not significantly impact the laser beam propagation as the beam extent is much smaller. We can also observe on the pedestal's sidewall the delimitation between each stacked dry-film and also that the lower layer has a thinner height because of the higher pressure applied on it during the soft imprint step. Nevertheless, the printing conditions were optimized to lead to a reproducible thickness that can be considered for the next step.

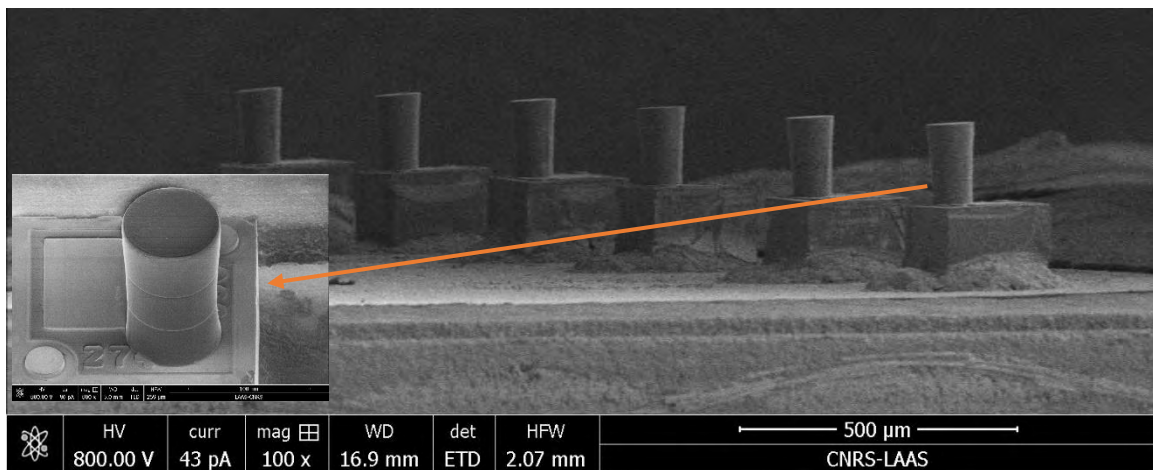


Figure 26. Polymer pedestals formed on mounted VCSEL chips on PCB by soft imprint of several DF films and direct laser writing.

II.4.2.2 Lens deposition

After DLW step, liquid droplets are accurately deposited onto the top of the polymer pedestal using an inkjet printing setup (Altadrop) under video control. The ink is ejected by a piezoelectric head. Produced droplets are deposited onto the moving substrate, thanks to three different deposition heads. that are available to adjust the droplet diameter according to the surface functionalization state of the top surface. Deposited material is then condensed either, by heating or UV curing: the choice of the method being dependent of the ink composition. The schematic diagram of the inkjet printing set up used is shown **Figure 27** [83].

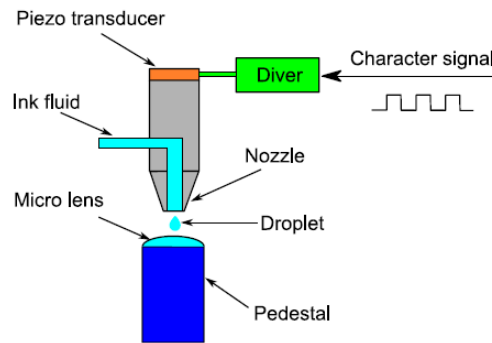


Figure 27. Schematic diagram of the inkjet printing setup [83]

Based on gravity and liquid surface tension forces, the accumulation of droplets forms a hemispherical surface that play the role of a microlens. The lens height and ROC can be easily modified by increasing the number of ejected droplets.

a) Thermo curable lenses

The home-made ink we first tried is called Cipol T, based on organic acids and alcohols derivatives. It was developed by Jean Baptiste Doucet from TEAM service. It is a low viscosity resist that becomes a hard polyester after thermal curing, by evaporating excess solvent. A calibration is therefore necessary to precisely control the final lens dimensions.

To precisely control the expected shape for the micro lens, a calibration is launched at first on a pedestal array on a Si wafer (**Figure 28**), to find the relation between droplet numbers and the final thickness of the lens, and on the same time the volume reduction rate as a function of curing time.

The pedestal array of the calibration sample is formed by photolithography, which is faster and cheaper than laser writing. Firstly, a heating lamination is applied on Si wafer, by Shipley 3024 machine, to add 2 layers of DF-1050 films on its surface, with a pressure of 2.5bars, and the temperature at 90°C. This process can be done in seconds. For a fixed diameter of cylindrical base, the height of pedestal will not influence the relation between liquid drop number and the final thickness of lens, so this substrate can simulate the real situation as well. We formed a 9×9 array for the test pedestals.

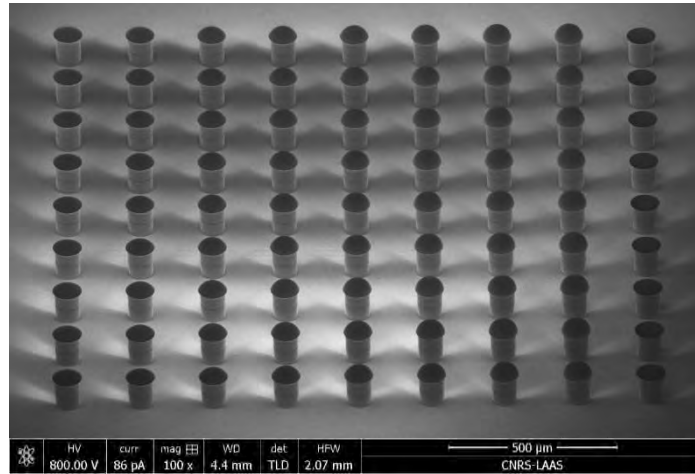


Figure 28. Pedestals array for calibration of lens thickness.

Then the ink jet is applied by gradually increasing the number of droplets in each column. As we can see in **Figure 28**, the rightmost column is kept as reference group without any droplets added, and the left columns are added separately by 10,12,14...24 droplets. We can see a remarkable change of lens heights. A long-term hard baking at 120°C is then applied with a shrinkage of lens shape caused by the solvent evaporation that has to be measured during fabrication and controlled.

To protect this semi-liquid structure before curing, we measure in real time the heights by LEXT-OLS confocal microscopy, which is designed for nanometer level imaging, 3D measurement and roughness measurement. By using the multilayer mode, it can capture a clear image from a specimen consisting of materials with extremely varied reflectivity levels (as Si and DF polymer in our case).

The confocal microscope uses fluorescence optics instead of illuminating the whole sample at once, the laser light is focused onto a defined spot at a specific depth within the sample. By using a pinhole filter, only the signal of focal point can be fed back, with a specific depth position information. The final image collects all these spots information and then can form a 3D pattern of its real structure. This optical detect is very fast and can avoid any physical contact for a height detection.

Figure 29 shows the measurement results of confocal microscope, the height difference can be read directly in the software. The ring patterns on the top of micro lens do not present its real surface morphology, they are caused by the step length during measurement.

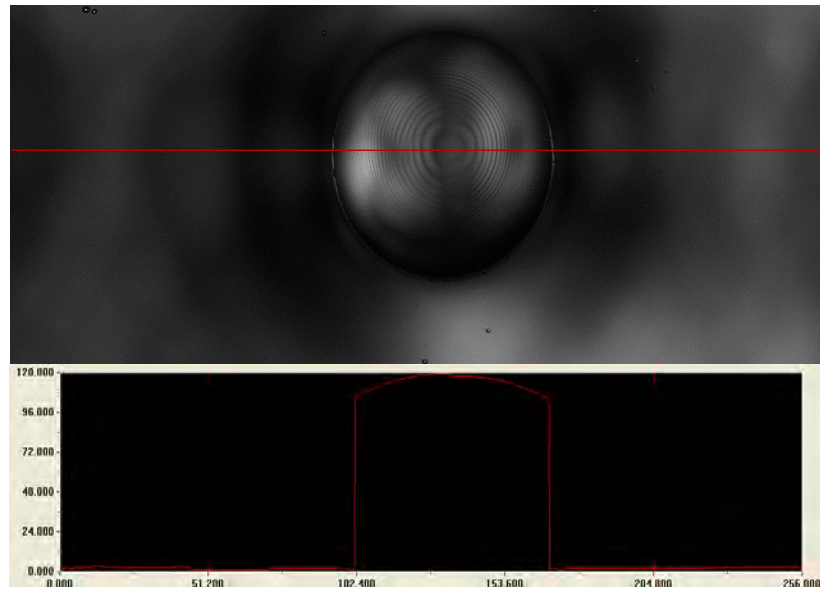


Figure 29. Measurement of semi-liquid dimension of micro lens by confocal microscope.

For each droplet number, 9 samples in the same column are measured to verify the repeatability of the operation. The average value is recorded in **Figure 30**, a data error around $0.5\mu\text{m}$ shows a good size uniformity of droplet at nanometric scale. These calibration curves were used to target the aimed microlens dimensions.

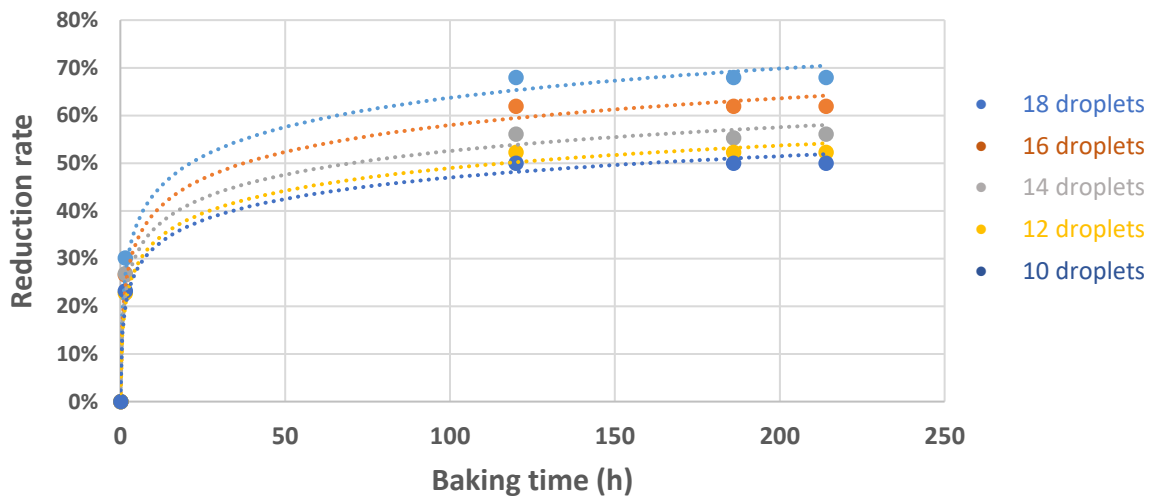


Figure 30. Measurement by confocal microscopy of the reduction rate of heights of micro lens as function of the baking time and number of jetted droplets.

b) UV-curable lenses

We noticed that a minimal period of more than 1 week is needed to stabilize the lens shape for the Cipol T thermocurable polymer material [82], so a commercial UV ink was tried in a second step. The commercial ink (Prielex SU-8 material from Microchem) can be polymerized immediately under UV exposition. Thanks to the integrated camera monitoring system of the Altadrop, the lens formation can be observed in real time and adjusted with no need for long calibrations as before. The result is shown in **Figure 31**. The optical quality and smoothness of lens surface is very good.

Due to the formation mechanism by surface tension effects, micro lenses formed by ink jetting method have indeed a very smooth surface [84], as confirmed by SEM (Scanning Electron Microscope) images shown in **Figure 32**.

At the end of the process, the bonding of the VCSELs can be done and the devices can be tested. Before presenting the characterization results, we discuss in the next section an issue that can be encountered using this method.

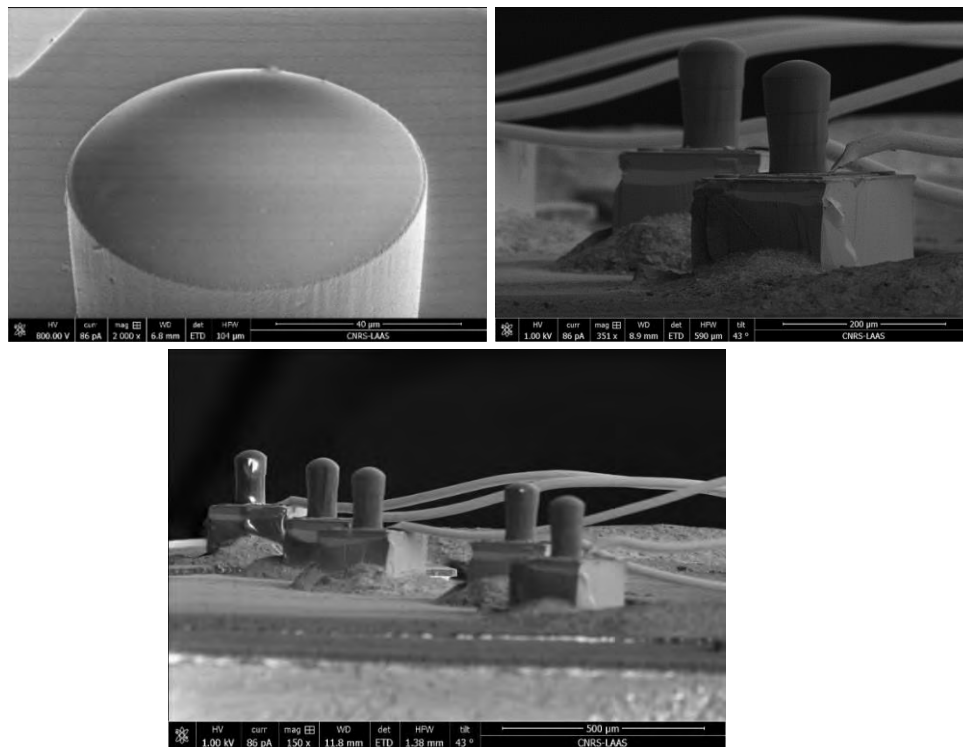


Figure 31. Micro lens fabricated by ink jetting on VCSEL chips and general view after wire bonding.

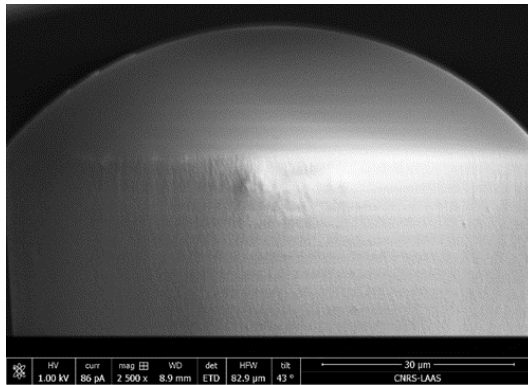


Figure 32. Micro lens fabricated by inkjet of commercial material Prielex SU-8.

II.4.2.3 Problems of pedestal flatness control

Since the VCSEL chips are mounted manually on a PCB, the uniformity of the used glue is a very important parameter to control, otherwise the patterned pedestals can be sometimes tilted, as show in **Figure 33-a**. Moreover, if the pedestal surface itself is not horizontal, the droplet deposited by gravity does not form the desired hemisphere shape, sometimes it flows from the side (**Figure 33-b**) and does not reach our designed goal.

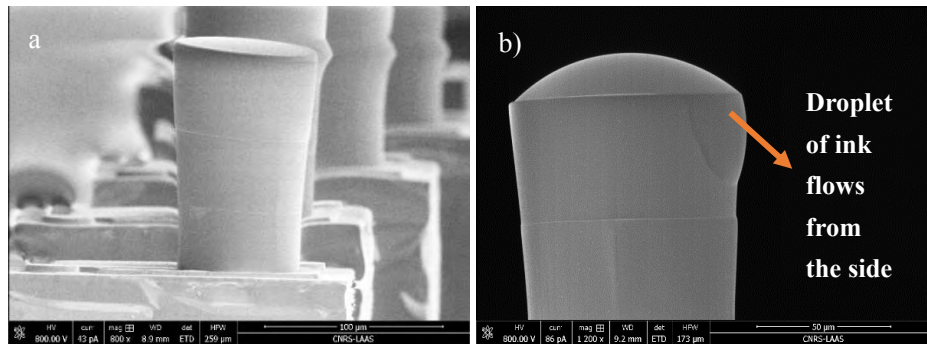


Figure 33. Inclined pedestal surface caused by the surface flatness defects under VCSEL chip during assembly.

To avoid this issue, a solution suggested by Prof. T. Camps was explored as an option, to maintain the verticality of the pedestal cylinder and to solve the flatness problem.

Normally, to ensure a strong bond, the thickness of glue layer is about 20μm, so we would like to build a “protection wall” around VCSEL to reduce the convexity of it and the surrounding PCB board, a specific WBR-2100 dry film (Dupont, 100μm) was chosen as surrounding plane, due to its high yield and quality through uniform resist thickness across the entire substrate, it is also environmentally friendly by using solvent free process.

The thickness of 2 stacked layers of WBR-2100 films can reach $180\mu\text{m}$, which is slightly higher than the thickness of VCSEL ($150\mu\text{m}$) plus the one of the glue layer ($20\mu\text{m}$), so this plane will share the pressure during soft print of DF film and protect well the upper surface of pedestal to be flat. The photolithography step will remove WBR film in VCSEL zone, as shown in **Figure 34**. After a standard DF film deposition process described in the previous section, a post exposure process, and a hard baking at 120°C for 10 minutes are applied on DF pedestal, to strengthen the bonding between pedestal and VCSEL. The WBR layers can be then dissolved by acetone. These steps are optional choice to promote the yield of vertical pedestal if the initial mounting condition is too bad.

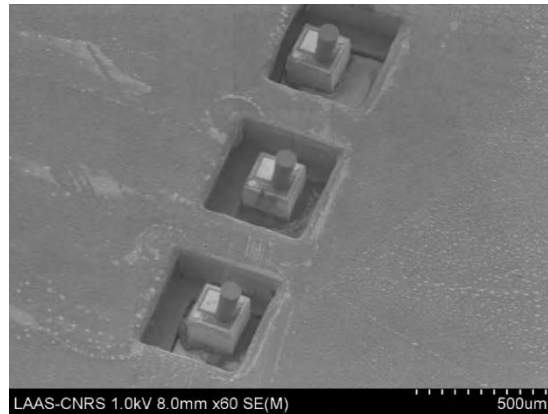


Figure 34. WBR film forming a « protection wall » to ensure the verticality of DF pedestal.

II.4.2.4 Characterization of lensed-VCSELs

a) L-I curve

After all these optimizations, several VCSELs chips with pedestals and Prielex micro-lenses were characterized. To first verify the transparency of this fabricated pedestal and micro lens, the L-I curve of the VCSEL with and without lens were measured (**Figure 35**).

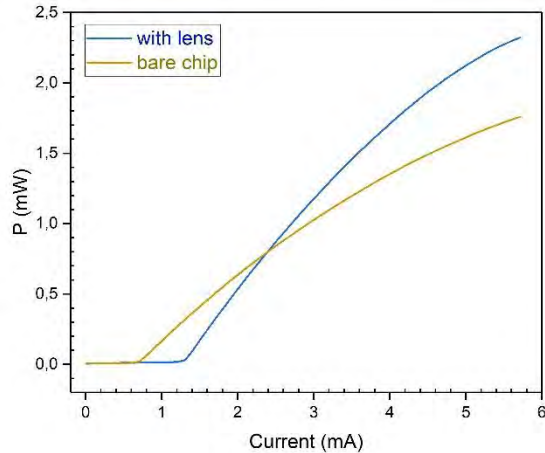


Figure 35. L(I) curve of VCSEL with and without collimation micro lens.

According to the data and as expected, the optical losses caused by the pedestal and micro lens polymer structures are negligible. The insertion of the micro lens only slightly shifts the current threshold of the VCSEL as the top reflectivity is slightly modified, and it increases the output power at higher currents. This can be explained by the fact the emitted mode becomes slightly more divergent with the current and it is better collected in the presence of the microlens. However, this is not useful for our application as this corresponds to a better collection of the second order mode with our high NA microscope objective. This does not correspond to our experimental conditions (no additional optics) and only the fundamental mode will be coupled. We also checked that the polarization selection is kept higher than 78% despite the presence of a polymer material instead of air at the surface of the polarization grating.

b) Beam divergence

We built with the help of Julien Roul from I2C service a new characterization bench including a beam profiler (Beamage) to measure the $1/e^2$ divergence angles of bare VCSELs and lensed VCSELs. the schematic diagram is shown in **Figure 36-a**. The Beamage profiler software can acquire the 3D, 2D, XY (cross-sectional graphs along the crosshairs) beam tracking.

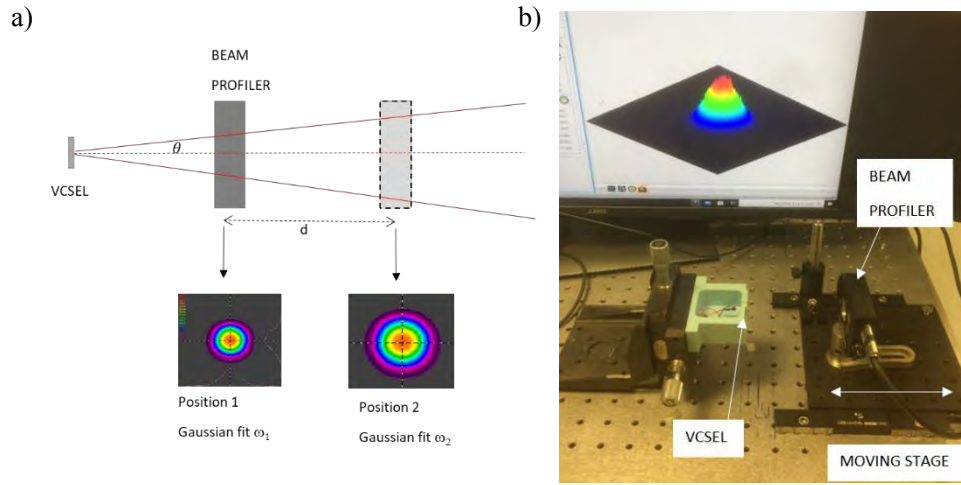


Figure 36. Measurement set-up of the beam divergence of single mode VCSELs

Two images of the 3D laser beam profiles (**Figure 37-a**) are taken by moving the detector over a given distance d using a translation stage. We fit the intensity profiles by a Gaussian function, to recover the beam at $1/e^2$ divergence angle: ω_1 and ω_2 . The divergence of beam is then given by the following equation:

$$\theta = \frac{\left(\frac{\omega_2}{2} - \frac{\omega_1}{2}\right)}{d} \quad (3)$$

This bench in **Figure 36-b** is very simple to use with mounted chips. It can also rapidly achieve light-current curves measurements or divergence tests for different applied currents and is free from any calibration.

The measured divergences of VCSELs before and after lens integration are shown in **Figure 37-b**. The applied current on VCSEL was here 3mA. We can see that the measured output light divergence has been significantly reduced, from around 14 degrees to ~ 3 degrees, the diameter of light spot at 2mm distance is about $51\mu\text{m}$, these values fit very well with our simulation results taking into account the lens and pedestal dimensions.

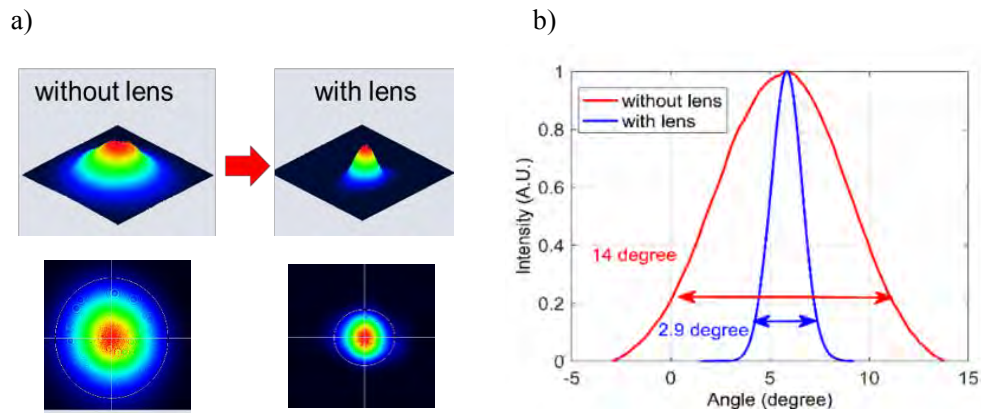


Figure 37. a) Intensity profiles measured with the beam profiler ($I=3\text{mA}$). b) Divergence of VCSEL with or without micro lens fabricated by inkjet writing.

II.4.2.5 Conclusions on the first method

To conclude, we used soft printing of a dry film, DLW patterning and ink jet printing of a UV curable ink (Prielex) to successfully reduce the beam divergence of 850nm VCSEL single chips already mounted on a PCB. These chips were used in a self-mixing microfluidic sensor [82] and can be also used for our gas sensor application.

However, as above-mentioned, the control of pedestals shape and flatness remains tricky with this method. As it is not possible to precisely control the height of pedestal during the soft imprint steps when fabricated on a single chip, an adjustment of the laser writing focus plane is always needed. To ensure repeatability in the micro lens parameters, a measurement of the pedestal diameter and height and a re-estimation for the droplet numbers to use are necessary prior the inkjet step. Considering these complex operation steps and long fabrication time, we investigated a simpler and faster method.

II.4.3 Micro-lens fabrication by 3D laser printing

II.4.3.1 Advantages of 3D printing technology and working principle

In recent years, additive manufacturing (3D printing) has proved to be a viable alternative to conventional planar technologies, with applications in photonics, biology, or lab-on-chip among others. Compared with photolithography, 3D printing offers more freedom in the type of shapes that can be achieved, enabling new fabrication schemes. As a non-collective method, 3D printing is well suited to structure single objects, which is typically the case for creating micro-lens over

single dies VCSELs. In current market, the commercial stereo-lithography (SLA) 3D printers provide a convenient platform for low-cost fast-prototyping of LOC systems. [85] [86].

Additive manufacturing can be performed with various techniques, which can be classified according to their working principle (technology), resolution or surface roughness among others. Main parameters can be compared in **Table 5**. It should be emphasized that due to the very dynamic nature of the market, new 3D printing equipment are issued each year with incremental enhancement of their features. For example, considering stereolithography, some equipment like the Kloe Dilase HR can reach 5 μ m resolution, it's a significant improvement over other equipment [87]. This increase in resolution is always a compromise with the total build volume achievable and the writing speed, so currently no technology can cover the whole spectrum of resolution, accuracy, build volume needed. Considering the precision required for the manufacturing of micro-optics, only the two-photon polymerization (2PP) currently offers appropriate characteristics, as recently demonstrated in the literature [88].

Table 5. Comparison between main additive manufacturing technologies for polymeric materials (adapted from Nanoscribe Whitepaper “Additive manufacturing based on two-photon polymerization”).

Additive manufacturing technologies	Two-Photon Polymerization (2PP)	One-Photon Polymerization			Fused filament fabrication
		Continuous digital light processing (DLP)	Stereolithography (SLA)	Projection micro stereolithography (P μ SL)	
Min. XY feature size [μ m]	0.2	30	25	2	≥ 250
Layer thickness range [μ m]	0.1 - 5	15 - 150	25 - 300	5 - 50	20 - 400
Accuracy or tolerance [μ m]	< 1; $\pm 0.5\%$	± 50	± 150 ; $\pm 0.5\%$	± 25	± 200 ; $\pm 0.15\%$
Surface roughness Ra [μ m]	< 0.01	>1	> 0.1	≥ 0.5	>1

The 2PP writing means that the photosensitive material is polymerized by absorption of two photons simultaneously; this absorption only occurs in a small voxel at the focal plane (**Figure 38**), which leads to a high resolution of writing. We took the opportunity of the presence of a Nanoscribe GT2 equipment available through the MultiFAB platform [89] to evaluate this technology for direct 3D printing of micro lens on VCSELs.

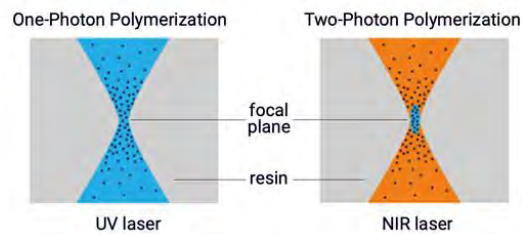


Figure 38. Comparison of one-photon polymerization and two-photon polymerization.

The 2PP technology working principle is illustrated in **Figure 39**. The photosensitive material is polymerized by absorption of two photons simultaneously. This non-linear optical process occurs when an ultrashort pulse laser is focused tightly in a small area. The size of this area is related to the laser spot, the laser power, and the properties of the material itself. By scanning the laser focus throughout the material or by moving the sample with a fixed laser spot, a 3D structure can be built.

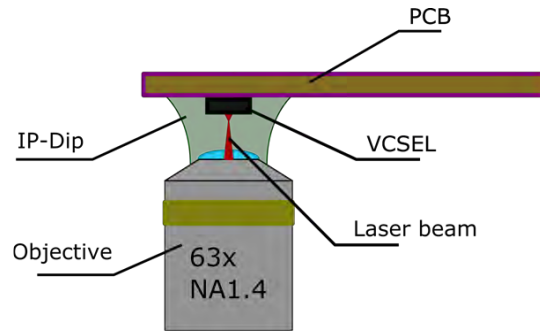


Figure 39. Working diagram of the 2-photon polymerization Nanoscribe 3D printing machine. The substrate (here a VCSEL mounted onto a PCB) is dipped into the photoresist which is in direct contact with the objective lens.

According to a comparison to other additive manufacturing technologies for polymeric materials, this 2PP additive technology has advantages in aspects of high resolution and accuracy (**Table 5**), which attracts more attention in micro-optical fabrication domain.

This new technique presents the advantage of being applicable on the surface of VCSEL chips directly at a post mounting/assembly stage, with the additional benefits of being able to change arbitrarily any dimensions of the pedestal and micro lens.

II.4.3.2 Process developed for lens fabrication

As illustrated in **Figure 39**, the substrate is immersed (dipped) into the IP-Dip liquid resist at the beginning. In our case, the substrate is a custom PCB with an assembled VCSEL. Then by slowly pulling the substrate up, the polymerization occurs layer by layer at the programmed position. After the exposure is finished, SU-8 developer solution is used to remove extra polymer part then leave only the pedestal and micro lens for the collimation of source light.

The machine model we used here is PHOTONIC PROFESSIONAL L- 3D (Nanoscribe), a 780nm femtosecond (pulse \approx 100fs) laser source is used, with a power from 50-150mW. The voxel size of 200nm in X/Y direction ensures its high resolution. The movement range of XY-stage is around 10 \times 10cm². Sample holders in different forms are provided by the manufacturer (**Figure 40**), we choose to use the DiLL sample holder as its deeper tolerance for substrate thickness is closed to the normal thickness of PCB. A 76 \times 26mm² PCB is commended to adapt this system.

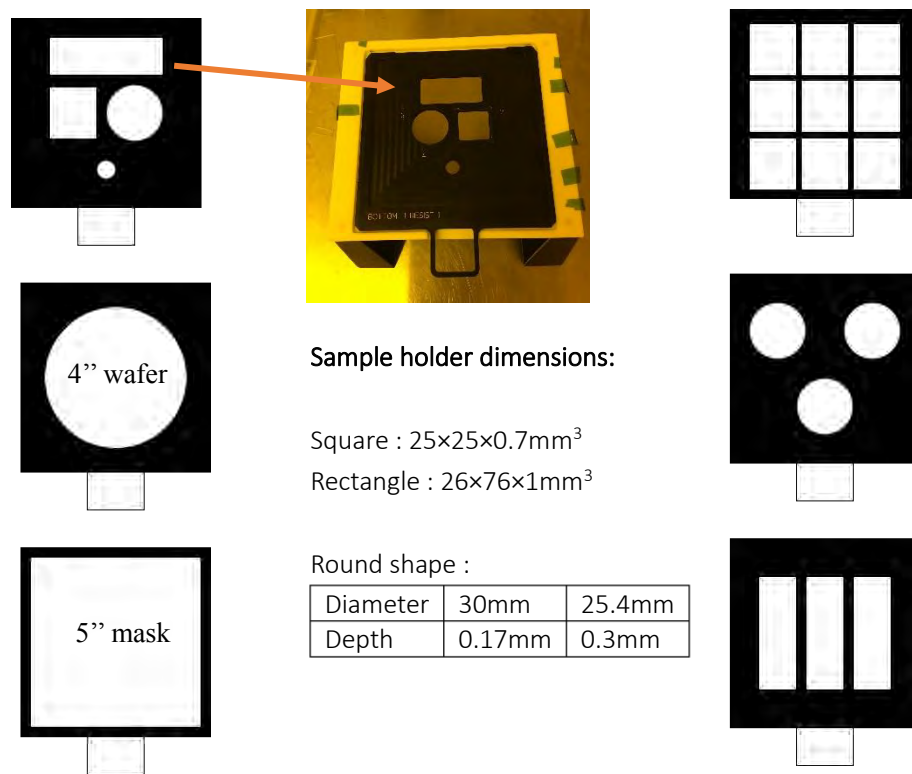


Figure 40. Different sample holders provided by Nanoscribe.

In some cases, considering about the sample position and its shape, the interface position is no longer in the default range set. To find the beginning point of writing, the Interface Finder function can be used to drive the objective dip into resist.

The movement of z-drive is controlled by Piezo mode or Galvo mode. In Galvo mode, the movement part is writing laser, so the writing speed is faster. And in Piezo mode, the movement part is the sample holder, it ensures a more stable performance and a higher resolution.

Different objectives are used for different applications. their properties are compared in **Table 6**. The x25 can write faster but lead to a lower resolution, so we use here x63 objective here according to the substrate material and the propriety of photoresist, according to the instructions for use.

The photoresist of choice is the IP-DIP resin from the equipment manufacturer: this resin is well suited to fabrication of optical elements and high aspect ratios. It is designed for so-called DiLL, which stands for Dip-in Laser Lithography, where the objective lens of the equipment is dipped into the liquid resin which acts simultaneously as an immersion medium and a photosensitive material, a technique which is suitable to high-resolution patterning on opaque substrate.

Table 6. Comparison of different objects of Nanoscribe.

Objects	×25	×63
Numerical aperture	0.8	1.4
Working distance	380μm	190μm
Minimal Δn	0.1	0.05
Resolution in XY	1 μm	160nm
Standard configuration	IP-S	IP-Dip

a) Lens design

Due to the nature of the 2PP technology, the pedestal and the micro lens can be designed as a single unit. This design can be done with conventional 3D computer-aided-design (CAD) software. In our case, we used FreeCAD, an open-source parametric 3D CAD software, to design the pedestal and micro lens. The obtained design is then exported as a .STL file, which is a file format commonly used for 3D printing. While the native parametric 3D CAD design is composed of primitives (i.e. a combination of solids like cubes, cylinders, spheres...), the .STL file is an approximated version of the parametric design which uses triangular planes to reproduce the surface geometry of the 3D model. The Nanoscribe uses STL file format as an input, as such the settings for exporting the 3D parametric design to an STL file are critical: coarse settings would lead to large facets and would be detrimental to the overall print quality, while highly refined setting would lead to enormous files and much longer processing while not bringing additional benefits to the print quality. Our settings are a compromise between file size (1.1Mb) and print quality, with a STL file comprising 22284 faces and 11414 vertices. The dimensions and STL files of the pedestal and micro lens are described in **Figure 41-a**.

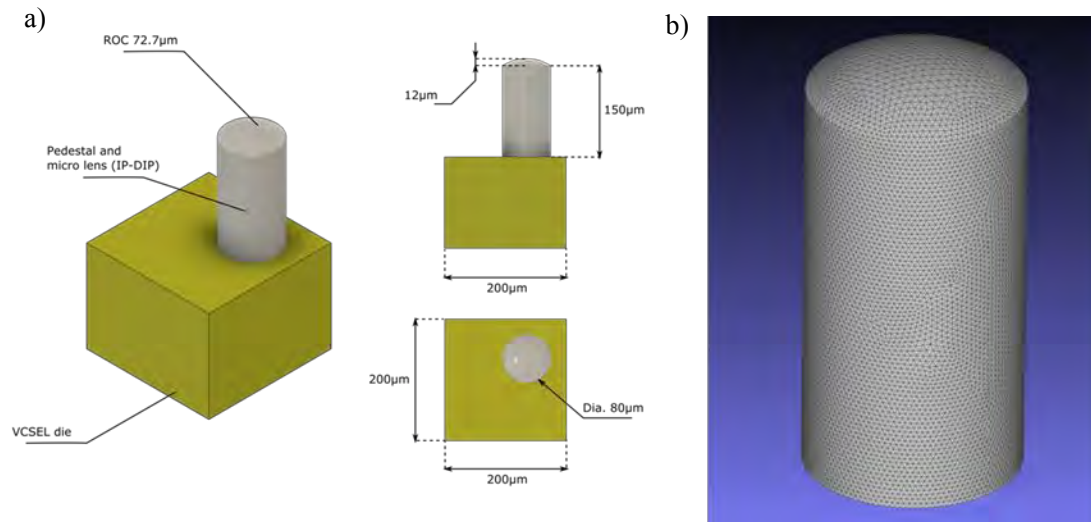


Figure 41. a). 3D CAD representation of the pedestal and micro lens over a dummy VCSEL die, highlighting the dimensions of the micro optical components compared to the VCSEL. b). Illustration of the STL file mesh to be used for the Nanoscribe 2PP equipment, comprising 22284 faces and 11414 vertices.

b) Lens writing conditions

Once the STL file is generated, the file is imported in the Nanoscribe software named DeScribe. This software will interpret the STL file in order to prepare the print job, according to customizable recipes including parameters like slicing distance (horizontal layers thickness), hatching (parallel lines distance), scan speed or printing strategies. Writing settings in 2PP (like other laser-based additive manufacturing technologies) is always a compromise between time and resolution. As an illustration, printing time for an 80 μm diameter, 150 μm high pedestal with a micro lens can range to several minutes to several hours depending on the writing settings.

As for all photolithography processes, the calibration of exposure parameter is firstly needed. The dose of exposition is controlled by the writing power and the writing speed. A higher writing speed leads to a lower exposure time, otherwise small bubbles appear at the focused point while writing. The setting of exposure is also related to the magnification of objective. When using a higher magnification objective, the exposure power should be decreased appropriately. Additionally, the optimal value varies with the surface state of substrate. For example, the power exposed on a metal surface should be much lower than a polymer surface, or else an over exposure problem will deformer the 3D printing structure.

A test array of micro pedestals and micro lens was developed on different resolutions, exposure powers and writing speed as shown in **Figure 42**, to find the optimal configuration of writing parameters. With a 500 μm space between two pedestals, the objective can work freely without

destroying the previous structure, this is a favorable condition for the parallel detection system on a real PCB.

The post treatment after exposition is immersing the sample into SU-8 developer solution for 3 minutes under room temperature. After rinsing in an isopropanol solution, the micro structured patterns are obtained.

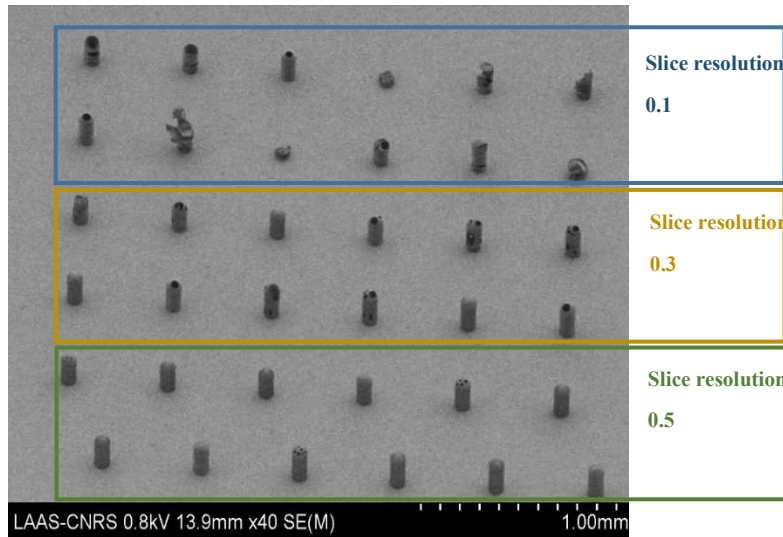


Figure 42. Calibration of exposure parameters for Nanoscribe writing.

We tried the combinations of 100% exposure power with 30/50 $\mu\text{m/s}$ scanning speed, and 63% exposure power with 10/30 $\mu\text{m/s}$ scanning speed. By finding the optimal parameters, the final structures with different slice resolutions are shown in **Figure 43**.

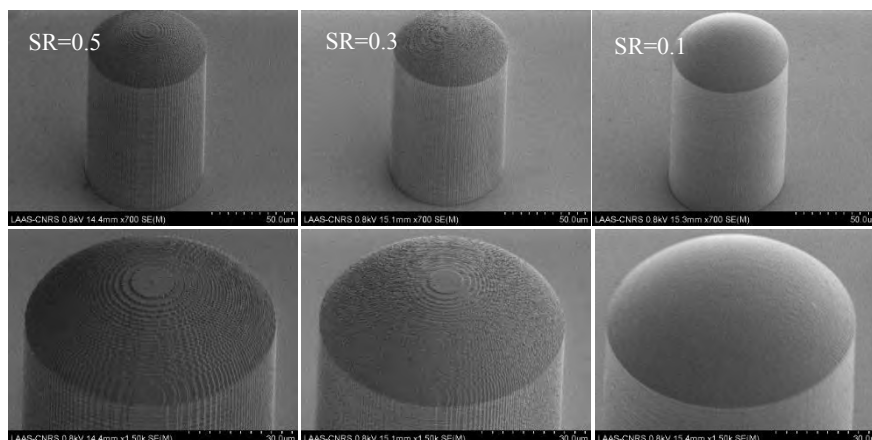


Figure 43. Micro pedestal and micro lens fabricated by 3D printing in three different slice resolutions.

According to the SEM images, the surface of micro lens made by 3D print is as expected less smooth than with the inkjet method, we can see layered patterns that follow the order of exposure changing with the set slice resolution. For an optimal structure as simulated in **Table 4**: the height of pedestal is $80\mu\text{m}$ and the arch height of micro lens is $18\mu\text{m}$, the writing time with a 0.5 resolution is only several minutes, but with a 0.1 resolution, the process sustains several hours.

These test samples are currently under study in a laboratory specialized in micro-optical elements characterization (TONA-VUB Brussels).

To save time, we applied the 0.5 resolution conditions to VCSEL chips mounted on PCB (**Figure 44**). If the surface roughness does not affect the subsequent optical effect, a concession for time can be made here. When applied to the VCSEL surface, the reflectivity of surface has to be considered to adjust the writing parameters, and a more complicated focusing process is needed on non-standard thickness substrates.

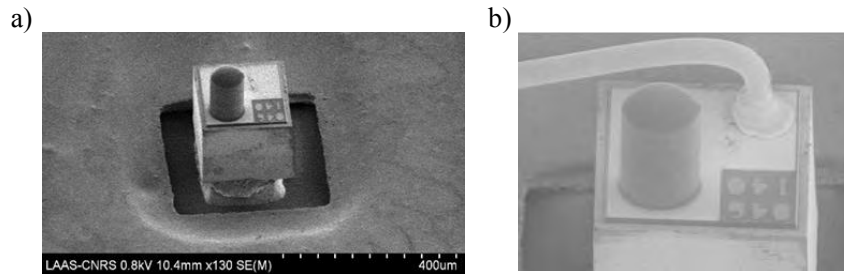


Figure 44. View of a VCSEL chip with a 3D printed lens in single step before (a) and after (b) wire bonding.

As this technique is applicable on the surface of VCSEL chips directly at a post mounting/assembly stage, another paste method was proposed by Samuel Charlot from TEAM service. The chip can be pasted by side, and this buried structure can provide a better stability (**Figure 45**). During both manipulations, we should take care on the parallelism of the VCSEL surface with the PCB surface, to avoid any tilt.

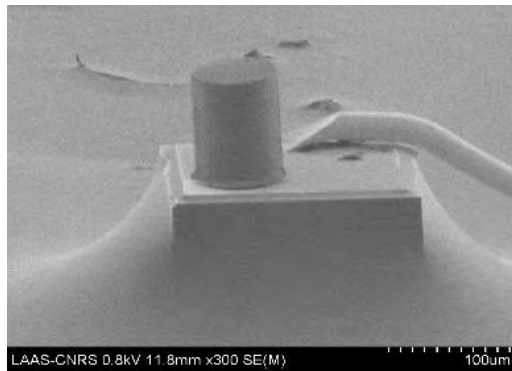


Figure 45. VCSEL with a 3D printed lens and buried on a PCB with a wiring done before lens fabrication.

II.4.3.3 Characterization of lensed devices

a) L-I curve

The L-I curves of VCSEL with and without a 3D printed micro lens are shown in **Figure 46-a**. The polarization selection was also checked for the lensed VCSEL and found higher than 75% as for the first method (**Figure 46-b**).

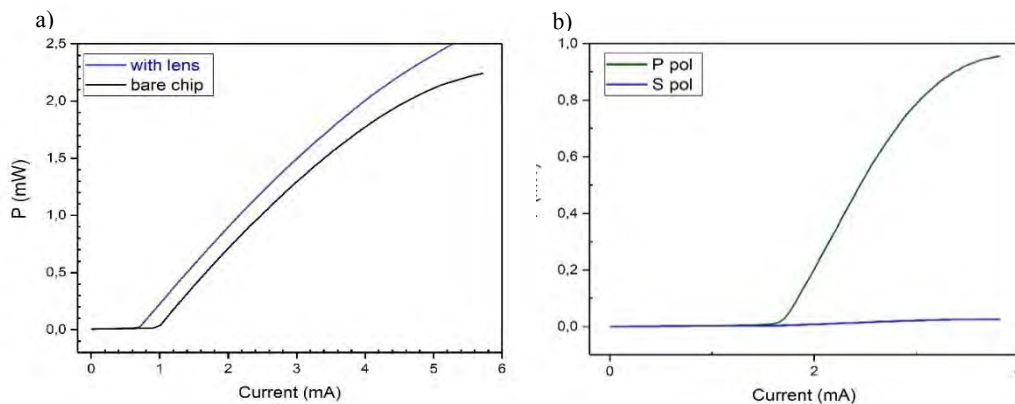


Figure 46. a) L(I) curve of VCSEL with and without 3D printed micro lens. b) Polarization-resolved L(I) curve of VCSEL with 2PP 3D printed micro lens.

Figure 46 illustrates that even though the optical surface is not too smooth with a resolution of 0.5, the output power with micro lens is not significantly influenced by scattering, neither the polarization behavior.

b) Beam divergence

By using the optical characterization bench illustrated in **Figure 36**, the divergence of VCSEL with or without micro lens fabricated by 2PP 3D printing was measured (**Figure 47**). The output light divergence has been significantly reduced, from around 14 degrees to ~3 degrees, and the diameter of light spot at 2mm distance is about 54 μ m, these values also fit very well with the simulation results.

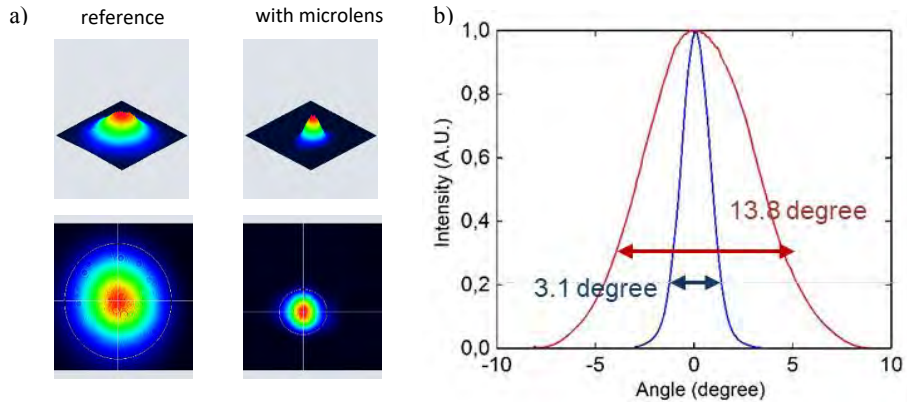


Figure 47. a) Beam profiles without and without microlens measured at 3mA. b) Divergence of VCSEL with or without micro lens fabricated by 2PP 3D printing.

Concerning the impact of the surface roughness that is induced due to the scanning nature of the 2PP technology, we can see that even though the surface of the 3D printed micro lens is expected to be less smooth than the one fabricated by inkjet writing, it does not affect significantly the output power and the collimated divergence. So, there is no need to further increase the 3D print resolution. In this case, the writing process can be finished in several minutes.

c) Tuning range after 3D-printed lens fabrication

The evolution of the emission spectrum as a function of the applied current was measured after lens integration with the 3D-printing method **Figure 48**. Thanks to the collimation effect, the power collected by the fiber is much higher than for the case of the reference chip. However, the transverse mode behavior is slightly degraded. The relative intensity of the second order mode is indeed found to be higher for currents above 5.5mA. This can be accounted for the fact the polarization grating dimensions were optimized for achieving a single mode emission in the air and not in a polymer medium [90]. This issue could be solved by using dedicated VCSEL chips with an optimized grating for an output emission in the polymer. Nevertheless, the SMSR remains higher than 10dB for applied currents up to 5.5mA. This corresponds to a tuning range of ~3nm, which is still sufficient for our application.

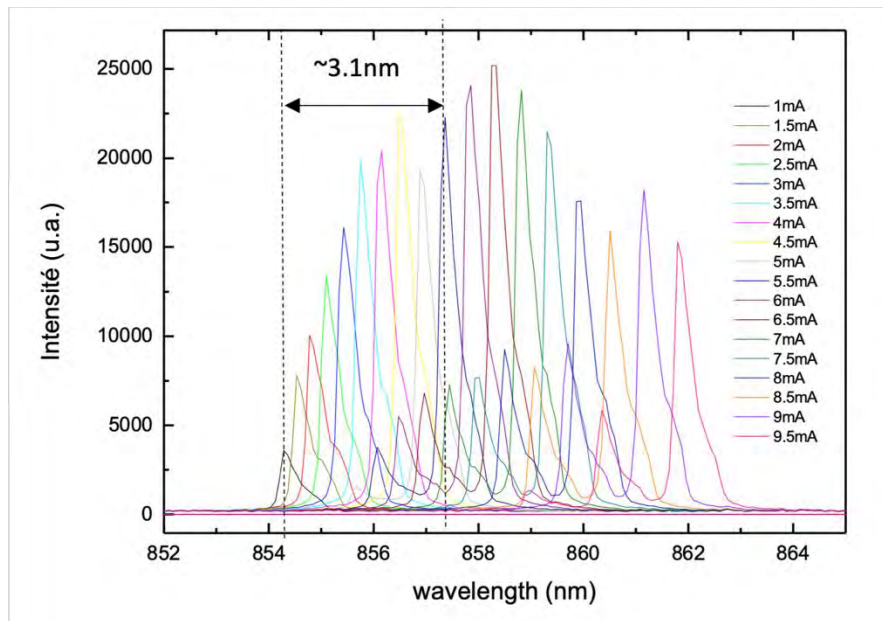


Figure 48. Evolution of the emission spectrum of VCSEL with 3D printing micro lens according to the applied current

II.5 Conclusions on lensed VCSEL source fabrication

To conclude, the experimental results of inkjet writing method and 2PP 3D printing method show that all above-mentioned polymer materials being used are transparent in the near infrared band, especially near 850nm, and are suitable and stable for the operating process.

By using two different methods and targeting the previously micro lens design, we successfully managed to reduce the VCSEL divergence to about 3 degrees at $1/e^2$, as needed for our microsensor. This compact laser source emits a single mode Gaussian beam with an optimal 60 μ m size at 2mm distance and can be spectrally tuned over 3nm under current adjustment.

Table 7 lists the comparison of performances between both methods. Considering all the factors above, as the 3D printing method that was developed for the first time in the framework of this thesis [91] presents the advantages of fast manufacturing cycle, being operated at room temperature without heating, and in a single step, we selected it as a preferred fabrication method for our system. A coarse resolution of 0.5 μ m can indeed totally satisfy our requirements, with which the microstructure for collimation can be processed in several minutes on a post-assembly VCSEL chip.

Table 7. Comparison of performances between both methods.

	DLW+Inkjet printing	3D printing
Processing period	Few days	< 10 minutes
Heating requirement	120°C	room temperature
Surface roughness of micro lens	very low	middle
Pedestal shape	not perfect cylinder	accurate
Repetition	middle	very high
Operational complexity	middle	low
Acceptability for pre-soldering	No	Yes
Alignment	500nm	1µm

Chapter III

Analytical models and simulations of optical gas sensor

III. Analytical models and simulations of optical gas sensor

As illustrated in **Figure 49**, our microresonator is composed of a tapered SU-8 waveguide, two aluminum grating couplers for light injection and signal extraction, and a vertically coupled SU-8 microring that will be furthered functionalized for gas sensing. In this chapter, the size of each part will be calculated in detail by analytical models and software simulation.

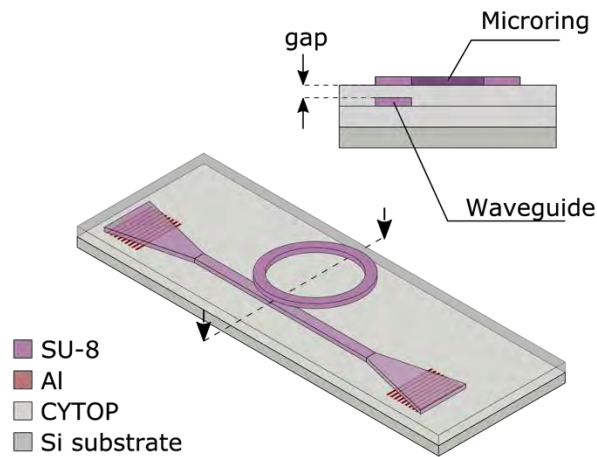


Figure 49. Schematic of the microresonator, including tapered waveguides, grating couplers and a vertically coupled microring.

III.1 Waveguide dimension calculations for single-mode transmission

A single-mode waveguide is required to avoid detrimental inter-mode interaction effect in the final spectrum. Considering the refractive index of selected materials and the operating wavelength, the range of dimension can be calculated with the method below.

To obtain a single-mode propagation, it is necessary to establish and solve the eigenvalue equation under fixed optical-geometric conditions. The theoretical study begins with a 3-layer planar structure (1D), in order to determine the ideal thickness of the SU-8 polymer core in guiding layer. The diagram is shown in **Figure 50**.

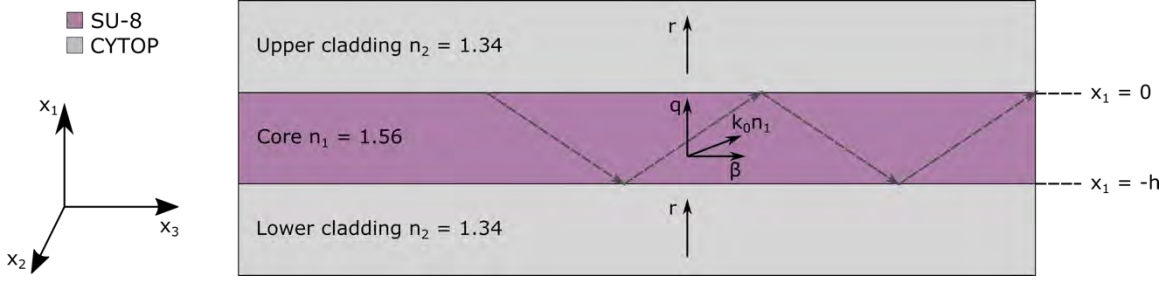


Figure 50. The 3-layer planar waveguide and its associated relative wave vectors.

The Helmholtz equation solution in different regions allows us to determine the expression of optical modes and the distribution of energy. To simplify the problem, the waveguide is supposed to be perfectly homogeneous in the (x_2, x_3) plane. The waveguide is considered as infinite along x_2 , so the contribution of type $\frac{\partial}{\partial x_2}$ and $\frac{\partial^2}{\partial x_2^2}$ will be zero. The light propagates along x_3 . The discussion starts with the TE mode, the electric field being oriented along the x_2 axis.

For a TE polarized optical wave, the components of electric field vector and magnetic field vector are $\vec{E}(0, E_{x_2}(x_1)e^{j(\omega t - \beta x_1)}, 0)$ and $\vec{H}(H_{x_1}(x_1)e^{j(\omega t - \beta x_1)}, 0, H_{x_3}(x_1)e^{j(\omega t - \beta x_1)})$, with ω the pulsation of wave and $\beta = k_0 n_{\text{eff}}$ the projection of propagation along the x_3 axis. Then the Helmholtz propagation equation in the three different layers ($i = 1, 2$) can be simplified as:

$$\frac{\partial^2}{\partial x_1^2} E_{x_2}(x_1) + (k_0^2 n_i^2 - \beta^2) E_{x_2}(x_1) = 0 \quad (4)$$

The continuity of the field TE at the interface CYTOP/SU-8 (at $x_1 = 0$ and $x_1 = -h$) gives the solutions of E_{x_2} as:

$$E_{x_2}(x_1) = \begin{cases} C e^{-r x_1}, & x_1 \geq 0 \text{ (upper cladding)} \\ C \cos(q x_1) + K \sin(q x_1), & 0 \geq x_1 \geq -h \text{ (waveguide)} \\ [C \cos(h q) - K \sin(h q)] \cdot e^{r(x_1 + h)}, & x_1 \leq -h \text{ (lower cladding)} \end{cases} \quad (5)$$

With $q = \sqrt{(k_0 n_1)^2 - \beta^2}$ and $r = \sqrt{\beta^2 - (k_0 n_2)^2}$ the wave vectors, C and K being integration constants. The field has an oscillating shape in the waveguide (field confinement) and decreases exponentially (evanescent field) in the cladding.

According to Maxwell's equations, the magnetic field of the TE mode along x_3 axis can be expressed as:

$$H_{x_3}(x_1) = \begin{cases} \frac{jrc}{\mu_0\omega} e^{-rx_1}, & x_1 \geq 0 \\ \frac{jq}{\mu_0\omega} [C\sin(qx_1) - K\cos(qx_1)], & 0 \geq x_1 \geq -h \\ -\frac{jp}{\mu_0\omega} [C\cos(hq) - K\sin(hq)] \cdot e^{p(x_1+h)}, & x_1 \leq -h \end{cases} \quad (6)$$

Then these expressions can be used to derive the eigenvalue equation of propagation mode. Using the condition of continuity for the magnetic field tangential component at the interfaces ($x_1 = 0$ and $x_1 = -h$), the constants C and K are eliminated, the equation being simplified as:

$$hq - 2\arctg\left(\frac{r}{q}\right) = n\pi \quad (7)$$

with n an integer and a quantization number that represents the mode order.

With the same method, the components of electric and magnetic fields for the TM mode (the magnetic field being oriented along the x_2 axis) are $\vec{H}(0, H_{x_2}(x_1)e^{j(\omega t - \beta x_1)}, 0)$ and $\vec{E}(E_{x_1}(x_1)e^{j(\omega t - \beta x_1)}, 0, E_{x_3}(x_1)e^{j(\omega t - \beta x_1)})$, so the final equation related to the thickness of the waveguide layer will be:

$$hq - 2\arctg\left(\frac{n_1^2 r}{n_2^2 q}\right) = n\pi \quad (8)$$

In this equation, n presents the mode order. Therefore, the cut-off thickness, that is the minimum thickness of the guiding layer necessary for the propagation of wave of the TE_n and TM_n modes, are:

$$h^{TE_n} = \frac{1}{q} [\arctg\left(\frac{r}{q}\right) + n\pi] \quad (9)$$

$$h^{TM_n} = \frac{1}{q} [2\arctg\left(\frac{n_1^2 r}{n_2^2 q}\right) + n\pi] \quad (10)$$

Based on these equations, a Matlab program has been written to plot the dispersion curves of eigenmodes versus the guiding layer thickness, illustrated **Figure 51**.

In this three-layer structure, the effective indices grow with the thickness. As higher effective indices are always appreciated for a better sensitivity, for keeping a higher sensitivity but staying in single-mode configuration at the same time, a SU-8 waveguide thickness less than 800nm will be favored.

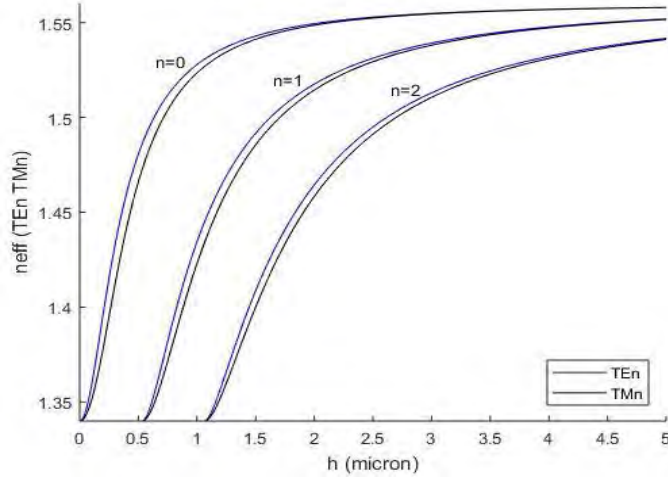


Figure 51. Dispersion curves@850nm of TE_n and TM_n modes in a three-layer structure CYTOP/SU-8/CYTOP versus the guiding layer thickness.

With the same method, we can use a 2D model to find out the optimal width of the waveguide for single mode propagation. In this case, it is necessary to transform the TE mode and the TM mode of the previous case, as shown in the top view of the guiding plane **Figure 52**.

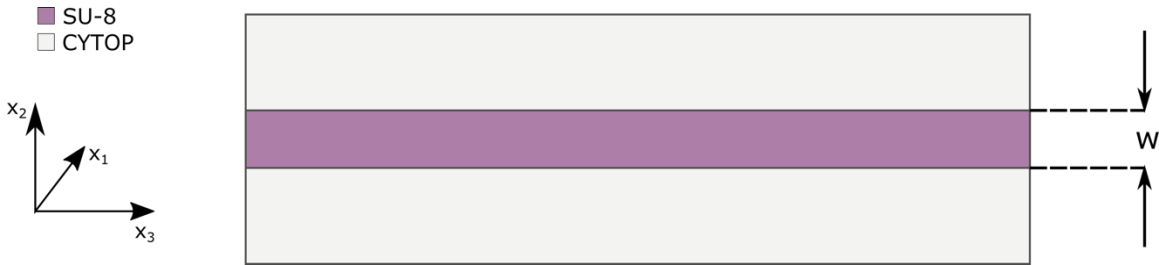


Figure 52. Top view of the guiding plane.

The width of the SU-8 waveguide, noted w , works as the thickness h in the previous situation:

$$wq' - 2\arctg\left(\eta \frac{r'}{q'}\right) = m\pi \quad (11)$$

with $\eta = 1$ for TM mode, $\eta = n_{\text{eff}}^2/n_2^2$ for TE mode. $q' = \sqrt{(k_0 n_{\text{eff}})^2 - (k_0 n_{\text{eff}}')^2}$, $r' = \sqrt{(k_0 n_{\text{eff}}')^2 - (k_0 n_2)^2}$, m being the wave mode order and n_{eff}' the effective index in the 2D

waveguide. We then calculate the dispersion curves of $n_{\text{eff}}' = f(w)$ with Matlab using the aforementioned method, and obtained the results shown **Figure 53**.

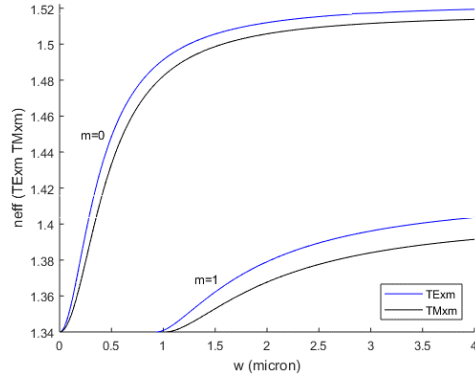


Figure 53. Dispersion curves at 850nm of TE_{xm} and TM_{xn} modes in a three-layer structure CYTOP/SU-8/CYTOP. The thickness of layer SU-8 is less than 800nm.

Based on previous experience on the Canon FPA 3000i4, the UV (365nm i-line) projection stepper available in the LAAS-CNRS cleanroom, a minimal waveguide width of $1\mu\text{m}$ has been defined in order to obtain waveguides edges and cross-sections of good quality with layer thicknesses below 800nm.

By considering the dispersion curves above and our technological constraints, we can select a suitable range for the waveguide width to guarantee single-mode operation with the aforementioned materials. Based on these calculated ranges of width and thickness, we then proceed to a parametric analysis using a commercial modeling simulation software named Lumerical (MODE Solutions module) to find the best compromise. This parametric analysis has finally led to a 400 nm high, $1\mu\text{m}$ wide waveguide.

In the next paragraphs, we will determine through the use of Lumerical FDTD simulations the optimum dimensions for the grating couplers, the tapers, the microring (radius, gap) and the CYTOP lower cladding thickness, that will all have an influence of the final performance of the sensor. The range of waveguide dimensions that we determined in this section will be used as a working basis.

III.2 Design of grating coupler

With the idea of a portable, integrated micro-system, we decide to use a VCSEL as the optical source for our optical sensor. While recent developments in 3D printed structures [88] shows some promising results for light coupling, these strategies are low-throughput compared to wafer-scale,

collective manufacturing techniques. While the VCSEL source, or the photodetector in our system can be considered as reliable parts with long lifetime, we furthermore considered that the microring resonator should be replaceable, for example in the case of a degradation of the sensitive layer or a pollution of the sensor. We therefore choose to use more conventional grating couplers, to obtain better tolerance to misalignment between the source and the waveguide input as well as simplify the usually complex apparatus required for injecting light into micronic or sub-micronic structures.

For a grating coupler illustrated in **Figure 54**. Schematic diagram of a simulated output grating coupler. , we can use the formula $\sin\theta = \frac{n_{eff} - m\lambda/a}{n_{cladding}}$ to obtain a rough estimates of its geometrical parameters, where θ is the incident angle of the VCSEL beam, n_{eff} is the effective index, m is the order of diffraction series, λ is the wavelength, a is the grating period and $n_{cladding}$ is the refractive index of cladding. We take $m=1$ so that only 1 order is supported. For a given wavelength of the excitation source and materials, the design parameters of a grating couplers include period, duty cycle, etch depth and thickness of the waveguide layer, which will influence the effective index. According to the formula, the optimal incident angle of the excitation source grows with the decrease of the grating period. On one hand, we want to make the incident angle as small as possible to simplify the injection setup; on the other hand, we are limited by the stepper lithography equipment that does not offer sufficiently high resolution to obtain grating periods of 700 nm or less. Considered both practical and technological constraints, we considered that a 800 nm period combined with a θ of less than 20° represent appropriate parameters.

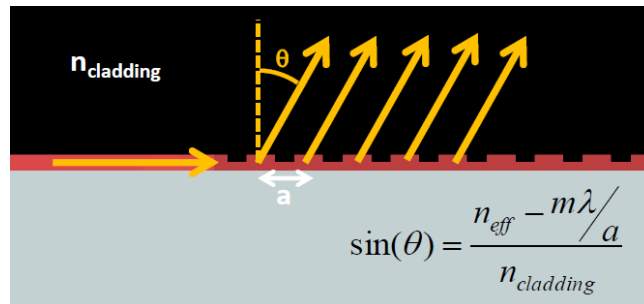


Figure 54. Schematic diagram of a simulated output grating coupler.

We modelled the structure with two source-detector setups. In the first setup, the light enters the waveguide from the left (in-plane butt coupling) and then is diffracted by the grating in a specific angle (θ). This first setup helps us to find the optimal configuration of the grating coupler like grating period, duty cycle, etch depth and so on. Then in the second setup, the light enters from the top of the grating coupler (vertical coupling) and is then diffracted and guided into the waveguide core (SU-8). This model is used to simulate the optimal position and incident angle of the VCSEL source beam. The collection of the coupled signal in the waveguide layer along the direction of propagation (the direction of propagation of light in the waveguide plane is the same as the component of source in the same plane) requires a longer grating period, which is favorable for the fabrication, so we focused on this case.

Following the considerations above, the schematic view of the structure simulated using Lumerical FDTD is given in **Figure 55**. The Si/CYTOP/SU-8/CYTOP structure is in two-dimensions to save the time of calculation and to ease the computer memory pressure.

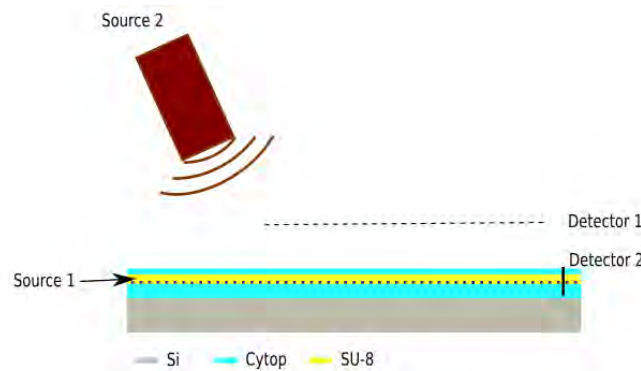


Figure 55. Schematic of the model simulated with Lumerical, showing the two input sources, and the position of the two detectors used in the simulation to optimize both output (Source 1 + Detector 1) and input (Source 2 + Detector 2) grating couplers.

Since the VCSEL surface includes a surface grating, the polarization of the source is stabilized, and this maximizes the light entering the grating coupler. The preferred output pattern for the VCSEL to maximize the coupled power will be quasi-TE mode. This is also beneficial for the micro ring as TE modes always offers a better-quality factor, and by extension better sensitivity (although those two are not always directly correlated) according to the simulation results.

In the first configuration representing the output grating coupler, where the Source 1 and Detector 1 are active, we tried a nested loop structure simulation including the following parameters of the grating coupler: period, duty cycle, grating depth and the waveguide thickness. That means each parameter will be scanned in a reasonable scale: for example, the duty cycle will take values of 0.2 to 0.8 with a 0.1 step, while the waveguide thickness varies from 400 nm to 800 nm with a step of 50 nm, and the grating depth varies from 0 to the thickness of waveguide, with a step of 50 nm. The software will try every combination and then gives the optimal match.

If we use four variables, we have four levels of nesting, that configuration will take a lot of time to do the simulation. To simplify the calculation, we choose to set the thickness of the CYTOP lower cladding layer, which lies between the Si wafer and the SU-8 waveguide layer, at a thickness several times higher than the 850 nm emission wavelength so it does not influence the coupling efficiency of light into the waveguide layer caused by constructive interferences. As the duty cycle of grating coupler have a moderate effect on the coupling efficiency compared to the other parameters, while also being tricky to control accurately in the manufacturing process which involves in a chemical etching processes, its initial value is arbitrarily set as 0.5, while the grating period is fixed at 800 nm as discussed in the paragraph before due to manufacturing constraints. In that configuration the simulation is reduced to two levels of nesting, which reduce a lot the pressure on computer memory and lead to more practical simulation times.

According to the parameter sweep, with a duty cycle of 0.5 and a grating period of 800 nm, an optimal waveguide layer thickness around 400 nm gives the best coupling efficiency over the VCSEL operating wavelength range shown **Figure 56**. Considering a fabrication tolerance of (± 50 nm) still guarantee coupling efficiencies above 12%. Besides, the height of the aluminum grating coupler from 40 nm to 60 nm does not have too much effect on the coupling efficiency and should be relatively easy to guarantee during the fabrication process as it translates to a tolerance of roughly 20% on the aluminum layer thickness which is obtained by PVD.

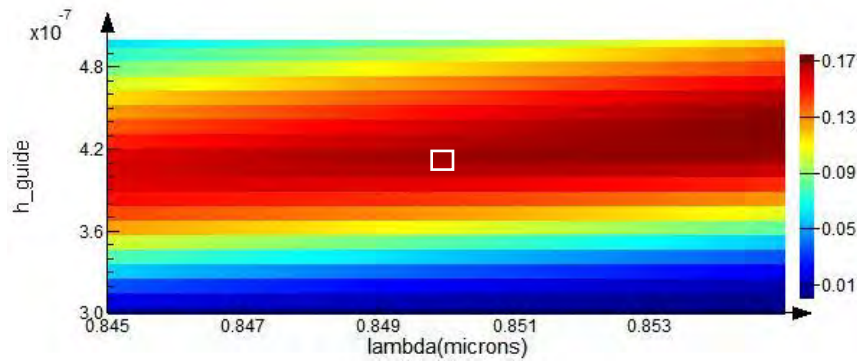


Figure 56. Coupling efficiency of the grating coupler versus waveguide thickness.

This estimation of coupling efficiency provides us the freedom for choosing the photodetector to be used. The emission power for a topical VCSEL can reach 500 μW ; even after passing two grating couplers as incident port and exit port with a coupling efficiency at 10% for each, the emergent power should be about 5 μW . Considering that a standard Si photodiode has a typical responsivity above 0.55 to 0.65 A/W @ 850 nm, the power obtained at the output grating coupler will translate to a current in the range of a few μA which will be easily converted to an usable voltage using a transimpedance amplifier with a 1 M gain. Another advantage of using a 850 nm VCSEL source is that Si photodiodes have an optimal responsivity around these wavelengths. As Si photodiodes or Si-based photodetectors are ubiquitous, this gives us plenty of options for cost-effective integration of the detector in the microsystem.

On the following step, we study how the spot size of the VCSEL excitation light source affect coupling efficiency, based on Source 2 and Detector 2 described in **Figure 55**, with an incident angle value of 19° . The influence on coupling efficiency caused by the dimension ratio between the VCSEL collimated beam size and the grating coupler size is computed in **Figure 57**: a maximal coupling efficiency is obtained for a dimension ratio between the beam spot and the grating coupler in the range of 0.6 to 0.8. Considering the propagation of the VCSEL source after collimation, the optimal diameter of light spot will be under 60 μm at a working distance of 2 mm, so the initial size of grating coupler will be 100x100 μm .

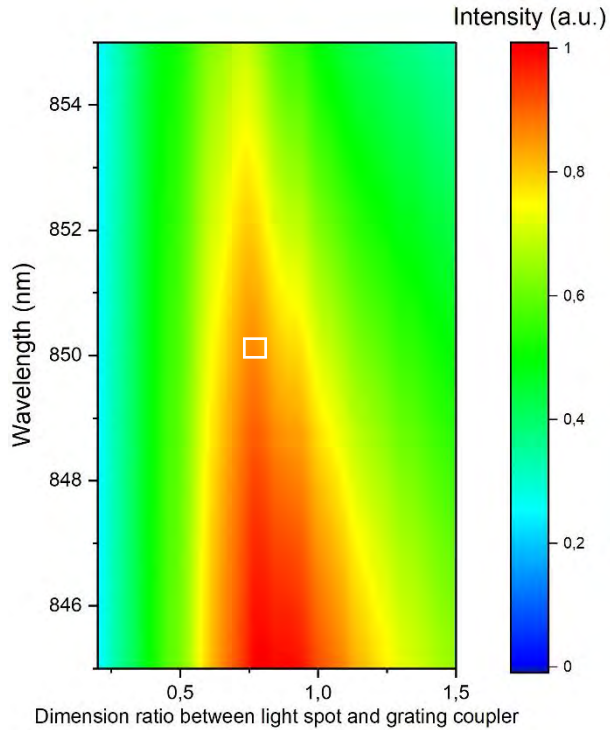


Figure 57. The influence of the dimension ratio between light spot and grating coupler on coupling efficiency.

III.3 Taper waveguide dimensioning

Based on previous experiments and additional calculations with Zemax, the VCSEL will form a light spot on the surface of the grating coupler in a shape of a 60 μm diameter circle at a working distance of 2 mm. The previous coupling efficiency study shows that a grating coupler area of $100 \times 100 \mu\text{m}$ would give a good compromise: this means the width of the grating coupler should be much wider than the width of the waveguide which has been fixed at 1 μm . Therefore, a taper waveguide is required between the grating coupler and the single-mode waveguide to ensure a smooth mode transition.

The taper transmission efficiency depends on its length-to-width ratio: from our simulations shown **Figure 58**, we can see that for ratios above 8, transmission efficiency is maximized and reach a plateau. Considering the 100 μm width of our grating coupler and the 1 μm width of our single-mode waveguide, a transition length of 1 mm is chosen, giving a ratio of 10:1, thus guaranteeing no additional efficiency losses from the taper waveguide.

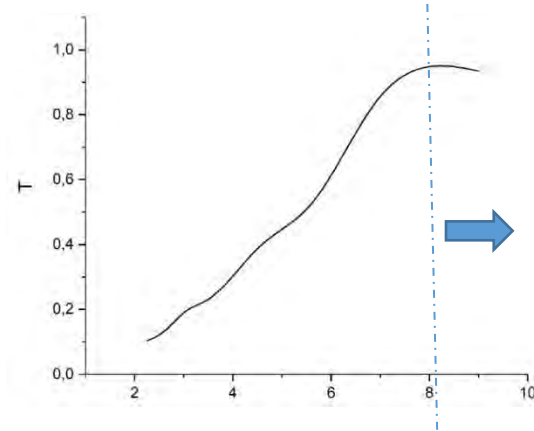


Figure 58. Taper guide transmission efficiency as a function of the length to width ratio.

III.4 Calculation of micro-ring radius

The resonant modes trapped by the micro-resonator circulate according to the standing wave condition: $P=m \cdot \lambda_{\text{eff}}$, with P the geometric perimeter of the micro ring, m an integer and λ_{eff} the effective wavelength of the light in the resonator. It is defined as $\lambda_{\text{eff}}=\lambda_0/n_{\text{eff}}$, n_{eff} being the effective index defined as the solution associated to the quantified resonant eigen mode.

For two adjacent resonant eigen modes, they follow a relation as: $P \cdot n_{\text{eff}} = m\lambda = (m - 1)(\lambda + \text{FSR})$, with FSR the free spectral range defined as the spacing in optical wavelengths between two successive resonance peaks in the output signal. If we replace m by $\frac{P \cdot n_{\text{eff}}}{\lambda}$, then we can get $\text{FSR} \cong$

$\frac{\lambda_0^2}{P \times n_{\text{eff}}^2}$ as an approximate result. This formula illustrates that the FSR in the output signal is mainly related to the perimeter of the micro-ring with a relation of inverse ratio: the bigger the perimeter, the smaller the FSR.

The 850 nm VCSEL source typically offers a maximal spectral tunability of 7 nm. The emission wavelength can be adjusted with the temperature (0.06 nm/°C according to the datasheet) and can also be tuned by adjusting the current to a lesser extent (0.2 nm/mA) [92]. In order to be able to monitor the resonance peaks, and based on a calculated FSR, the micro ring resonator geometric perimeter P is calculated so that two peaks can be covered by the VCSEL spectral tunability, i.e. $\text{FSR} < 6\text{nm}$. Considering a 2 to 3 nm FSR, this leads to an estimated radius of 30 μm (**Figure 59-a**), which should be adapted to the whole sensing system. This diameter is relatively typical for a

micro ring resonator, being large enough to limit propagation losses linked to bend radius, while still offering a compact size for better integration.

Although it was later proved that the tuning range of lensed VCSEL reduces to 3nm, we can adjust the radius to 60 μm to adapt to this change (**Figure 59-b**).

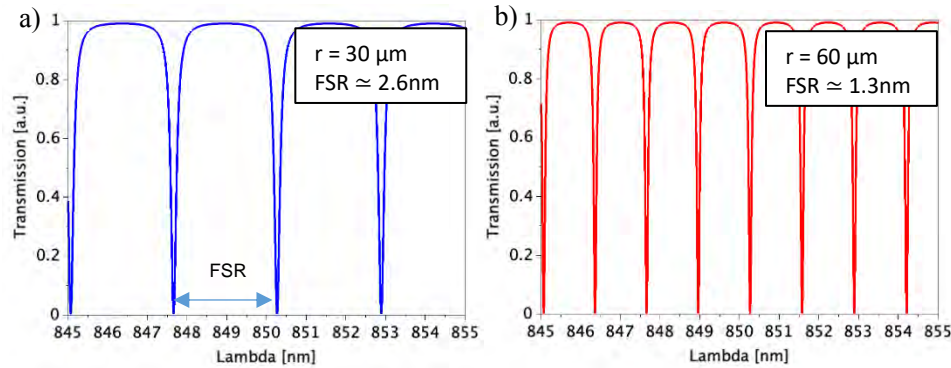


Figure 59. Quantized resonance modes of a conventional micro resonator besides a mono-mode waveguide

Due to the vertical coupling scheme chosen here, and the use of stepper photolithography, several ring diameters can be incorporated in the photomask without changing the design of the other micro-resonator elements. The FSR can also be adjusted in the future to be adapted to a different excitation source with smaller tunability for example. Changing the micro-ring diameter will affect the vertical coupling with the waveguide, but thanks to the vertical coupling scheme, the gap is obtained by etching the CYTOP upper cladding, so it can be tuned without modifying the photomask to recover the required coupling conditions.

III.5 Calculation of the vertical gap between the waveguide and the micro-ring resonator

The gap between the single-mode waveguide and the micro-ring resonator is an important factor to consider as it defines the coupling regimes: under-coupling, critical coupling, and over-coupling. In a vertical coupling scheme, the gap distance is set by the upper cladding thickness (CYTOP in our case). The 2D analysis or the 2.5D analysis mode of Lumerical are not appropriate for the vertical coupling configuration; however, due to the heterogeneous dimensions between the waveguide length (mm range), the ring diameter (tens of μm) and the gap (nm range), simulating the whole device in 3D analysis is not feasible using standard computing power due to the required meshing. To overcome this practical limitation, we simulate only the coupling region in 3D. This

allows us to estimate the coupling conditions and a range of appropriate gap dimensions between the single-mode waveguide and the ring resonator.

The radius of micro ring is fixed at $30\mu\text{m}$ in the simulation as it provides a suitable FSR, adapted to the VCSEL source tunability as seen in the previous section. Empirically, a larger radius will give a higher contrast in the output signal. The greater the radius is, the bigger the optimal gap for critical coupling will be as it will generate more overlap area between the evanescent field coming from the waveguide and the ring.

When light pass through the waveguide, the microring close to it will capture a fraction of the signal through the evanescent wave; this is referred as coupling. The coupling efficiency between waveguide and microring depends on four factors: the refractive index of material, the waveguide dimension, the gap distance between waveguide and microring, and the geometry (radius) of micro resonator. We set t as the coefficient of self-coupling amplitude; k is the coefficient of coupling amplitude, which will determine the coupled energy intensity into microring, α is the loss per round trip during the circulation in the microring as shown **Figure 60**.

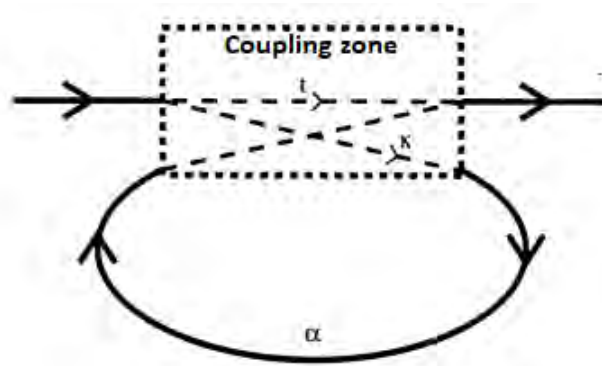


Figure 60. Energy coupling schematic between a waveguide and a lateral micro resonator.

To keep an optimal coupling, which means the contrast in the output signal is maximized, there is a critical coupling condition. Changing the gap influence the energy coupled into the micro resonator: critical coupling is obtained when the coupled energy intensity is equal to the total loss per round trip α in the resonator. We calculate respectively the coupled energy intensity k^2 and the bend loss per lap in the resonator versus the gap dimensions with the simulation software, and then draw the diagram with the calculated data to find the point of intersection which is represented **Figure 61**.

In our situation, the CYTOP/SU-8/CYTOP structure with the radius of micro ring equals to $30\mu\text{m}$ needs an optimal gap of about 180 nm . However, the total loss inside the micro ring is not only affected by the bend loss, but also the surface roughness, the manufacturing defects, losses caused by the interface and the material, which cannot be estimated precisely without experimental characterizations. Since the practical propagation losses are always greater than theoretical

calculation due to fabrication imperfections, we will try several gap values and micro-ring radius around these calculated values: while the micro-ring radiuses have to be fixed by the photomasks. For the radius of 60 μm , a bigger gap will be required; this requirement can be easily fulfilled as different gaps can be obtained by adjusting the etching depth of the CYTOP upper cladding layer with the same photomasks thanks to the vertical coupling configuration.

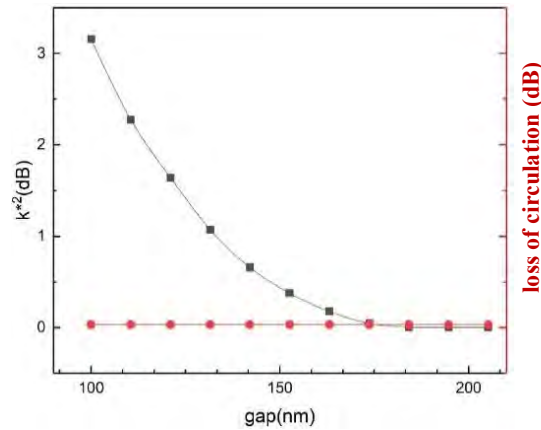


Figure 61. Energy coupling curve of a micro resonator system for different gaps.

III.6 CYTOP lower cladding thickness dimensioning

Another important parameter to be calculated is the CYTOP lower cladding thickness. In order to evaluate the contribution of the reflections at the Si/CYTOP interface that can translates either to constructive or destructive interferences, we studied the coupling efficiency dependence on the CYTOP bottom cladding. This usually translates into a periodic relation between bottom cladding thickness and coupling efficiency as seen in **Figure 62**.

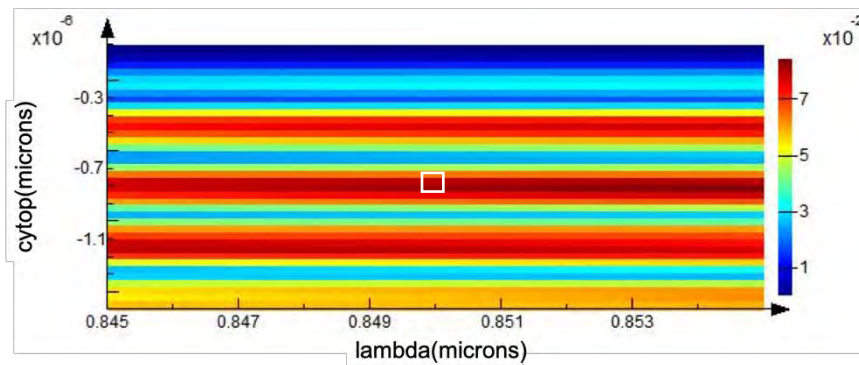


Figure 62. The variation of coupling efficiency versus CYTOP bottom cladding thickness.

The light source position is not optimized in this simulation to reduce nested loops and pressure on computer memory, so the y axis label in this result just shows a trend of change instead of exact

values. From the simulation results **Figure 62**, we can clearly observe that the coupling efficiency can be enhanced for specific thicknesses. Based on a compromise between better optical confinement in the waveguide and manufacturing process capabilities, the optimal bottom cladding thickness is chosen as 800 nm. From our previous experiments in CYTOP deposition and curing conditions, the tolerance of fabrication error range is under ± 50 nm, which translates to less than 10% variation of the overall coupling efficiency.

After all the theoretical calculations, the overall structure of the optical sensor is presented in **Figure 63**, with an overview of the selected materials, their dimensions and their respective tolerances considering the intended fabrication processes. The output grating coupler and its associated taper waveguide is not represented here but the structure is symmetric. A configuration with in-plane output (without the grating coupler and the taper waveguide) will also be included in the fabrication and will be described later in the manuscript.

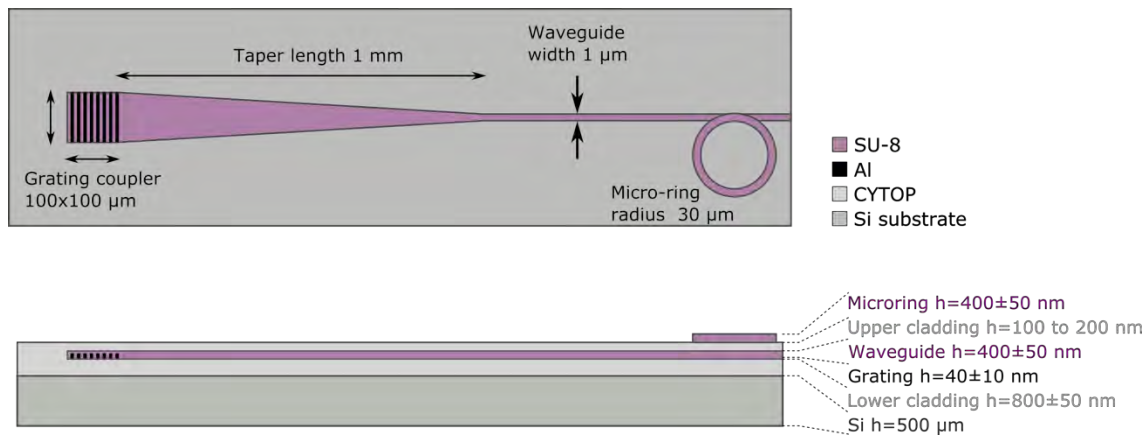


Figure 63. Top view and side view of the detection area of the microsystem.

III.7 Design of the photomasks

For the waveguide output, we will test two configurations to reach the photodetector: out of plane output with an output grating coupler, and in plane output by butt-coupling. This choice has been made to compare the efficiency of these two methods, and in the case of a much lower coupling efficiency of the gratings than expected, could allow us to collect more output power.

Based on the simulation results obtained in the previous section, we proceed to the design of the reticles to be used for the Canon FPA 3000i4 projection stepper. The term reticle is more suited over the term photomask due to the nature of the stepper system, as due to the projection, only a small portion of the wafer is exposed at each exposure; hence for clarity in the following sections the term photomask will be replaced by reticle.

For a photomask used in conventional photolithography with a mask aligner, the standard size usually varies from 2.5×2.5 up to 16×16 square inches. Geometric shapes, generally in chrome, define the dimensions of the devices to be produced at scale one. A stepper differs from a mask aligner in that it uses a projector that shrink the features of the reticle by a factor X which depends on the equipment. The projection is achieved by reduction lenses; the geometric shapes in chrome define the dimensions of the devices to be produced at scale X. The dimension of the reticle are commonly comprised between 4×4 to 8×8 square inches. Here we use a 6×6 square inches reticle, the scale factor being X=5 for the Canon FPA 3000i4 stepper as represented **Figure 64** [93]. The reticle contains several patterns, each of which covering an area of 6.2mm×7.2mm on the wafer. For a standard 4 inches Si wafer, it translates to 114 individual areas that can be exposed in batches with different settings and a combination of patterns. In our case, a complete microresonator will require three levels of photolithography, one for the grating couplers, one for the waveguides and one for the micro-rings.

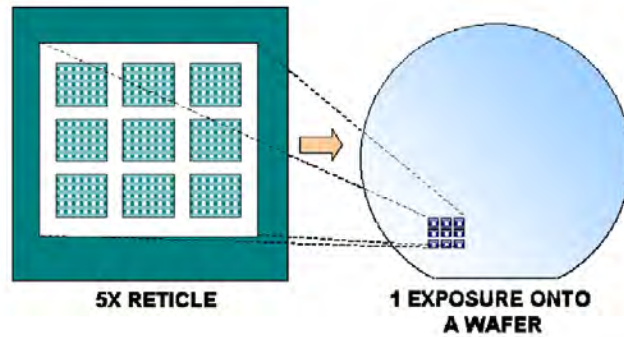


Figure 64. Illustration of the size reduction from the reticle to the exposed wafer. Here the reticle features are designed at scale 5, and the reticle contains 9 patterns. [93]

Based on the dimensions summarized **Figure 63**, a representation of the different areas of the reticle is given **Figure 65**. Seven waveguides can be integrated within one area of the reticle, so we defined several micro-rings radius (from 30µm to 90µm, visible on **Figure 65** (3)) for the final experimental validation, to release the complexity of adjusting the thickness of CYTOP that defines the coupling gap in the later etching part. Generally, a larger diameter needs a larger gap distance, to reach the critical coupling condition. Some waveguides with an increased width of 2 µm have also been included as well as an alternative option. As the 400 nm targeted waveguide thickness is sufficiently small, this increased width should not induce a multimode propagation.

A total of five areas on the reticle (out of the nine available) are used for our design including the two types of input/output configurations: a configuration with out-of-plane light input and in-plane (butt-coupling) output (combination of **Figure 65** (2) and (5)), and a configuration with out-of-plane coupling for both inputs and outputs using identical metallic grating couplers (combination of **Figure 65** (1) and (4)). **Figure 65** (3) contains the micro-rings with various radiuses and can be used for both coupling schemes.

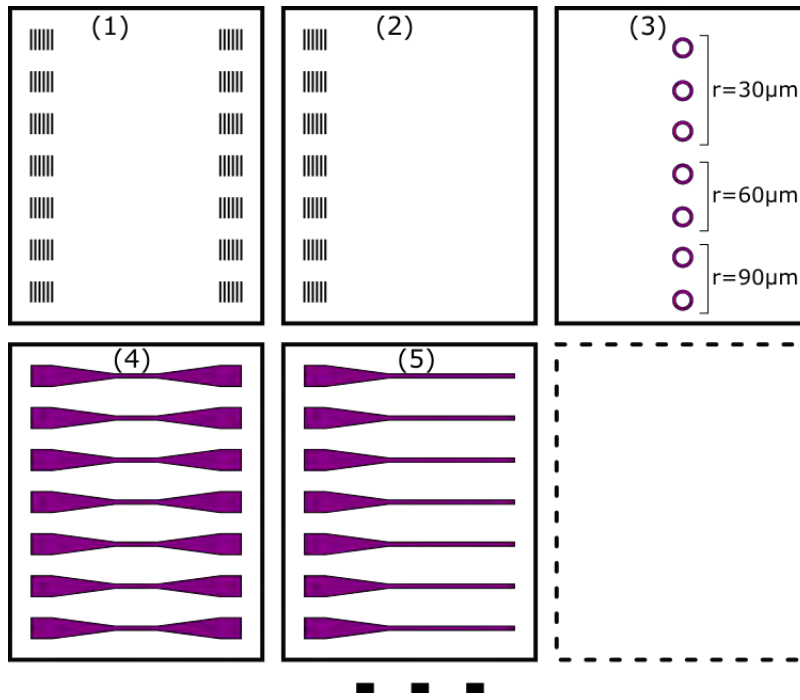


Figure 65. Schematic representation of the five over nine areas available on the reticle. Each pattern will cover a $6.2 \times 7.2 \text{ mm}^2$ on the wafer. A complete micro-resonator will be a combination of three areas of the reticle. Note: the polarity is not respected for better graphic rendering of the schematic.

For the butt-coupling (in-plane) output configuration, as the light outputs by the end of the waveguide, a good quality facet is needed to ensure further light collection. While for inorganic materials this can be achieved by pre-cautious cleaving of the wafer, it is almost impossible to obtain optically correct facets by cleaving polymeric waveguides with polymer cladding. The other option is to define the output facet by photolithography. However, due to the waveguide cross section of about $1 \mu\text{m} \times 400 \text{ nm}$, problems are expected using i-line UV exposure: due to optical effects the desired orthogonal shape of the waveguide end will likely turn into a rounded shape. To improve this problem, we use the software GenISys Lithography Simulation software to optimize the end shape on the reticle and get a better-defined waveguide end. As this kind of simulations is highly demanding in terms of computing power, we simplified the problem by drawing two rectangles with a width of $2 \mu\text{m}$ and $1 \mu\text{m}$ respectively, to simulate the waveguides extremities. Small squares on the corners like illustrated in **Figure 66**, which is a classical correction method to obtain orthogonal shapes in such configurations.

The parameters of the waveguide materials, like the SU-8 photoresist refractive index, as well as the Canon FPA 3000i4/i5 stepper specifications were then configured in GenISys. We use two embedded loops to scan the square size from $0.1 \mu\text{m}$ to $0.5 \mu\text{m}$, and the overlap from $0 \mu\text{m}$ to $0.5 \mu\text{m}$ (**Figure 67**).

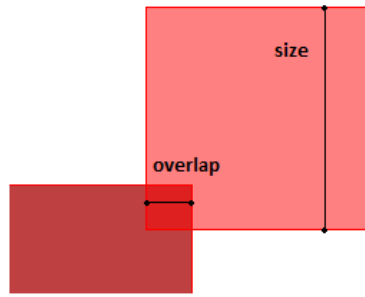


Figure 66. The small squares added on the corner in the simulation.

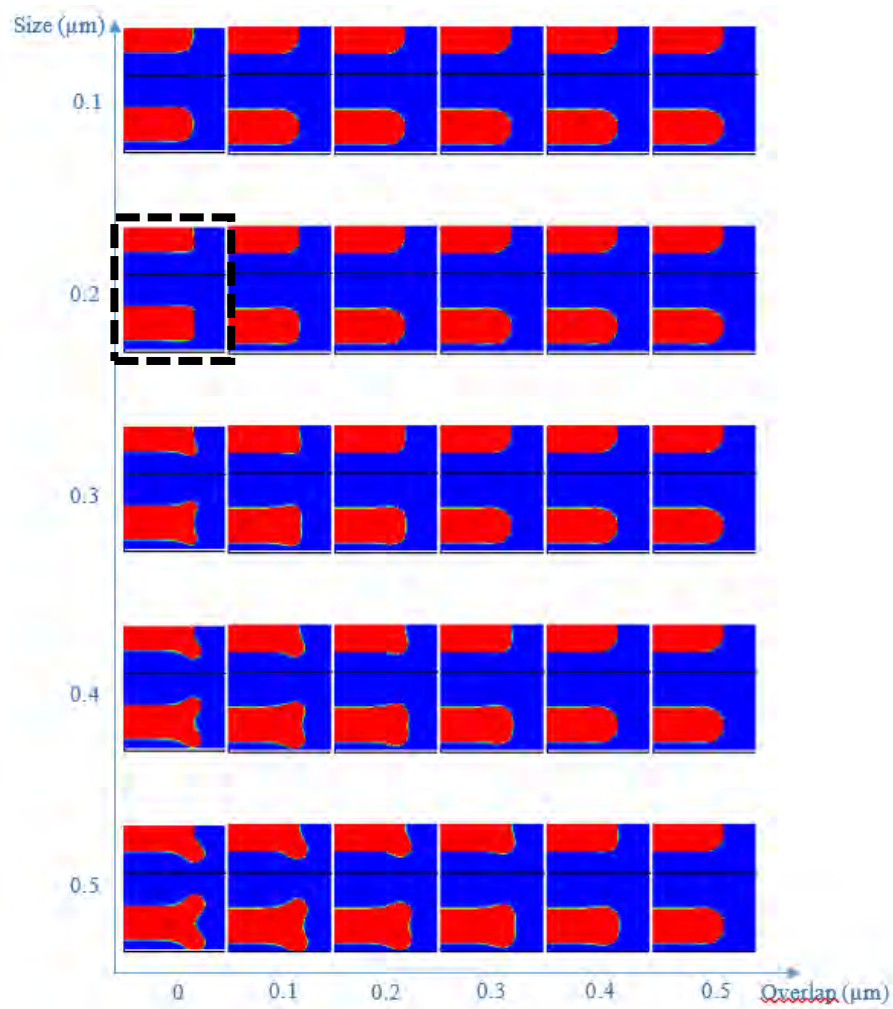


Figure 67. Simulation results obtained with GenISys for different additional square size and overlap with the waveguide extremity. The best configuration obtained at 0 μm overlap and 0.2 μm square size is highlighted.

By analyzing the results provided by the simulation and shown **Figure 67**, we found that the best configuration to get a regular end is when the square's size equals to $0.2\mu\text{m}$ and the overlap equals to $0\mu\text{m}$, so these correcting patterns were added to the waveguide ends whenever it was required.

Chapter IV

Fabrication of the microresonators

IV Fabrication of the microresonators

In this chapter, the different fabrication techniques that have been explored to realize the structure designed in chapter III are presented. By considering all existing materials and equipment in the laboratory, different methods have been evaluated, in particular for the grating coupler part, which requires the highest resolution and is the most challenging part of the process. Advantages and disadvantages among all methods are compared at the end of this section.

IV.1 Fabrication of the reticles for stepper lithography

The reticle is a transparent plate (typically glass or quartz) covered by an opaque surface (typically chrome) which can be engraved with highly detailed designs. The polarity of the patterns is set according to the photoresists that will be used during the exposure (positive or negative). The reticle can contain several patterns that can be selected for projection on the wafer. In our case, a 6×6 square inches reticle divided in 9 areas is used, as described by the schematic **Figure 65**.

Resolution patterns (**Figure 68**) are added at the edge of the reticle: they include horizontal, vertical lines and squares of different sizes and polarities to cover most common resolution issues. As our most challenging pattern is the grating coupler, these resolution patterns are adapted to our needs and kept as is. These patterns are very useful to adjust parameters in the photolithography process, such as the exposure dose, focus depth, and development time.

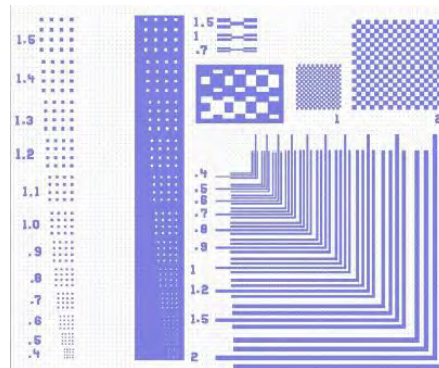


Figure 68. Resolution patterns.

The pattern was drawn by Clewin software, and then generated in .CIF format. The drawing rules depend on the reticle manufacturer and have to be adapted as such. The LAAS CNRS cleanroom is equipped with a Direct Write Laser (Heidelberg Instruments MikroTechnik DLW 2000) system that allows in-house manufacturing of photomasks and reticles. Unfortunately, at the beginning of our work, this equipment suffered several issues that affected its precision, thus our first reticle was made by the Toppan photomask company located in Corbeil-Essonnes, France. They use an American laser writing machine named ETEC Alta 3000, to manufacture high-resolution photomasks and reticles. This type of machine ensures a high resolution of writing because its

FWHM (full width at half maximum) of spot size can be as low as $0.27\mu\text{m}$, the price of the photomask being dependent on the resolution chosen as it impacts the writing time. We chose here a minimum feature size = $0.5\mu\text{m}$ with a critical dimension tolerance of $\pm 0.09\mu\text{m}$. The final pattern resolution on the wafer will be $1/5$ of the feature size of the reticle, as the stepper uses a focused projection during the photolithography, so a $0.5\mu\text{m}$ feature size of photomask means the tiniest pattern on the wafer can reach $0.1\mu\text{m}$, which is larger than our smallest features. Once the LAAS DWL system was repaired and recovered its factory precision, we made a second reticle in house.

IV.2 Fabrication process of designed system

Based on previous works in our research group on the fabrication processes of comparable micro-ring resonators, we anticipated that fabricating these devices is challenging. We started by analyzing available in-house manufacturing processes that have been used in these previous studies: the first option is based on nano-imprint technology, a technique that has been adopted during the PhD of Miguel Diez-Garcia [94], for the manufacturing of SU-8 microring resonators and grating couplers. Although challenging, this technique was adapted in that case as the evanescent coupling between waveguides and rings was achieved in a lateral coupling scheme, where both elements are in the same plane. In a vertical coupling scheme, where the waveguides and the rings are on different planes, it would involve a two-step process that would require sub-micron precision in alignment, something that is not practically feasible with our Nanonex NX-2500 nano-imprint equipment. Nano-imprint also suffered for other drawbacks like residual layers, and a high cost for the master mold manufacturing that was made with e-beam lithography.

Based on previous results during the PhD of Farida Meziane [41] using the Canon FPA 3000i4, we concluded that stepper projection lithography theoretically offers sufficiently high resolution for our structures, and more suited to our vertical coupling scheme than nano-imprint, and as such will be preferred to the first option.

IV.2.1 Preparation of substrate coated by CYTOP

The fabrication process starts with a 4-inch Si wafer that will support a 800 nm thick CYTOP layer that will act as the lower cladding of the waveguide. The CYTOP used in our process is the CTL-809M, which is supplied by the AGC company in Japan. The CTL-809M has $-\text{CONH}-\text{Si}(\text{OR})_n$ terminal functional groups that allows good adhesion over Si or glass substrates without specific surface treatments. It contains 9% of monomer in mass and is well suited for thicknesses in the range of $1\mu\text{m}$ or lower. For thinner layer, it can be dissolved in CT-SOLV180. Our targeted 800 nm thick lower cladding is achievable without dilution of the CYTOP by adjusting the spin-coating

parameters, as well as the curing conditions which plays a major role in the final CYTOP thickness. The coupling efficiency of the grating coupler can be affected by the bottom cladding thickness as illustrated **Figure 62**, with a dependency showing an alternance of minimum and maximum according to the stationary wave formed at the CYTOP-Si interface. A 50 nm tolerance on the final layer thickness will ensure a positive influence on the coupling efficiency.

Before the deposition of the first layer, a standard piranha ($\text{H}_2\text{O}_2+\text{H}_2\text{SO}_4$ 1:3, 3mins) or oxygen plasma (800W for 5 mins using a TEPLA 300 semi-auto) is applied to remove organic and metallic contaminants present on the surface of silicon wafer. Before spin-coating, a 120° bake for 5mins is applied to dehydrate the wafer. This step will increase the adherence of the CYTOP coated onto the Si surface.

The spin-coating deposition of CYTOP is then carried out with a Suss Microtec LabSpin 6 BM spin-coater. The rotation speed (rpm) and acceleration speed (rpm/s) as well as spreading time (s) all plays a role on the coating thickness and uniformity: these parameters need to be adjusted according to the viscosity of the solution to obtain the required thickness.

After a couple of experiments, we obtained good results with a rotation speed of 2800 rpm for 30s. Compared to other polymer commonly used in our cleanroom, the CYTOP final thickness is highly dependent on the curing conditions. These conditions need to be optimized according to the thickness of the deposit. Because the solvent is completely volatilized to improve adhesion with the substrate, it is recommended to perform final baking at as high a temperature as possible. This also ensure a good stability of the CYTOP lower cladding during the remaining technological steps. However, if high-temperature baking is performed with solvent remaining, the coating surface may be rough (orange peel), or uneven film thickness may occur. To avoid this, a ramp heating program shown in **Figure 69** is applied to ensure the solvent dries slowly. We use a programmable oven (Binder Oven) to prevent the influence of surface gas flow. As the curing program is relatively long (about 4 hours), using a programmable oven over a hotplate allows us to prepare several wafers simultaneously.

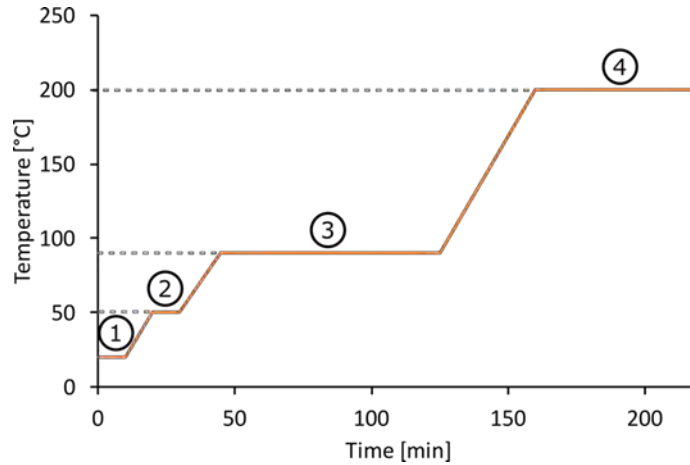


Figure 69. Gradually baking process of CYTOP polymer.

After drying at room temperature for 10mins (step 1), to stabilize the distribution of solvent, a pre-baking process at 50°C (step 2) is taken place to remove gas in the solvent. In a high viscosity solvent, bubbles need an extended time to be totally removed especially for coating thicknesses above 5µm. In our case, as our thickness is below 1µm, a period of 10mins is sufficient. Then another prebaking process at 90°C is applied for 80mins (step 3) to remove remaining solvent. The drying occurs from the resin surface, so if this step is too short, a certain amount of solvent will remain in the resin leading to non-uniformity of the surface. Then a final baking at 200°C for 60 mins (step 4) is launched. This step is necessary to improve adhesion between resin and base material. After this final step, the samples are cooled down back to room temperature with a progressive ramp. CYTOP surface uniformity is highly dependent on these curing parameters, and it should be emphasized that the duration of each curing plateau has to be optimized depending on the targeted thickness.

After the deposit of CYTOP cladding layer, the thickness of coating is measured using a KLA Tencor mechanical profilometer that offers a resolution as low as 10 nm, by applying a stylus pressure from 1 to 15mg. The principle of the measurement is relatively simple: the sample was scratched using tweezers so that the polymer layer will be peeled by the tweezers in certain area without hurting the Si substrate, while the width of the trace is big enough to be detected by the stylus profilometer. Then, by moving in two degrees of freedom on the surface of sample, the geometric structure of surface can be recorded by the probe. For each sample, at least three measurements are taken to verify the uniformity of the deposit over the entire substrate.

Using these parameters, we obtain a final CYTOP layer thickness of $820 \pm 20 \text{ nm}$, which matches perfectly with the design.

IV.2.2 Fabrication of Aluminum grating coupler on CYTOP lower

cladding

Under normal circumstances, the CYTOP surface at room temperature is hydrophobic, with a contact angle of deionized water of about 108°. Therefore, the stacked layer is difficult to be hold during the subsequent spin-coating process. To resolve this, a special treatment is implemented, which consist in evaporation of a thin aluminum layer onto the CYTOP surface followed by wet etching: this allows to decrease the contact angle of CYTOP down to 30° or less.

To take advantage of this metallisation step, the first fabrication process is designed to fabricate aluminium grating coupler directly by using this layer. On this basis, several different manufacturing processes have been proposed and improved step by step. We will analyse their advantages and inconveniences separately and introduce relevant optimization ideas according to practical experience.

This first approach is presented **Figure 70**. The Al metallization process was realized with an Alcatel EVA 600 evaporation equipment. It carries out vacuum evaporation deposit by electron gun. The material to be deposited is vaporized by the electron gun, and further deposited on the substrate. The substrate holder rotates 360° at a speed of 13 rpm, to ensure uniform deposition. A built-in thickness measurement based on a Quartz Crystal Microbalance (QCM) allows to precisely monitor the deposit thickness. This step will form a directional polymer binding with the CYTOP structure,

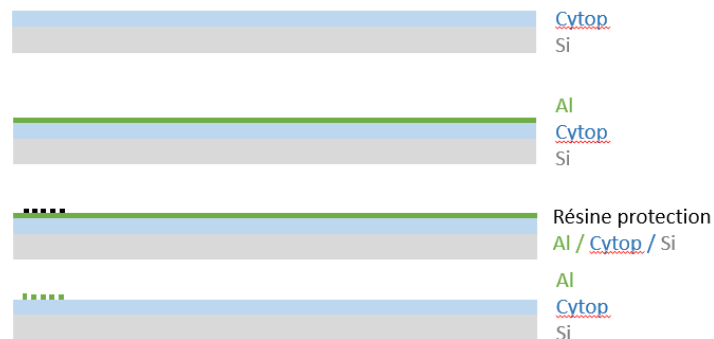


Figure 70. First approach adopted for manufacturing the aluminum grating couplers.

to increase the surface hydrophilicity. The sample is preferably stored at least 12h before proceeding to the next step, in order to stabilize this layer. To ensure a uniform evaporation of Al layer, we keep the thickness of this layer to be above 40 nm, for a more even coverage.

According to our experiments, the longer the time between evaporation and removal of aluminium layer, the longer the persistence of CYTOP surface hydrophilily exists. So, it is suggested to keep

this metallization layer as long as possible until the next step, to keep the surface hydrophilic as much as possible.

An AZ ECI 3000 photoresist is used to form the protection layer and pattern the grating couplers. This product is a modern, state-of-the-art positive resist series with high resolution and broad process window. Its high resolution as well as the process stability allow feature sizes close to the theoretical minimum attainable limitation [95]. With the positive photoresist, all parts of the resist will be removed after photolithography, except for the grating coupler lines, which will prevent the following etching of the aluminium layer. So, after etching, only the Al grating coupler should be left on the CYTOP surface.

To realise a standardized process, the spin-coating and development steps are operated using EVG 120, an automated resist processing system. This automatic system can operate coating, baking and development of photoresist on several sizes of wafers and in batch. Combined with a pre-aligner system, it can ensure a high repeatability.

The parameters used in our case are shown in **Table 8**, with some flexibility in the exposure parameters to adapt to any small fluctuations of the CYTOP thickness.

Table 8. Fabrication process of ECI protection pattern

Spin-coating	EVG120
Soft bake	90°C 90s
Photolithography Stepper	by Dose:2500 Focus:-0.5
PEB (post exposure bake)	110°C 90s
Development	EVG120
Rinse	EVG120

Then a chemical etching process by a mixture of H₂O 35ml+H₃PO₄ 200ml+HNO₃ 25ml is used to etch the unprotected Al layer. As the spacing between each grating coupler lines is very small (half a period, i.e., 400 nm), the solution encounters resistance to enter into the small gap, therefore it is necessary to pre-wet the wafer surface with deionized water to promote etching. After Al etching, the ECI layer is removed with acetone.

During this process, several unexpected inconveniences appeared, with strong influence on the final grating couplers. First, the grating couplers lines are “wavy” after the photolithography, as shown in **Figure 71-a**.

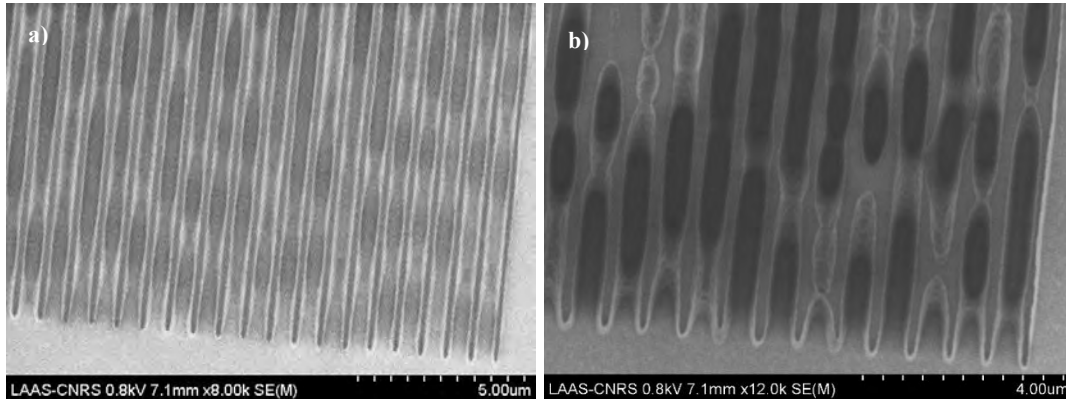


Figure 71. a) Wave shaped ECI stripes after photolithography. b) Uneven pattern of grating coupler after photolithography.

That phenomenon was attributed to light reflection at the ECI-metal interface. Secondly, with the same exposure parameters (dose and focus), the grating coupler lines are not uniform even in the same exposed area, as shown in **Figure 71-b**. Both of these defects have negative impact for the critical Al etching step.

In addition, we found additional issues that we attributed to the soft bake and post exposure bake steps, respectively before and after the exposure need, that are performed at 90°C and 110°C. As CYTOP and Al have different expansion and contraction thermal coefficients, that heating process tends to create some sort of bubble chambers at their interface as shown **Figure 72**. This problem could not be solved by increasing the curing time after CYTOP coating, which seems to indicate that it is not caused by the evaporation of residual solvent present in the CYTOP. This phenomenon was not observed in our previous works, as the Al layer was directly removed using wet etching without any thermal process involved.

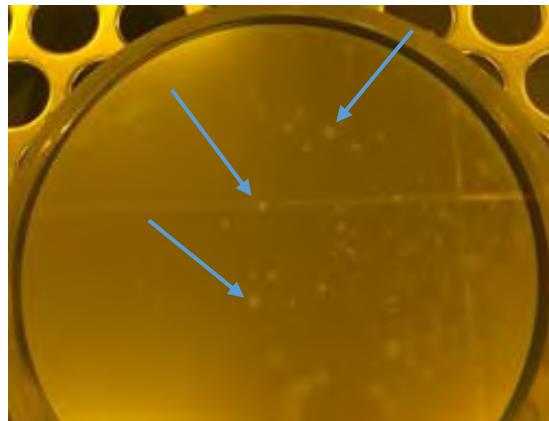


Figure 72. Bubbles that appear at the Al-CYTOP interface due to heating.

After immersing the wafer into the chemical wet etching solution for about one minute, the unprotected Al areas begins to be removed. The etching time is not easy to judge by eyesight, it is thus recommended to cumulate several short-time followed by visual inspection under a microscope instead of single-step etching, in order to account for the influence of environmental factors such as operation temperature.

After immersing the wafer in the solution for about 3 minutes, the unprotected Al layer is totally removed. Then the wafer undergoes a rinsing step for 2 minutes in deionized water and is dried by centrifugation. This drying technique is preferred over spray drying under nitrogen flow because it is more reproducible and more homogeneous; furthermore, it is less prone to damaging small features like the grating couplers.

During wet etching, lateral etching occurs simultaneously as the vertical etching: this will thus reduce the final width of Al lines. This isotropic process is not friendly to the final shape, as it is always hard to keep straight edges for the grating coupler as shown **Figure 73**.

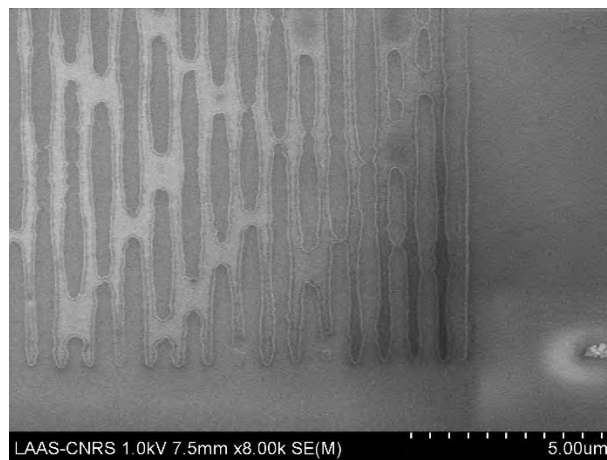


Figure 73. Irregular aluminum grating coupler lines after wet etching.

Based on these deceiving results, and after discussion with the TEAM cleanroom engineers, a plasma etching process was then evaluated to replace the wet etching step, trying to correct the irregular shapes of aluminum stripes. But as we need to avoid the heating temperature and time, to minimize the deformations at the Al-CYTOP interface and considering that the ECI resin does not adhere well to the Al surface, it was challenging to keep the grating coupler patterns consistent during plasma etching. The results **Figure 74** attests that this method left much to be desired. So after several unfruitful testing of various methods, we considered to change the process to lift-off, to break through the bottle neck. This approach is resumed in **Figure 75**.

In this method, the 800 nm CYTOP layer is deposited as the lower cladding, and the 40 nm Al layer at least 40nm is evaporated, to improve the hydrophilicity of CYTOP surface and create the grating couplers. As we said before, the longer the waiting time between evaporation and removal of

aluminium layer, the longer the persistence of CYTOP surface hydrophily will exist. The sample is supposed to be left at least 12h before next step, to stabilize this pattern.

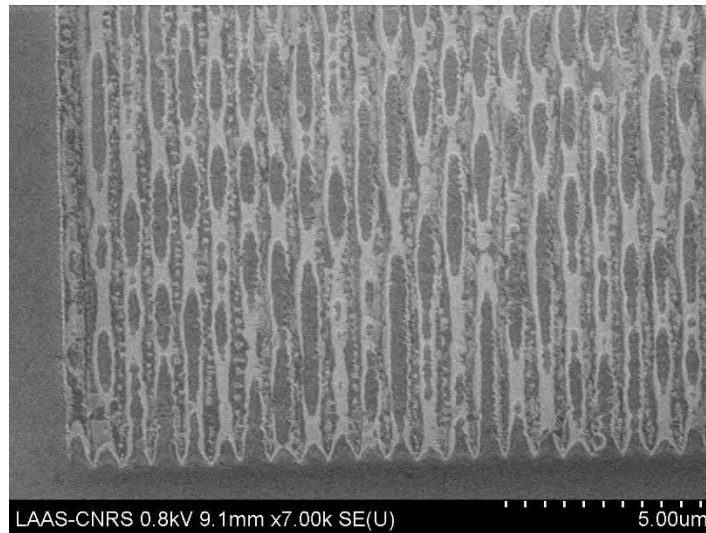


Figure 74. Aluminum grating coupler after Plasma etching.

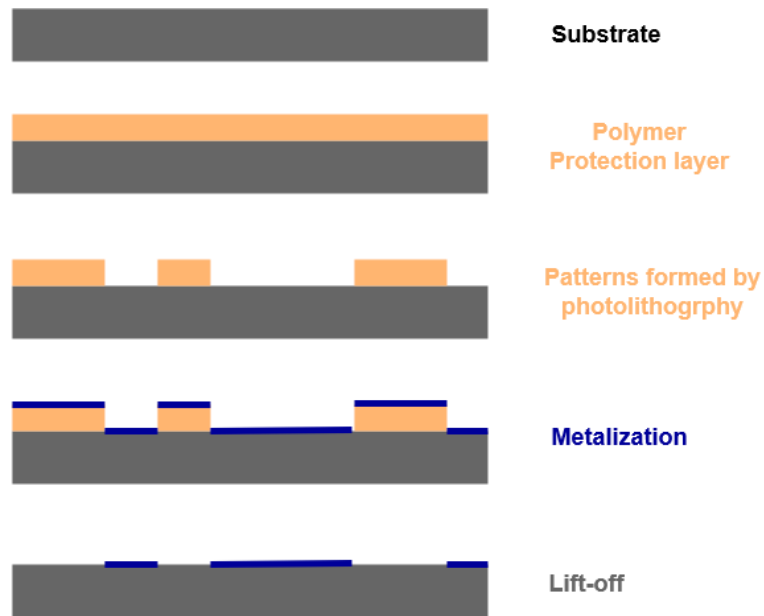


Figure 75. The manufacturing process flow of lift-off method.

Normally, the Al layer is chemically etched by the Al etchant (H_2O 35ml+ H_3PO_4 200ml+ HNO_3 25ml) just before the spin coating in the next step. Usually, a dehydration step heated to 120 degrees for 2 minutes after wet etching is applied before the coating of a photo resist, to improve the adhesion between the photo resist and the substrate surface. But in this case, the dehydration step should be avoided, because according to our experiments, a temperature higher than 100°C will

return the CYTOP surface back to hydrophobic. The same phenomenon was described by B. Agnarsson: i.e. the heating of the CYTOP layer after aluminium etching at more than 100°C had the effect of restoring the hydrophobic character of the CYTOP surface [47]. Instead, a spin drying is used here, to ensure a clean surface with high wettability, which is favorable to better deposits by spin-coating. Then, a dedicated, thermally stable lift-off photoresist is applied to form the desired structure.

This time, either the reticle or the photoresist polarity should be the opposite as previously used to obtain the complementary pattern. Simply put, the lift-off implies that the previously exposed part needs to be covered, and the previously covered part needs to be exposed. Then after the photolithography, all the CYTOP surfaces will be covered by the resist, except for the grating coupler lines. The 40 nm Al layer is then evaporated: ideally, the deposition should be done with a directional method, so due to the undercut property of lift-off resist, the metal will form a thin layer separately in areas with and without resist. So, when the resist layer is removed, only the Aluminum deposited onto the exposed parts will be left, to form the desired grating coupler.

Firstly, we chose the AZ nLOF 2000 series negative photoresist [96] to accomplish this process. This is a very mature lift-off dedicated photoresist, with remaining adjustable undercuts after development, high thermal and chemical stability. According to official technical datasheet **Figure 76** [97], the thinnest coating achievable by a standard nLOF resist is about 1.8µm, and the recommended resolution of pattern is in the range of micrometer.

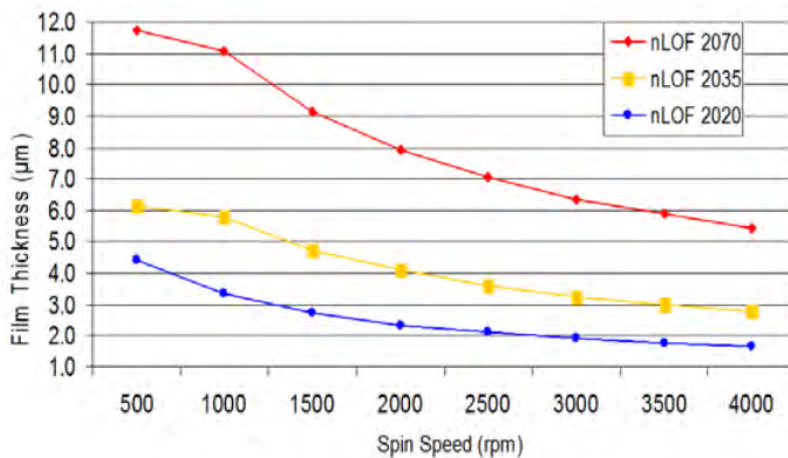


Figure 76. Coating thickness of nLOF 2000 series photoresists versus spin speed. [97]

As our critical features are around 400 nm, we concluded after a few tests that the nLOF 2020 could not reach our target. To improve this resolution limit, the nLOF was then diluted to decrease the coating thickness. By diluting the nLOF2020 and AZ EBR solvent with 1:1 ratio, the coating thickness could be decreased from 1.8µm to 200nm. However, while the resolution was greatly improved (**Figure 77-a**), the undercut could not easily be reached. As the thickness of Al layer is

60 nm, it's relatively close to the 200 nm height of the nLOF layer, and the evaporation of Al can only form a slice of film with protrusions, instead of separated stripes (**Figure 77-b**).

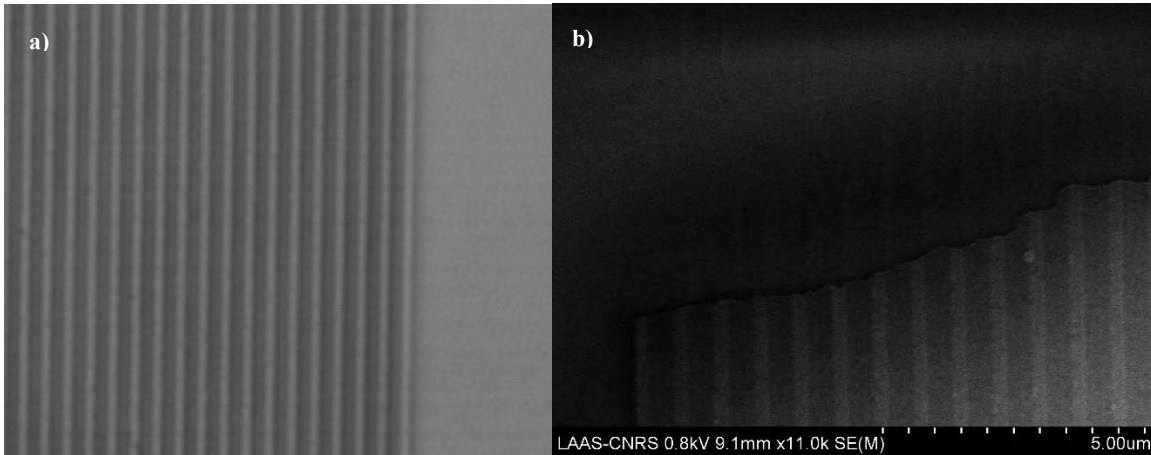


Figure 77. a) nLOF grating couplers after photolithography, without formed undercut. b) The evaporated Al forms a slice of film rather than separated stripes after etching.

We tried to adjust the soft bake and post expose bake temperatures to help establish the undercut, as shown in official technical datasheet, but we never succeeded in this way. So, we turn to AZ nLOF2035, to increase a little the layer thickness.

The nLOF 2035 diluted by AZ EBR solvent at 1:1 ratio will form a coating thickness of 1.2 μ m, a significantly higher thickness than in the previous experiments that was chosen to guarantee the undercut. With the recipe in **Table 9**, grating couplers with several duty cycles (obtained by adjusting the exposure dose) were fabricated.

Table 9. Fabrication process of Al grating couplers with nLOF dilution solution by lift-off method.

Pre-preparation	Si wafer + 800nm CYTOP cladding (after aluminizing and acid cleaning treatment)
Spin-coating	T=40s; V=4000rpm, Acc=500rpm/s
Soft bake	110°C 120s
Photolithography by Stepper	Dose:1200-1500 Focus:-0.5
PEB	110°C 60s
Development	MF-CD-26 90s
Rinse	DI water
Metalization	Evaporation 60nm Al
Lift-off	DMSO-D350 90°C 12h

The clean and tidy patterns obtained during our experiments were always in the case of a duty cycle above 0.7, as clearly shown in the SEM images **Figure 78**.

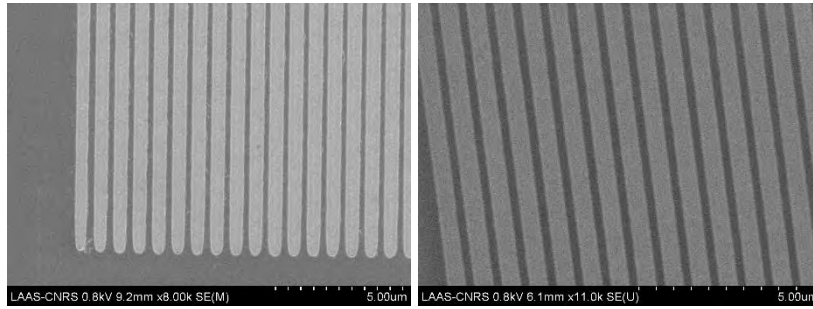


Figure 78. Aluminium grating couplers fabricated by lift-off process.

For the grating patterns with smaller duty cycle, the edges of aluminum wires are quite rough **Figure 79**. The residual aluminum wires that should have been removed, were dispersed around the grating coupler. Some of them are still connected to the main lines of the grating coupler, and are impossible to take off even by increasing the immersion cleaning time. These observations tend to indicate that proper undercuts seem to be found only under the over exposure conditions, conditions for which the duty cycle is outside our targeted values.

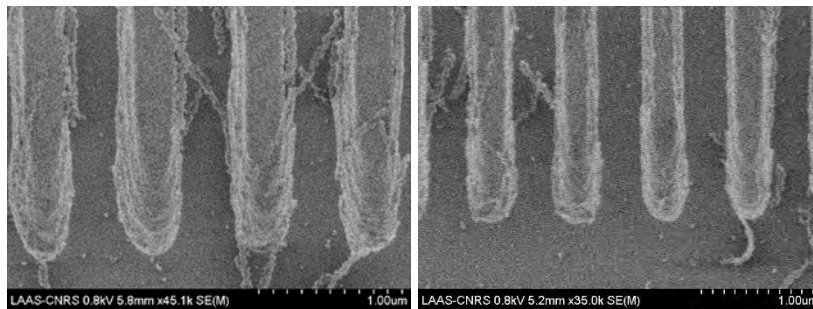


Figure 79. Aluminium grating couplers with residuals of aluminium lines.

After a discussion with the engineer group (TEAM) members in laboratory, our engineer Laurent Mazenq proposed an alternative solution: to establish the undercut structure with a two layer photoresist structure. In traditional method, lift-off dedicated photo resist will directly form undercut after development, so the following evaporated metal will be shaped based on the photolithography pattern. When the undercut is not established, the final pattern will be influenced, especially at the edges of the pattern like schematized in **Figure 80**. To remedy this, a double layer structure with a wide top and a narrow bottom is developed, to replace the fonction of undercut.

Here we combined LOR photo resist and ECI to build desired double layer structure. LOR lift-off resists are based on the PMGI (polydimethylglutarimide) polymer and are well suited for a variety of critical and non-critical level lift-off processes. Used in combination with conventional positive resists, LORs are available in a wide range of film thicknesses and undercut rates [98]. As LOR resist develops isotopically, its coating thickness should be thin enough, to reduce bilateral etching effect for the 400 nm wide pattern. Former ECI positive resist is chosen to form the upper layer, as

it offers high level resolution maturely. As we reverse the negative resist to positive resist, the reticle pattern polarity has to be reversed to adapt this change.

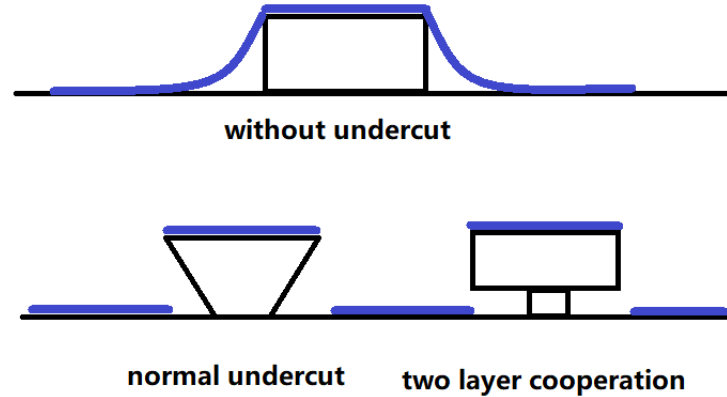


Figure 80. Normal undercut form and functional interchangeable two-layer form for lift-off process.

By using the recipe in **Table 10**, double layer combination was formed as expected.

Table 10. Fabrication process of grating coupler by double layer lift-off method.

Pre-preparation	Si wafer + 800nm CYTOP cladding (after hydrophilic treatment)
Spin-coating	LOR 3A T=30s; V=8000rpm, Acc=4000rpm/s
Soft bake	230°C 120s
Spin-coating	ECI T=30s; V=3600rpm, Acc=4000rpm/s
Soft bake	90°C 60s
Photolithography by Stepper	Dose: 700-1400 J/m ² Focus: -0.4
PEB	110°C 120s
Development	MF-CD-26 90s
Rinse	DI water
Metallization	Evaporation 60nm Al
Lift-off	PG remover 90°C 2h

In this process, we use a very high 8000 rpm spin-coating speed for the LOR layer in order to lower the final thickness, as this will reduce the bi-lateral etching on the tiny lower part during the development step. Then a soft bake temperature of 230°C instead of 200°C was applied, to strengthen the adhesion of LOR on the wafer surface.

The dose of exposure is varied from 700 to 1400 J/m², according to the exposure pattern represented **Figure 81**: this range covers the exposure conditions from underexposure to overexposure, as shown in the SEM images of **Figure 82**.

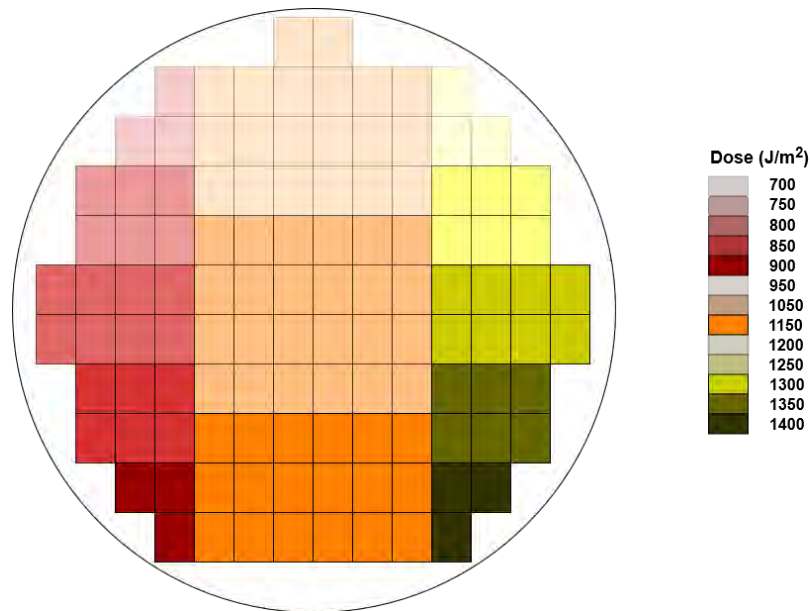


Figure 81. Distribution of different doses of exposure on the wafer during photolithography for the LOR+ECI lift-off process optimization.

In underexposed condition (**Figure 82–a**), the exposure dose isn't strong enough to penetrate through all the photoresists layers during exposure period; the consequence is that the bottom of the pattern is still connected, and the grating shape is only partially rendered. In overexposed condition (**Figure 82-b**), the obtained duty cycle is much smaller, and the tiny connection in the bottom cannot support the upper structure, which leads to a collapse of the grating coupler lines on the substrate after development.

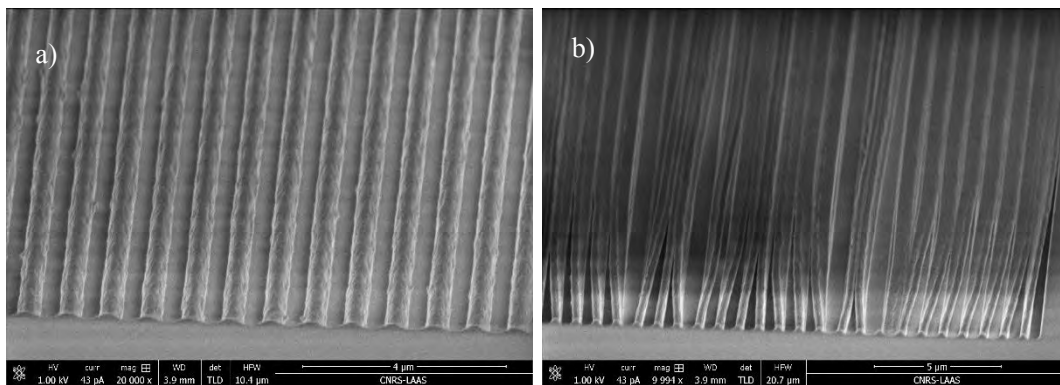


Figure 82. Underexposed (a) and overexposed (b) patterns of grating coupler after development.

In that case, the development step should be implemented manually and precariously, because the LOR bottom layer which is smaller than 300nm after development, is too fragile to sustain the vigorous development of the automated EVG 120. **Figure 83** shows how some lines of the grating

coupler pattern are broken during the development step due to the developer pressure applied by the equipment.

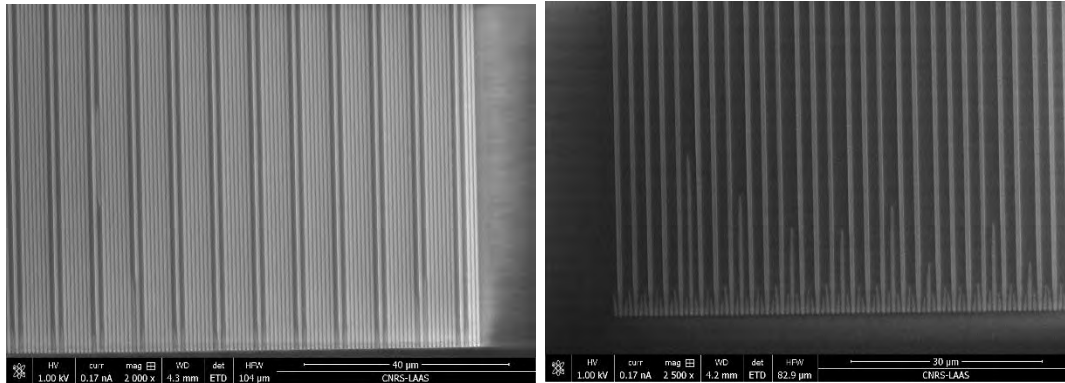


Figure 83. Damage to the pattern of grating coupler caused by the flushing pressure from the machine of development.

Attention should also be paid to avoid nitrogen flow for drying the wafer, or avoid applying it directly on the surface, as this will also destroy the fragile bi-layer structure. The drying step should be fulfilled by spin dryer with a speed under 3000rpm/s.

We found the best exposure parameters were between 1000 to 1100 J/m² to obtain the appropriate alternative undercut. As shown in the SEM photos in **Figure 84**, we managed to obtain the expected aluminium grating couplers.

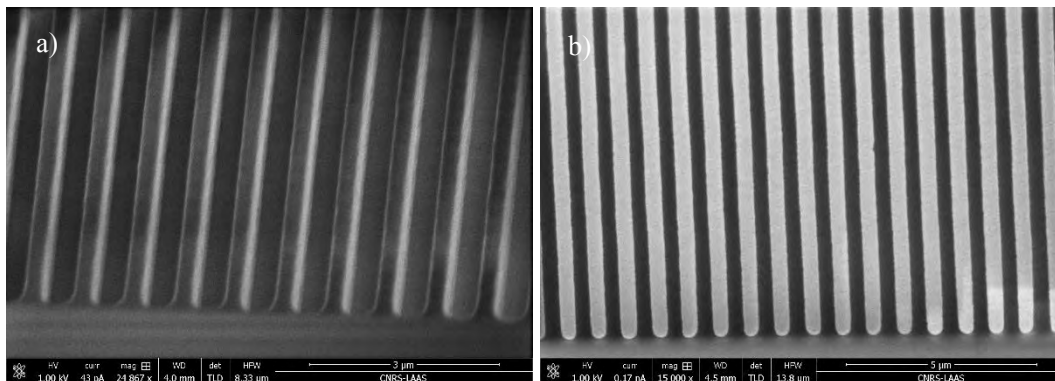


Figure 84. a) Grating coupler patterns in LOR+ECI obtained after photolithography with exposure doses between 1000 to 1100 J/m². b) Aluminium grating coupler obtained after completion of the lift-off process.

Considering the manual control for the development step and the very small and fragile dimensions of the structure to be developed, the yield rate with this approach is not high. But due to the number of microresonators per wafer, this inconvenience is tolerable.

IV.2.3 Fabrication of SU-8 waveguide and taper

To realize the waveguide, we choose the SU-8 photoresist fabricated by Microchem company. Varieties of models are provided by this company to fulfill our target dimension. We can also have a precise control over the waveguide thickness by adjusting the spin-coating parameters from given Si substrate recipe with minor adaptations due to the nature of CYTOP.

After the obtention of the Al grating couplers, the following step in the process is the fabrication of the SU-8 waveguides, which comprises one or two tapers depending on the output configuration (in-plane/butt coupling, or out-of-plane) and a single-mode area with a 400 nm x 1 μ m cross-section. The fabrication process is given in **Table 11**.

Table 11. Fabrication process of SU-8 waveguide and taper

Spin-coating	1000rpm 200acc 30s 2000rpm 300acc 30s
Soft bake	105°C 1min
Photolithography by Stepper	Dose:2500J/m ² Focus:-0.5
PEB (post exposure bake)	105°C 1min
Development	Developer-SU-8 1min
Rinse	Isopropanol

As SU-8 is a negative resist, the exposed photosensitive elements will change chemically and form bonds with the substrate below (in our case CYTOP™), they then become insoluble in the developing solvent. This insolubility is due to an increase in molecular weight and the change in polarity of the functional groups of the resin.

According to the processing guidelines of Microchem for SU-8 2000.5, the recommended exposure energy for a 0.5 to 2 μ m thick SU-8 layer is comprised between 60 to 80mJ/cm², paired with a recommended temperature of 95°C for both the soft bake (SB) and the post-exposure bake (PEB).

The stepper focus setting was first set at a value of -0.25 μ m, to be located approximately in the middle of the SU-8 layer. The first tests with these parameters led to a lot of distortions, stress, and subsequent localized peeling of the SU-8 waveguides after development and PEB. These defects were especially visible in the smallest cross-sections of the waveguides (width = 1 μ m), as shown **Figure 85**.

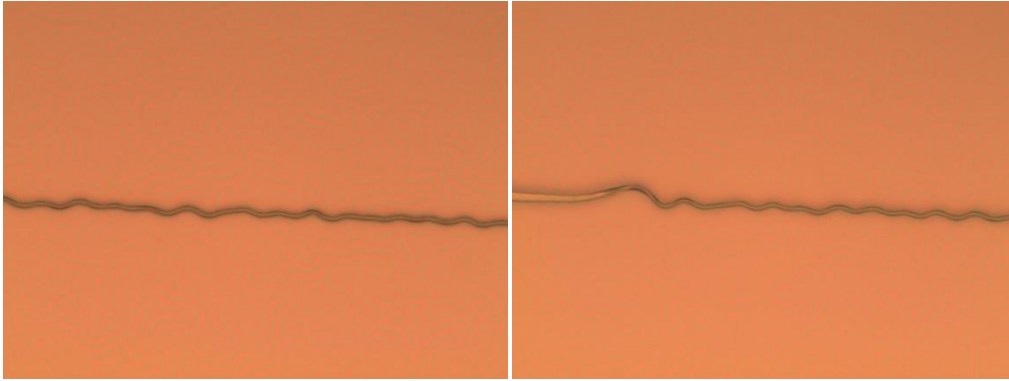


Figure 85. Distortions and misalignments of SU-8 waveguides on CYTOP lower cladding.

After a series of tests, we considered that this abnormal phenomenon was due to the weak adhesion of the SU-8 resin coated onto the CYTOP surface, as well as to small non-uniformities in the CYTOP surface that leads to local defaults in the focus setting of the stepper. To resolve this problem, we significantly raised the final dose exposure up to $250\text{mJ}/\text{cm}^2$, combined with an increased PEB temperature at 105°C , to stabilize the resin structure modified by the photoreaction and induced by the stepper. The focus plane of stepper was also altered and set at $-0.5\mu\text{m}$ from the reference plane (the SU-8 surface), which is no longer located to the center plane of waveguide, but at the interface between CYTOP lower cladding and the SU-8 waveguide, to further strengthen the adhesion of these two materials. These parameters were obtained based on a series of experiments conducted with varying conditions in terms of dose, focus, and SB/PEB temperatures.

An isopropanol rinse is performed after development, allowing to remove remaining developer, but also to ensure that the development is complete: in the case of an underdevelopment of the resin, whitish traces are likely to appear in the presence of this solvent.

After each fabrication process, the waveguide thickness measurements were carried out using a mechanical profilometer, to confirm the SU-8 waveguide dimension is in the targeted range of 400-500nm to ensure single-mode conditions.

The SEM pictures of accomplished SU-8 waveguide and transitional tapers are shown in **Figure 86**. It can be observed that the tapered section of the SU-8 waveguide covers the Al grating coupler uniformly. Compared to the 60nm Al thickness, the subsequent SU-8 layer is almost ten times thicker, which accounts for the observed planarization effect as observed on the close-up tilted view, where the edge of the taper section and the grating coupler Al lines can be observed.

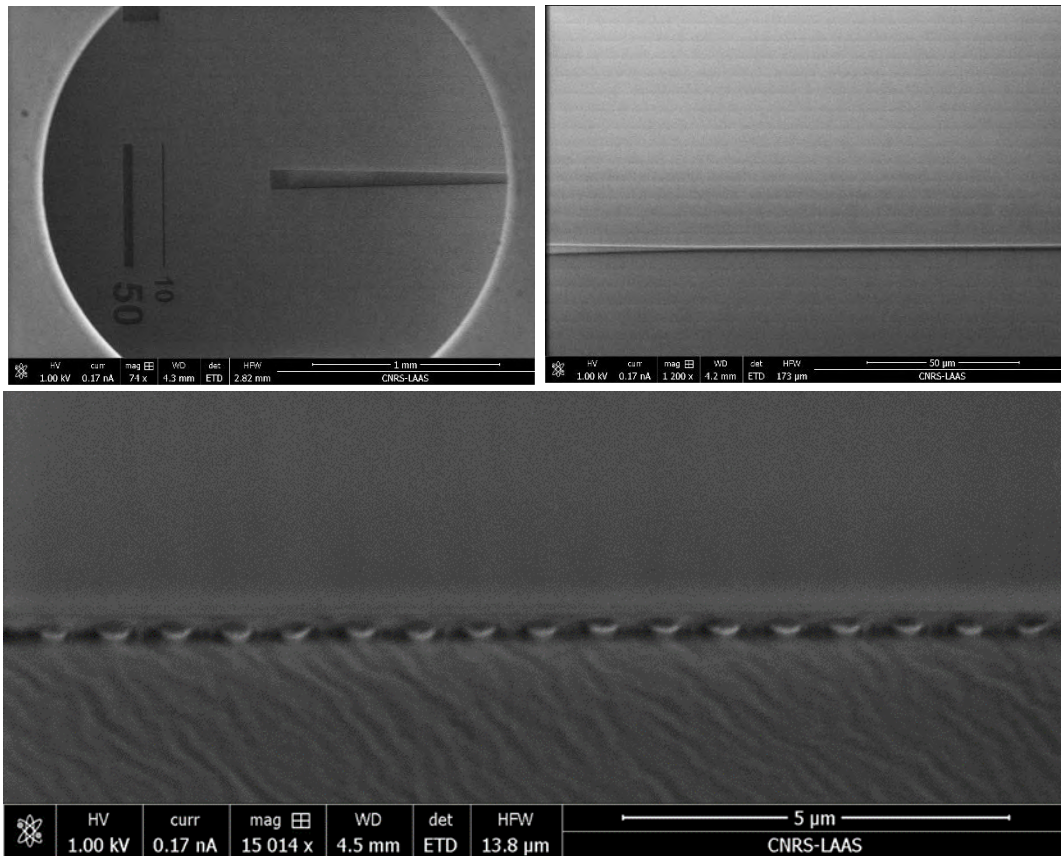


Figure 86. Upper left: SEM wide view of the tapered waveguide and the grating coupler realized over a CYTOP cladding. Upper right: Close-up view of the waveguide at its thinnest section (1 μm width). Bottom: Tilted SEM image at the edge of the taper, highlighting the smoothness of the surface despite the presence of the Al grating coupler.

This image also illustrates the textured surface of the CYTOP, which has been attenuated by the aforementioned curing conditions optimization but is still visible at the nanoscale. An observation of the waveguide at its smallest width shows that the adhesion over the CYTOP is satisfactory, with no visible defects or peeling of the waveguide.

For the in-plane (butt-coupling) output configuration, as we used an over exposure condition, the improvement on the waveguide end shape (shown **Figure 87**) is not as obvious as in the simulation obtained by GenIsys. We will compare in-plane output configuration with grating coupler output configuration in the following characterization section.

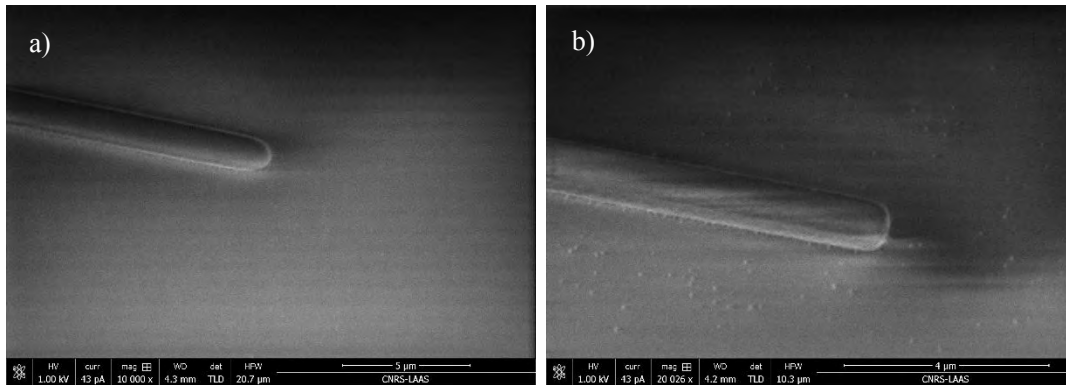


Figure 87. a) Waveguide exit port by regular photolithography. b) Waveguide exit port improved by GenISys design.

After this step, the sample is ready for the next fabrication steps which include the upper CYTOP cladding deposition and subsequent etching to define the gap, followed by the fabrication of the micro ring resonator.

IV.2.4 Fabrication of CYTOP gap between waveguide layer and the micro-ring layer

Before the construction of the micro-ring resonator, a thin layer of CYTOP needs to be added. The role of this CYTOP layer is multiple: (i) it determines the gap between the waveguide and the micro-ring, hence directly influence the coupling conditions. (ii) It acts as the upper cladding of the waveguide and offers a symmetry of refractive indices which is beneficial for the optical confinement. (iii) It covers the waveguides, leaving only the micro-ring to be exposed to the gas, and at the same time act as a protective layer. In order to fulfil the optimum coupling conditions, the targeted thickness of this layer is around 200nm or smaller. While such a thickness could be directly obtained by spin-coating with appropriate dilution of the CTL-809M in the dedicated CT-SOLV180 solvent, due to the topology induced by the 500nm thick SU-8 waveguides, this would result in planarity defects in the coupling area with deformation of the ring. In order to obtain a planarization effect, a better strategy is to spin-coat a thicker layer of CYTOP and proceed to an etching of this layer until the targeted thickness is reached, as described and successfully applied in the thesis of C. Delezoide [27].

The same recipe as for the bottom cladding was used in order to obtain a 800 nm thick layer. As CYTOP can be etched with an oxygen plasma, we performed an etching speed experiment with a DIENER Plasma O₂ equipment. There are two oxygen generators to control the etching speed: one

to control the ionization voltage to influence the bombardment speed, and the other to control the ion concentration.

By applying power settings of 40W/10W (ionization/bombardment respectively), with an oxygen flow of 50sccm and the pressure of 10mT, approximately 470-500 nm of the CYTOP thickness was etched in one minute. By using this average etching speed of 485 nm/min with the aforementioned power settings, the coupling gap between waveguide and resonator can be precisely tuned to obtain the optimal coupling factor.

An observation of the CYTOP surface before and after ionic etching was obtained by AFM (Atomic Force Microscopy). AFM is a type of scanning probe microscopy with a high resolution on the order of fractions of a nanometer. It can gather the information of surface by force measurement or frequency measurement with a mechanical tip connected to a cantilever (**Figure 88**). The probe is very close to the sample surface so that it can sense the force between atoms, the reaction of the probe to the force being recorded to form an image of the topography of the sample surface.

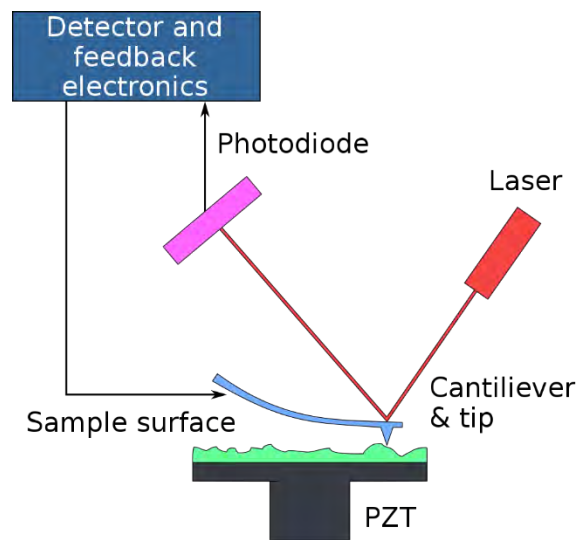


Figure 88. Typical configuration of an AFM.

In tapping mode, the cantilever oscillates on an intrinsic frequency; the surface fluctuation of the sample will influence this oscillation frequency and finally form an image of the three-dimensional shape. This mode is very soft and is favoured in order to protect the sample surface from damage.

By using tapping mode, the roughness and the topography of the surface were quantified and are presented in **Figure 89**. The plasma etching has slightly increased the surface roughness, but the surface level undulation was decreased from 81 nm to 6 nm. We see that the intrinsic surface of CYTOP coating has small folds, which make them look like the “orange peel”, despite all our efforts to optimize the curing conditions.

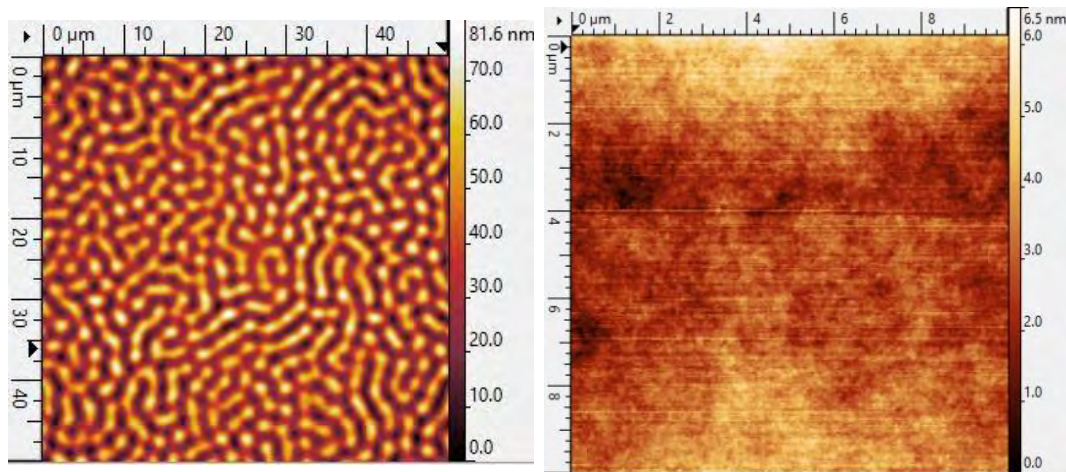


Figure 89. CYTOP surface before/after plasma oxygen etching.

IV.2.5 Optical characterization for preliminary achievement

We now have a partially complete structure for our system. Before the addition of the micro-ring, we can already start testing the coupling efficiency for the grating couplers paired with the SU-8 waveguides, to ensure that enough light can be coupled in the waveguide in order for the system to work as expected.

We designed two kinds of waveguides: the first type of waveguide has grating couplers at both ends, the light of source entered by the first grating coupler into waveguide, then exit by the second grating coupler, this course goes through two couplers and lose energy twice. We choose to start in more relaxed conditions by characterizing the second structure, with an out-of-plane input grating coupler, and a classic waveguide in-plane output (i.e. butt-coupling). In this case, the detector should be very close to the exit port to collect the maximum of emitted light., which means that wafer cleaving should be done as close as possible to the exit port.

In order to inject or collect light through the facets of a waveguide in satisfying conditions, it is critical to obtain good optical quality surfaces. While this can be achieved on inorganic materials by careful wafer cleaving, this is much harder to obtain with polymer waveguides. As the machine cutting will produce a lot of droplets, which will pollute all surface of the chips, a simple manual

cutting trick called two-points pressure takes place here. It is suitable for a lot of experimental conditions on silicon wafers.

The Si wafer used in the laboratory has a (1,0,0) lattice structure, so we can use this feature to make it break naturally and precisely. First, we put the wafer on a paper which has vertical and horizontal grids. We align the edge of wafer with one grid and align the edge we want to cut with another grid. Then we press with tweezers on one point of intersection where the edge of the wafer to be cut crosses the grid, and press with a diamond cutter on the other point of intersection where the edge of the wafer to be cut crosses the grid. Accompanied by a crisp clicking sound, the parts are neatly separated (**Figure 90**). While requiring a bit of practice, this method proved to be very efficient and simple, without damaging any patterns on the surface of the wafer.

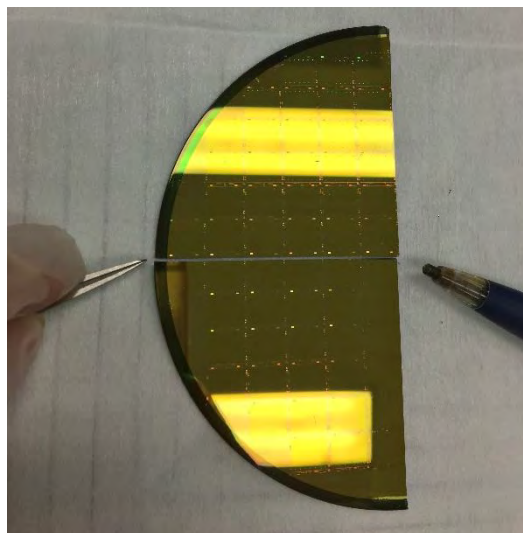


Figure 90. Two-point pressing method for wafer cutting without damaging the patterns.

After several experiments, even though the in-plane waveguide output structure should present less energy loss compared to the grating coupler, the output light diverges too fast, and it is diffused poly directionally by fragments at the junction, these factors make it hard to collect enough light signal at the port, so we decided to adopt grating couplers on both ends for the primary tests. The first iteration of the optical bench is illustrated in **Figure 91**.

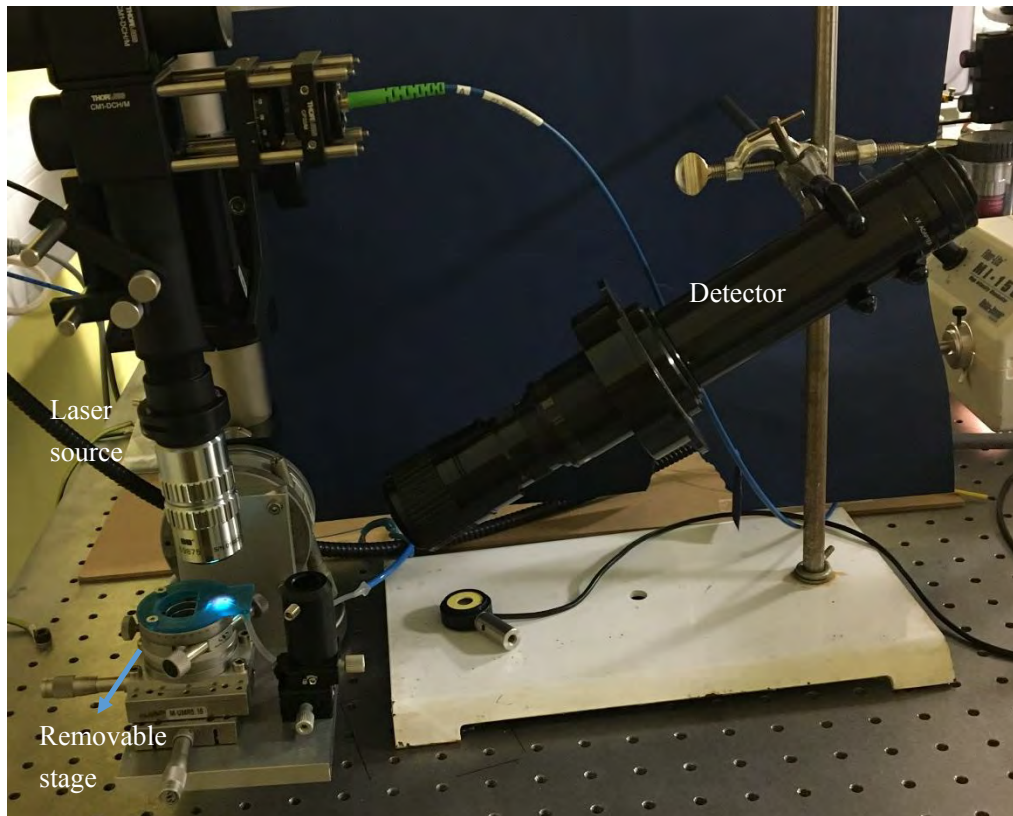


Figure 91. Optical bench for the characterization of the grating couplers.

The laser source enters perpendicularly from above the sample. For the first test, we use a high-power tunable fibered bulk laser (Broadsweeper BS-840-2 Superlum) to ensure a significant output signal. By using a program in the computer, we can control the current applied on the laser to vary its output power and scan the wavelength with a $\sim 70\text{nm}$ span around the 850nm center wavelength. The sample is fixed on a removable stage while adjusting the position, the stage can also rotate a few tens of degrees in XY plane, to adjust the incident angle of laser.

A detector is placed on the other side to collect the output signal, a near-infrared camera besides the detector will record the reticule plane to ensure the output light comes definitely from the output grating coupler, rather than other reflection signals.

Our first test begins with a semi-manufactured sample which consists of CYTOP lower cladding, Al grating coupler, SU-8 taper, SU-8 waveguide, and the upper CYTOP cladding. As the wafer had to be cut into small pieces to adapt to the optical bench, this step also increases the loss of samples. The incident light and output light recorded by the near-infrared camera are shown in **Figure 92**. According to the calculation of simulation in paragraph III.2, the optimal coupling efficiency of the polymer system with Al grating couplers can be 12% maximal, which means only 1.4% of initial power will be transmitted to the exit port. Considering the fabrication errors, surface defects, and other irregular edges that exists in real situation, the final output signal is very weak compared with

the input signal. But we can see that this structure can couple light into the system and then emit it as designed.



Figure 92. Incident light on the input grating (left) and output light obtained on the output grating (right) with an SU-8 waveguide covered on CYTOP lower cladding.

By scanning the incident wavelength from 805 to 875nm, and varying the incident angle from 10° to 30°, we confirmed that the input signal at 850nm with incident angle at 19° produce the best performance, which is corresponding to the simulation.

With this result, we were suddenly stopped by the global pandemic of COVID-19 that forced the laboratory to close for several months. Subsequently, the number of people who were allowed to enter in the laboratory was strictly limited, and the equipment booking schedules were also very restrictive, and not compatible with the long fabrication and characterization process.

According to previous works, the fabrication process of grating couplers and waveguides on a CYTOP lower cladding have raised several issues, especially being very time consuming and offering poor reproducibility, so we considered to continue the remaining part of the experiment with an easier to process cladding, to speed up the development process.

After analyzing the problems of CYTOP surface, the SiO₂ lower cladding seems to be a suitable substitute in the limited remaining time, as it has uniform thickness and will not be deformed during baking process. In addition, the combination of SU-8 with SiO₂ has also been successfully demonstrated in the literature.

So, in order to speed up the work progression and to adapt to the reduced time, further manufacturing was initiated with SiO₂ as the lower cladding, which has a shorter and more convenient manufacturing cycle.

IV.2.6 Grating coupler on SiO₂ lower cladding

As the COVID-19 largely reduced the time originally planned to do more experiments, we decided to use samples that are easier and quicker to prepare for the next step of the experiment. In order to

accelerate the research of subsequent manufacturing processes, we simulated the same dimension of grating couplers (so that we don't need to fabricate a new reticle) based on a SiO₂ lower cladding, as this cladding is easier to fabricated than CYTOP layer and can reduce the manufacturing cycle of each wafer.

A rapid simulation with Lumerical (FDTD) was performed to ensure that a good coupling efficiency could be maintained without changing the reticle and grating coupler dimensions with a SiO₂ lower cladding in place of the CYTOP lower cladding previously used. In this simulation, we kept the same values for the incident angle value (19°) and the grating coupler period (800 nm). We then varied the values of duty cycle (0.2-0.8), Al grating coupler thickness (20-100 nm), and incident position to find the optimal combination of parameters. While the incident position is not important here as it can be adjusted on the optical bench, it is varied here just for the sake of finding the highest coupling efficiency.

A SiO₂/Al/SU-8 grating coupler structure with similar dimension as before, can obtain a theoretical coupling efficiency as high as 29%, in that case with a duty cycle equals to 0.53, and an Al layer thickness of 67 nm. The obtained coupling efficiency is two times bigger compared to the CYTOP/Al/SU-8 structure. Based on this result, we decided to use this new lower cladding to pursue the fabrication process and to decrease the overall processing time.

The thickness of SiO₂ lower cladding is set to be thick enough (> 2 μm), to avoid the formation of standing waves between Si-SiO₂ interface and SiO₂-air interface, to remove its influence on the coupling efficiency of grating coupler above.

In addition, as the lower cladding material is changed from CYTOP (n=1.34@850nm) to SiO₂ (n=1.45@850nm), the decrease of the refractive index contrast between the lower cladding and the SU-8 (n=1.57@850nm) waveguide results in an attenuation of transmission energy [99]. This attenuation can be counterbalanced with an increase of the waveguide cross-section: as the waveguide width is fixed by the reticle patterns, this is more conveniently achieved by an increase of the waveguide thickness that can be adjusted by modifying the spin-coating parameters. Running the same Matlab program as in our preliminary study and taking with an adjustment of the relevant parameters, an optimum SU-8 thickness of 800 nm was determined, keeping a waveguide width of 1 to 2 μm. This thickness increase can be obtained with the same SU-8 2000.5 photoresist by a decrease of the spin-coating speed.

The fabrication process was then pursued with the following steps: a standard piranha (H₂O₂+H₂SO₄ 1:3, 3mins) or Plasma O₂ (800W for 5mins by TEPLA 300 semi-auto) process is applied to remove organic and metallic contaminants present on the surface of silicon wafer. Afterwards, a PECVD (Plasma-Enhanced Chemical Vapor Deposition) process is used to obtain a 2.5μm thick SiO₂ layer on the Si substrate. Once the reacting gas (SiH₄) is injected into the reactor, an RF electric voltage is applied between two planar electrodes, to generate a plasma that will

generate chemical reactions in the reaction chamber to deposit thin films from gas state (vapor) to a solid state onto the substrate. Here we used a multiplex ApSy-PECVD100 equipment. The roughness of the layer is 3 to 5 nm for our targeted thickness, with a thickness uniformity of 40 nm on a 4-inch wafer entire wafer: this is better than what was observed on the CYTOP layers and should provide better consistency of the stepper exposure as the focus setting will be identical over the whole wafer. A 60 nm aluminum layer is subsequently added by EVA 600 metallization machine using the same recipe as before.

Compared to the previous process, an anti-reflection coating named BARC (Bottom layer Anti-Reflective Coating, MicroChemicals Company) is added to the process before the deposition of the high-resolution ECI photoresist. BARC coating is typically used to improve the fidelity of the patterns especially when the critical dimensions approach the resolution limits of the photolithography equipment. In our case, the 400 nm wide lines that composed the grating coupler are approaching the 350 nm resolution limit of the i-line Canon FPA 3000i4. While this BARC layer was envisaged in the first process with the CYTOP lower cladding, the high curing conditions required (200°C) were not compatible with the CYTOP+Al stack as this would result in the formation of bubbles as observed in **Figure 72**. This phenomenon was not observed at SiO₂-Al interface during the BARC curing process, proving that this stack was more robust and stable toward thermal treatments.

BARC prevent unwanted light reflections at the Al surface that travels back into the ECI coating during exposure as illustrated **Figure 93**: the reflected light usually interferes on the formation of high-precision patterns, while the transferred patterns obtained with the assistance of BARC exhibits a higher degree of fidelity and a high yield rate. For a given set of exposure dose and focus, the photolithography was found to be much more repeatable and consistent, especially for our multi-layer structure. The thickness of the BARC layer should be adjusted according to the wavelength of incident light and the refractive index of photoresist [100]. In our condition, an i-line (365 nm) exposure is used on ECI photoresist, and the recommended BARC thickness should be 200 nm.

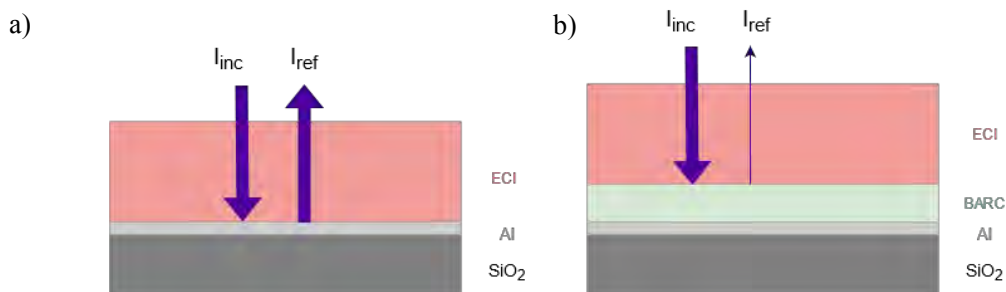


Figure 93. The incident light reflected on the substrate has nearly the same intensity as before, it will interfere the final resolution of the photoresist pattern (a), while using an anti-reflective coating (BARC) on the substrate will markedly minimised this effect, to keep the final pattern as neat as possible.

After exposure and development of the ECI to form the grating coupler structure, a Reactive Ion Etching (RIE) is used to remove the unprotected Al layer. Compared with chemical wet etching, this method is independent of crystallinity and leads to a better control of etching profile, the critical dimensions are easier to get without under etching. This process combines physical and chemical etching at the same time in a vacuum environment. As shown in **Figure 94**, a highly reactive plasma composed of particles as electrons, ions, radicals, photons ... is created by interaction between gas flow and electrical field. On one hand, the ions separated from gas molecules by electrons are accelerated towards the material and bomb on the substrate (physical etching), on the other hand the radicals chemically react with the substrate (chemical etching).

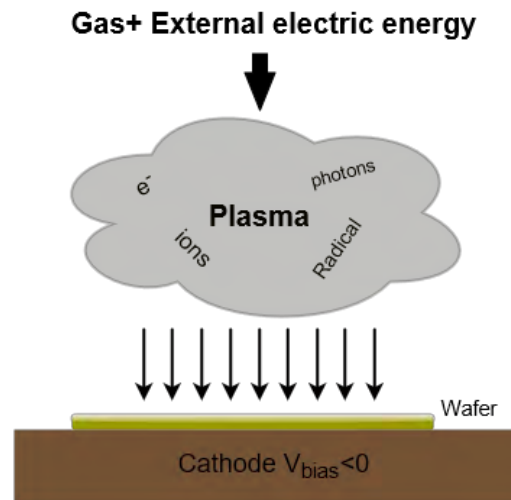


Figure 94. Schema of plasma etching.

During this reactive ion etching (RIE), the physical etching is anisotropic and no selective, while the chemical etching is isotropic, selective, and sometimes forms volatile products on the surface of sample. This process is carried out by Omega 201 equipment from Trikon. It is an ICP-RIE (Inductively Coupled Plasma) type plasma etching reactor and is suited for 6-inch wafers and smaller. It is equipped with an end point detection of etching achieved by laser interferometry @670 nm with a beam spot size of 100 μm that gives a feedback of the refractive index of the layers. The substrate holder can be heated up to 45°C, and the samples can be fixed on the holder by thermal conductive adhesive or electrostatic clamping. By using a thermal conductive adhesive, the temperature of Si substrate after plasma can be drastically decreased from 138°C down to 37°C, a configuration which is recommended to avoid any unwanted effects due to temperature. It has been observed that samples fixed with thermal conductive adhesive would exhibit a smoother surface after etching as illustrated **Figure 95**. The typical range of etching depth is from 20nm to 15 μm , which is compatible with our process.

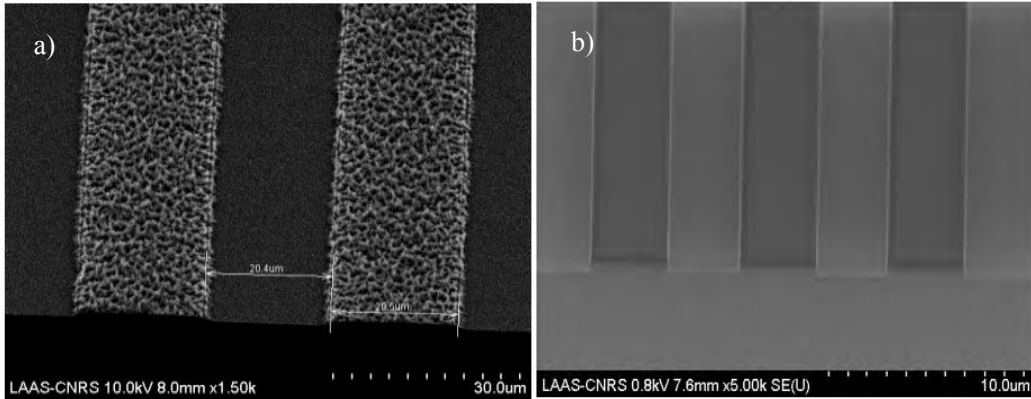


Figure 95. ECI patterns after plasma etching, a) with electrostatic clamping to the substrate holder, and b) with thermal conductive adhesive on the substrate holder. The roughness after etching is much lower in b).

Two powers (V_{icp} and V_{bias}) are used to control the speed of ionic bombardment and plasma density, the combination of which will influence the etching speed and etching pattern profile. Between them, V_{icp} has a significant effect on etch rate and selectivity, because it favors the quantity of reactive species in the plasma (chemical etching) while V_{bias} favors ion bombardment (non-selective physical etching).

The fabrication process of the Al grating coupler over the SiO_2 lower cladding is presented in the **Figure 96**, while the relevant parameters for each step are resumed in **Table 12** and **Table 13**.

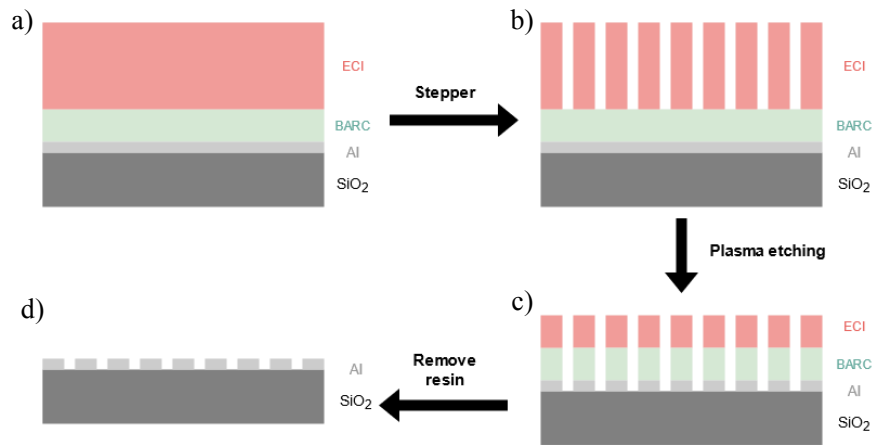


Figure 96. Process workflow for the fabrication of Al grating couplers over the SiO_2 lower cladding.

After spin-coating and soft-bake of the BARC and ECI layers, a relatively wide range of exposure parameters was used to find out the best configuration. The dose was adjusted from 800 to 1100 J/m^2 to obtain different duty cycles, and to determine which one was adapted to reach our targeted Al grating coupler duty cycle after plasma etching. It was found that in order to guarantee

the success of the subsequent steps, it was important to perform the photolithography and the etching without any delays.

For a surface smaller than $200 \mu\text{m}^2$, the etch rate starts to show a dependency on the surface of the pattern to be etched [101], as illustrated in **Figure 97**. As our pattern present small features, and considering the relatively thick layer of ECI, we applied an over etching of 30 s for each step, to ensure a clean interface in the small gaps of the grating coupler. As our process requires three photolithography levels, it is very important to keep the sample surface clean for each step, as any defects can impact the ability to accomplish the automatic alignment positioning required. At this point, dry etching has proven to be superior to keep the calibration pattern clean over the wet etching method.

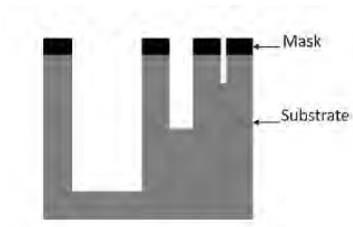


Figure 97. For the same material, the etch rate is lower on a smaller pattern during the plasma etching.

Table 12. Fabrication process of grating coupler with relevant parameters.

Lower cladding	4" Si wafer + 2.5 μm SiO ₂ cladding (deposited by PECVD)
Spin-coating	BARC 200nm T=30s; V=3000rpm, Acc=4000rpm/s
Soft bake	200°C 60s
Spin-coating	ECI 1.1 μm T=30s; V=3600rpm, Acc=4000rpm/s
Soft bake	90°C 60s
Photolithography by Stepper	Dose: 800,830....1100 J/m ² Focus: -0.4
PEB	110°C 120s
Development	MF-CD-26 90s
Rinse	DI water
Plasma etching	BARC/Al/ Remaining ECI

Table 13. Etching parameters during ICP-RIE.

Recipes	Gas (sccm)	Pressure	Power	Etching speed (nm/min)
BARC	O ₂ (25)/CF ₄ (5)/CHF ₃ (5)/Ar(5)	5mT	300W/40W	300
Al	Cl ₂ (20)	5mT	200W/10W	60

As we were unsure that increasing the etching time of 30 s would be enough to fully etch laterally the profile of the grating coupler, we also tested an over etching time of 90 s to compare the results. **Figure 98** shows that the lateral etching rate of this recipe is not preponderant. Due to the ECI thickness, the Al lines pattern below remains well protected.

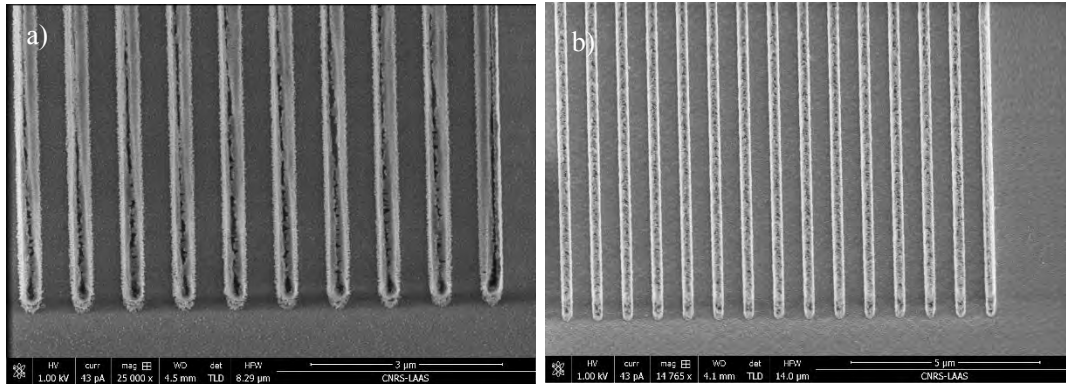
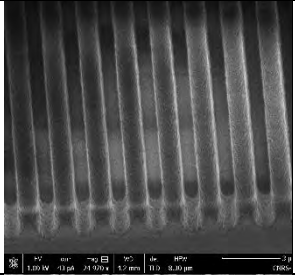
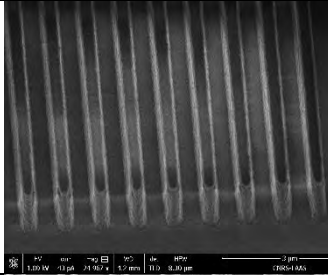
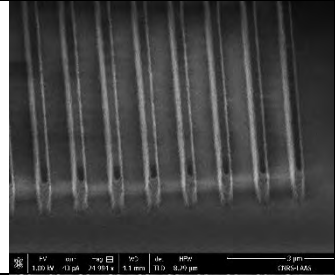
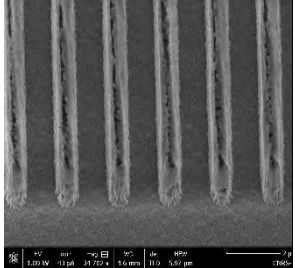
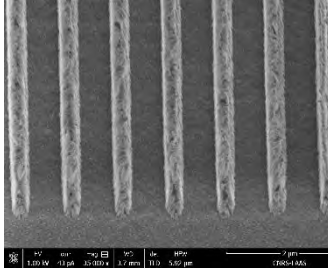
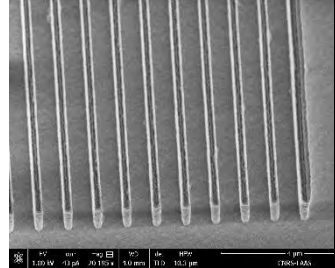


Figure 98. A 30s over etching time does not affect too much on the profile and duty cycle of pattern. a) Over etching time is 30s. b) Over etching time is 90s.

As there was only scarce experience related to aluminum etching by ICP-RIE in the LAAS cleanroom, it was essential to characterize the samples after each technological step, to assess the effect of each parameters on the patterns. A selection of relevant SEM images obtained during these characterizations are presented in **Table 14**. As expected, it can be clearly observed that the duty cycle decreases as the exposure dose increases. With the help of the BARC layer, the patterns are well resolved, even with the relatively thick ECI layer, and the uniformity of the SiO₂ deposit led to a much higher reproducibility of the pattern over the wafer compared to the results obtained with a CYTOP lower cladding.

Table 14. Selection of SEM characterization images after the stepper exposure and the ICP-RIE etching each step during the fabrication process. The duty cycle of grating coupler decreases as dose of stepper increases.

Fabrication step	Dose = 850 J/m ²	Dose = 950 J/m ²	Dose = 1050 J/m ²
Stepper			
Plasma etching			

As we first envisioned that the Al etching step would be the most challenging, we initially focus on optimizing the fabrication steps of **Figure 96** from a) to c), stopping before the removal of the remaining ECI photoresist and the BARC layer below. However, this final photoresist removal that was anticipated to be straightforward proved to be problematic, as illustrated **Figure 99**. Unexpected protrusions appear next to the grating coupler patterns, resulting in a distortion of the lines.

A subsequent cleaning with plasma O₂ did not fully remove these defects, with the additional drawback of polluting the sample with residues that were spread around the grating coupler, thus contaminating the sample surface.

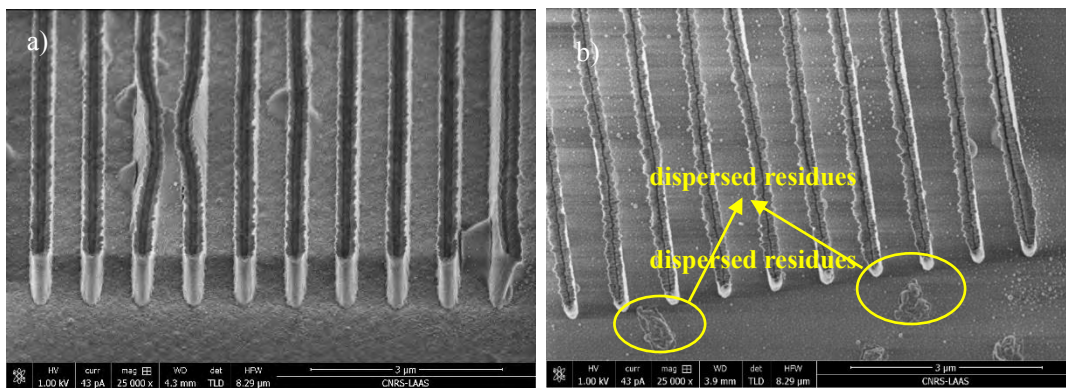


Figure 99. a) Protrusions appear next to grating coupler lines and pull the patterns to be distorted. b) A re-added plasma O₂ disperse the residues and contaminates the surface of sample.

By consulting the past work experience of several TEAM members, we finally found an explication [102]: after the Cl_2 etching of the unprotected Al layer, compounds in the forms of AlCl_x are produced. Once these by-products leave the vacuum environment (plasma chamber) and contact with air, the AlCl_x residue will continue to over etch the surface as HCl , resulting in the creation of a more complex by-product that cannot be eliminated by acetone solution or Plasma O_2 treatment in the following stripping step. To resolve this, two methods were evaluated. In the first one, the wafer is directly rinsed with deionized water after Cl_2 etching, as the water flow is expected to wash away the by-products on the Al surface and prevent the deeper chemical reaction. The second method consist in an oxygen plasma directly after the Cl_2 etching step, i.e. without interrupting the vacuum environment in the chamber, to prevent the formation of the observed bumps. After comparing the results obtained with the two methods in **Figure 100**, the second one was favoured, as the DI water flow tended to deform the grating coupler profile, as seen **Figure 100-a**.

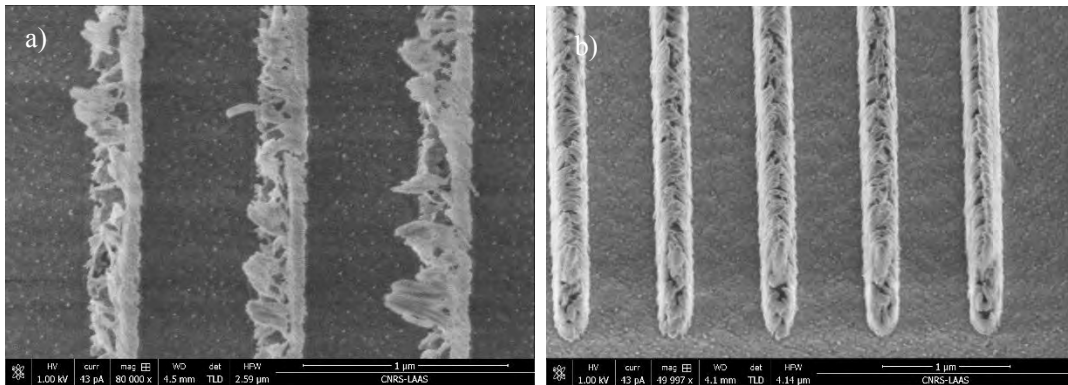


Figure 100. Grating coupler before stripping. a) A deionized water flow is used to avoid residue bumps. b) A chaining oxygen plasma without interruption of vacuum is used to avoid the formation of residue.

We initially planned two standard methods to do the stripping: (i) a micro-wave plasma to clean the wafer surface, (ii) an heated PG remover in an ultrasonic bath to efficiently separate the residual organic matter (the protection layer of photoresist) from the surface, but both methods proved to be unsatisfactory, as they both damaged our nano-structures as illustrated **Figure 101**.

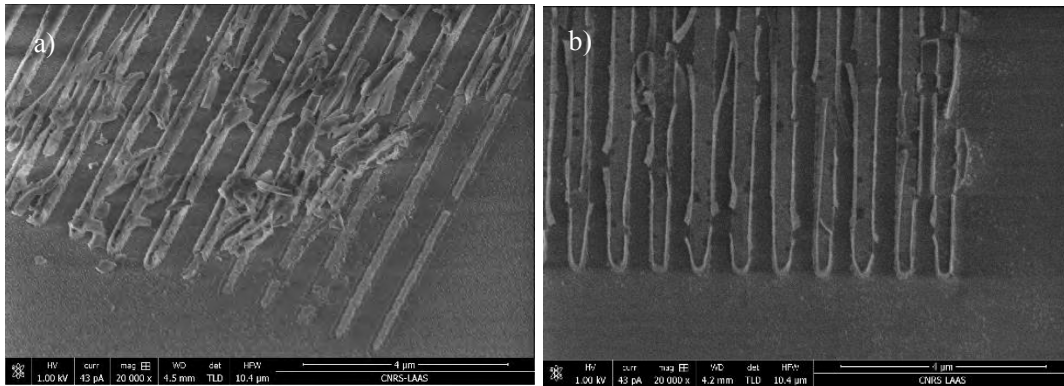


Figure 101. Illustration of the damages caused by (a) an ultrasonic bath with PG remover and (b) oxygen plasma on the nanometric features of the grating couplers.

In the meantime, J.B. Doucet, a chemical engineer from TEAM, proposed two alternative stripping methods. In the first method, the wafer is exposed to UV-Ozone for more than 48h. This equipment produces ozone by irradiation of atmospheric oxygen at 185 nm, this will destruct the organic contamination by breaking C-C bonds and other activated forms of oxygen. In the second method, the wafer is immersed into concentrated nitric acid (99%) for 5 mins to strip the remaining photoresists. Even though the second method is much faster, considering its dangerousness due to the acid concentration and the difficulty of obtain a precise control of time (as the nitric acid continue etching the Al layer after stripping), we finally choose to use the UV-ozone treatment for this step as the results obtained were the most satisfactory. This method is softer than oxygen plasma to eliminate the photoresist residues and proved to limit metal degradation, as shown on the close-up SEM image **Figure 102**.

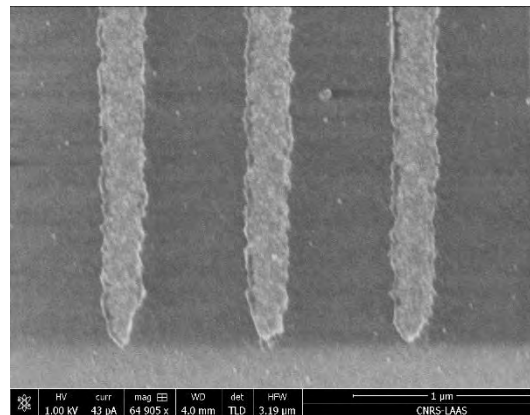


Figure 102. Al grating coupler fabricated by plasma etching and then stripped by UV-Ozone.

After many efforts and the evaluation of the different methods that could be applied within our limited remaining time, we finally manage to fabricate acceptable Al grating couplers on a SiO₂ lower cladding. Using the same fabrication process described in section IV.2.3. While this process

takes a very long period, it was proved to be more reproducible than the processes applied on CYTOP lower cladding. We can then add the SU-8 waveguides and tapers over the grating couplers.

IV.2.7 Optical test setup evolution

Due to the duration of certain technological steps, and an unexpected maintenance of stepper, we took the remaining time to improve the optical bench as illustrated **Figure 103**.

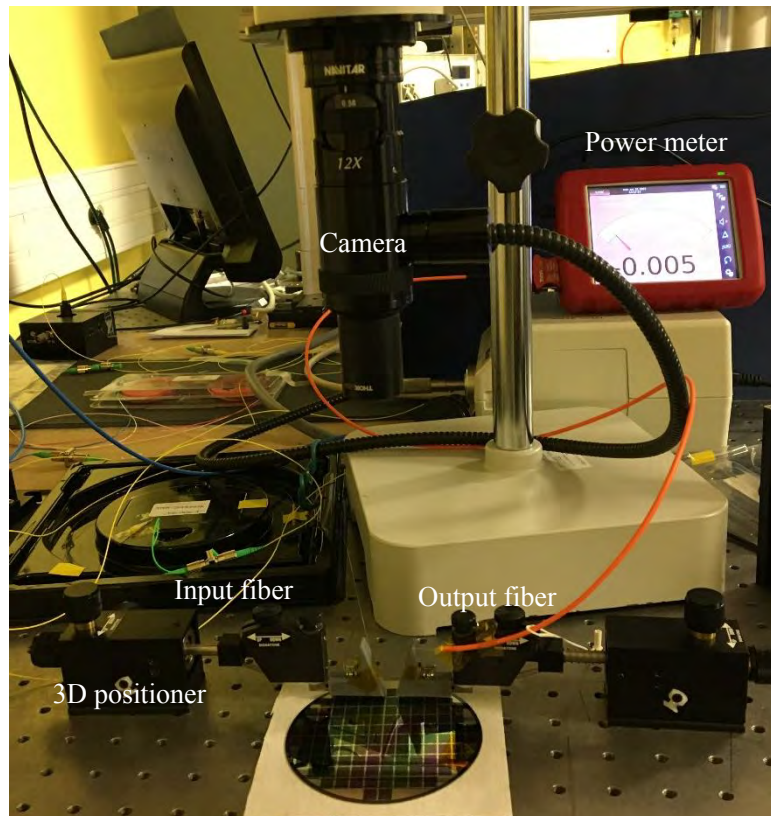


Figure 103. Improved optical bench for characterization of components.

In this configuration, we use optical fibers for light injection and collection. Both the input and output fibers are attached to micro-positioners by the mean of 3D printed V-grooves that positioned the fibers at the required 19° angle. These V-groove are made using a Formlabs Form 3 printer, an affordable desktop stereolithography (SLA). With an 85-micron beam size, the resolution of this printer is theoretically not sufficient to obtain the small V-groove dimensions required (approx. $150\mu\text{m}$ depth); however, by careful design, and playing with the tendency of the printer to overexpose, we managed to custom-made V-groove supports with a 19° angle that allowed us to use micropositioners that are usually used in electrical probe systems. This angle can be changed by modifying the 3D design, and as the printing time is relatively short (approximately 2 hours for two V-groove holders), modification can be efficiently made on the setup. The micropositioners

coupled with the 3D printed V-groove allows adjustments in XYZ axes to ensure proper alignment of the optical fibers with the grating couplers. A power meter is connected to the output fiber to help adjust the alignment effect. A camera equipped with a Navitar long range objective allows real time observation of the patterns on the wafer. The same program mentioned in section IV.2.5 is used to control the power and wavelength of light source.

Compared with the initial optical bench described in **Figure 91**, the sample can be placed by hand in a larger scale and its movement is no longer limited by the scope of positioner, thus the wafer dicing step is avoided to reduce processing time.

To get a more flexible adjustment, a second upgraded optical bench was recently installed adapting the VCSEL test bench as shown in **Figure 104**.

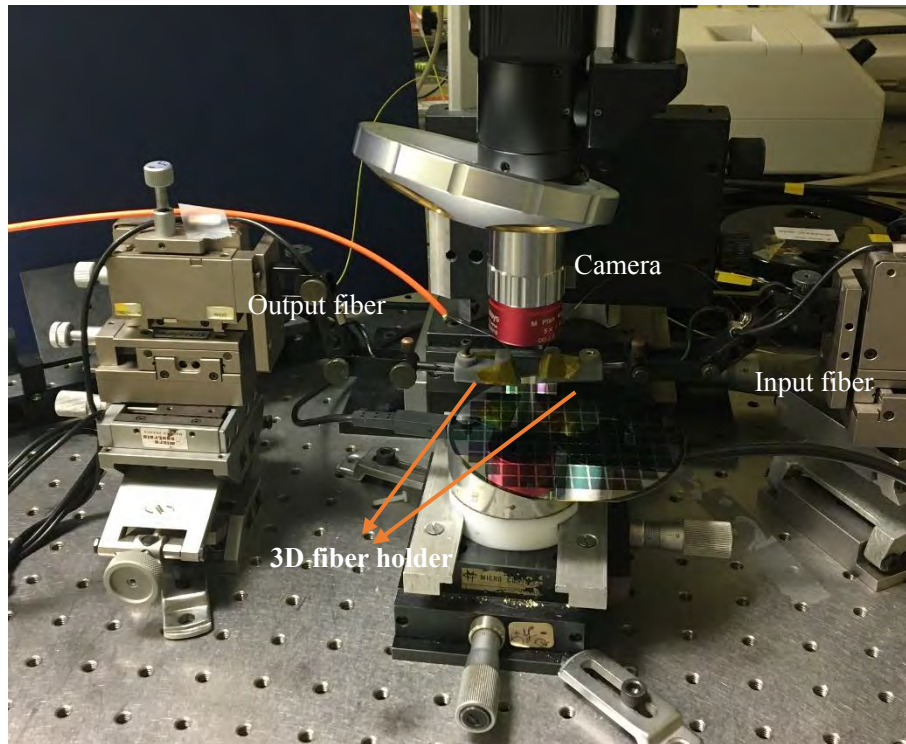


Figure 104. Upgraded optical bench for characterization of components.

In this configuration, the XY travel ranges are much higher. To make this set up usable, two angle adjusters were added on the 3D positioners: this configuration donates a ± 3 degrees of freedom on the input/output fiber in order to observe the influence of injection and collection angles on the coupling efficiency, considering the grating couplers have been designed for a 19° angle. The sample can be fixed by vacuum at bottom to provide a better stability during the manipulation.

A semi-manufactured wafer (with only imperfect grating couplers with SU-8 waveguide on SiO₂ substrate, without adding the upper CYTOP cladding) was used for performance testing of the new optical bench. Its coupling curves are shown in **Figure 105**.

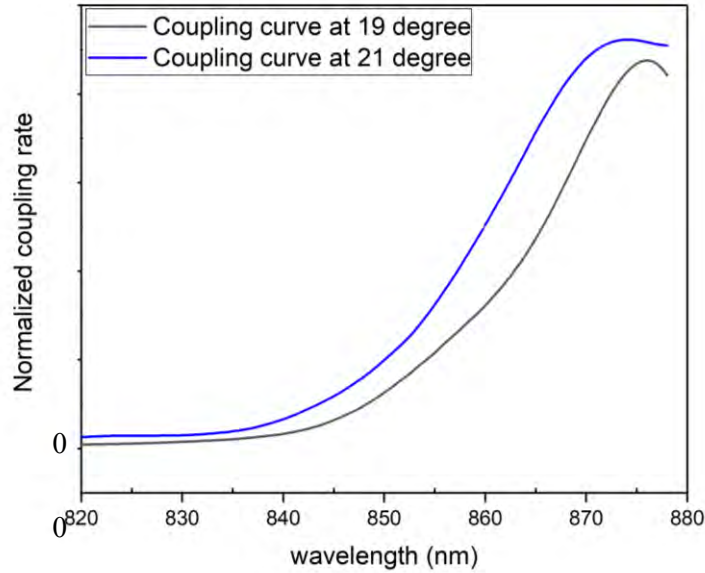


Figure 105. Normalized coupling rate of semi-manufactured wafer for the performance testing of upgraded optical bench.

A coupling peak appears around 870nm, and the coupling rate increases with a higher injection degree. As the sample used in this test has a very rough surface (caused by AlCl_x compounds) as shown in **Figure 100**, with a nearly 0.8 duty cycle (higher than designed value at 0.5) caused by the stepper error, and the lack of upper CYTOP cladding layer, the measured coupling efficiency of each grating coupler is much smaller than previous simulation. While even under these unfavorable conditions, the curve data can still be obtained clearly, which verifies that the applicability of this latest optical bench.

After these steps, the final micro-ring layer can be added by using the same manufacturing parameters explicated in paragraph IV.2.3. However, due to the unexpected technological difficulties in obtaining satisfying grating couplers, we didn't have enough time to conduct the subsequent fabrication steps. These steps include CYTOP upper cladding deposition and etching to obtain the appropriate gap (described in paragraph IV.2.4), and subsequent spin-coating and stepper lithography of an SU-8 layer over the CYTOP upper cladding, both of which are not foreseen as risky technological steps. A preliminary study on a PANI sensitive layer for specific detection of NH₃ is presented in chapter V.

Chapter V

Towards a NH₃ gas sensor with a PANI sensitive layer

V. Towards a NH₃ gas sensor with a PANI sensitive layer

As described in the introduction of this manuscript, Ammonia (NH₃) is of particular interest as it represents an important hazard to human health due to its toxic and corrosive nature. Polyaniline (PANI) is well known for its good affinity with ammonia thanks to its chemical structure, and offers interesting properties regarding NH₃ sensing: upon NH₃ exposure, PANI undergoes a deprotonation (Figure 106) which rates is related to the ammonia concentration [103]. This phenomenon translates into modifications of the PANI refractive index and absorption properties [40], which will influence the microring resonator optical response. This sensing strategy has already been successfully demonstrated for SU-8 waveguide-based sensors [37] and as such represents a good approach in order to validate our generic gas sensing platform.

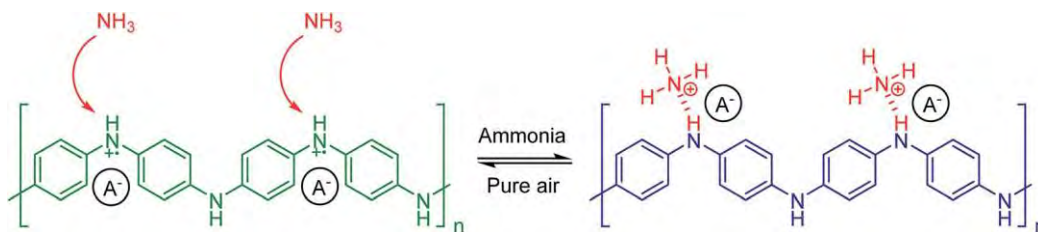


Figure 106. PANI undergoes a deprotonation process upon NH₃ exposure [103].

The Polyaniline (PANI) chosen as a sensitive layer is directly deposited on the SU-8 microresonator surface to realize the final integrated optical NH₃ gas sensor. As first step, the deposition of the pure polyaniline sensitive layer is carried out both on glass substrates and on silicon substrates as well: deposition on a glass substrate makes it possible to determine the optical properties of the PANI layer using UV-VIS spectroscopy, while deposition on a Si substrate is used to characterize the sensitive layer refractive index variation toward ammonia using ellipsometry. SU-8 samples are also used to study the deposition onto the final material.

V.1 Method of deposition of the PANI

The deposition of PANI is prepared by chemical way, and then coated by two methods as in-situ and spin coating. This part of the work was led in collaboration with Jean-Baptiste Doucet and Benjamin Reig from TEAM service.

V.1.1 Deposition of PANI in-situ

Prior to the PANI deposition, the solution is prepared according to the well-known procedure in the literature [104] [105], with the addition of an homogenization step using a magnetic stirrer. This procedure takes place in several steps.

Firstly, the following solutions are prepared:

- Solution 1: 1ml of aniline (Ani, Sigma Aldrich, 99.5%) is mixed with an aqueous solution (100 ml) of hydrochloric acid 1M (HCl, Sigma Aldrich, 37%)
- Solution 2: 0.56g of ammonium persulfate ((NH₄)₂S₂O₈, Aldrich, 98%) is dissolved in 5ml of HCl (1mol/L).
- Solution 3: 100ml of HCl (0.1 mol/L)
- Solution 4: solution 1 is prepared again

Once the solutions are prepared, the cleaned substrate to be coated is immersed in solution 1. This solution is kept homogeneous with the help of a magnetic stirrer set at 80 rpm, while solution 2 is quickly added. The addition of (NH₄)₂S₂O₈ will induce the polymerization of aniline: the solution then becomes viscous and turn to green, in the meantime a PANI film forms on the surface of the support. The thickness of the film depends on the immersion time in the solution.

After that, the sample is rinsed with solution 3 for one minute, then immersed in solution 4 for 30 minutes. This last step is necessary in order to transform all the forms of presented PANI into emeraldine salt (conductive form). Finally, the deposits are rinsed with solution 3 and dried with compressed air at room temperature.

V.1.2 Deposition of PANI by spin-coating

A second method based on spin-coating is evaluated, based on the steps detailed in reference [106] Firstly, the emeraldine salt must be synthesized according to the procedure of in-situ deposition previously described, with the main difference being that the PANI has to be recovered in a powder form. As the spin-coating method requires a relatively large amount of polyaniline, a mixture of solution 1 and solution 2 is stirred for an hour, and then filtered in order to collect the powder issued from the polymerization step. The obtained powder is then washed by solution 3, and finally mixed with solution 4 for one hour. At the end of this step, the doped form of PANI is obtained in solid form, it should be dried under vacuum for 48h. Since the doped form of PANI is not soluble in any solvent, it needs to be treated with ammonia hydroxide solution (NH₄OH, Aldrich) for two hours, then filtered and dried under vacuum for 48h, to get undoped form of PANI. The dried powder should be collected and stored for the spin coating depositing.

In order to deposit the PANI layer by spin-coating, it is necessary to dissolve a quantity of PANI-de-doped powder in N-methyl-2-pyrrolidone (NMP, Aldrich, 99%) solution, then the liquid will spread over the substrate during the high-speed rotation. Although the spreading phase is completed in a few seconds, the rotation is maintained in order to ensure the uniform distribution of the solvent and thus achieve a significant thickness. The final thickness is adjusted by a combination of the rotation speed, the acceleration, and the spreading time. For a rotation speed of 2000-3000 rpm, the final deposition thickness on Si, SU-8, or glass substrates will be 40-80nm.

After the deposition, the sample goes through an annealing step conducted at 90°C for 30mins. This heat treatment is necessary to desorb the residual solvent from the PANI and help to enhance the adhesion of the PANI film on the substrate.

V.2 Characterization of the PANI sensitive layer

V.2.1 Thickness and morphology

First and foremost, the thickness of the PANI layers obtained with the in-situ method is measured by Tencor stylus profilometer. **Figure 107** shows the evolution in the thickness of the PANI layer, deposited on Si, SU-8 and glass substrates over deposition time. We can see that the thickness of the PANI film changes in the same way on the three types of substrates. In the first short time (< 12mins for the Si substrate, < 18mins for the SU-8 substrate, and < 15mins for the glass substrate), the thickness of the PANI increases rapidly with time. Beyond that, the thickness begins to decrease. The maximum thickness of PANI coating is obtained on those of SU-8 substrate. We also note that this decrease is more remarkable for the layers deposited on glass and Si substrate.

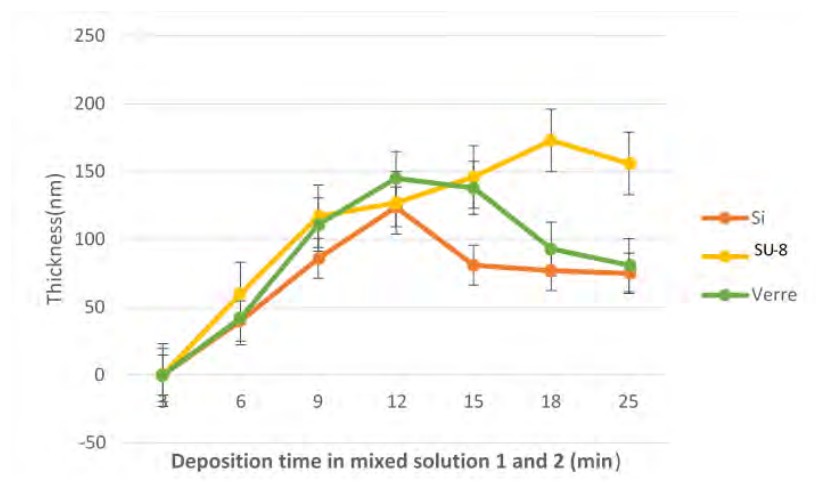


Figure 107. The evolution in the thickness of the PANI layer, deposited on Si, SU-8 and glass substrates over deposition time.

This difference could be attributed to the difference in the surface quality of Si, SU-8 and glass substrates, but also probably due to nucleation phenomenon as described in [107].

Thanks to this first study, we can conclude that it is relatively easy to deposit 150nm of PANI with a good reproducibility on SU-8 by dipping the substrate into the solution during 15 minutes.

Using Scanning Electron Microscopy (SEM), it is possible to visualize the morphology of the deposited thin layer. **Figure 108** presents the SEM photographs of PANI layer coated on Si substrate. By applying the same time of deposition (12mins here), the thin layers of PANI produced in-situ with an agitation of 80 rpm are denser and more homogeneous than those without agitation. The small particles of PANI are deposited in the form of grains, the size of particles is on function of the deposition time, varies between 100nm and 300nm.

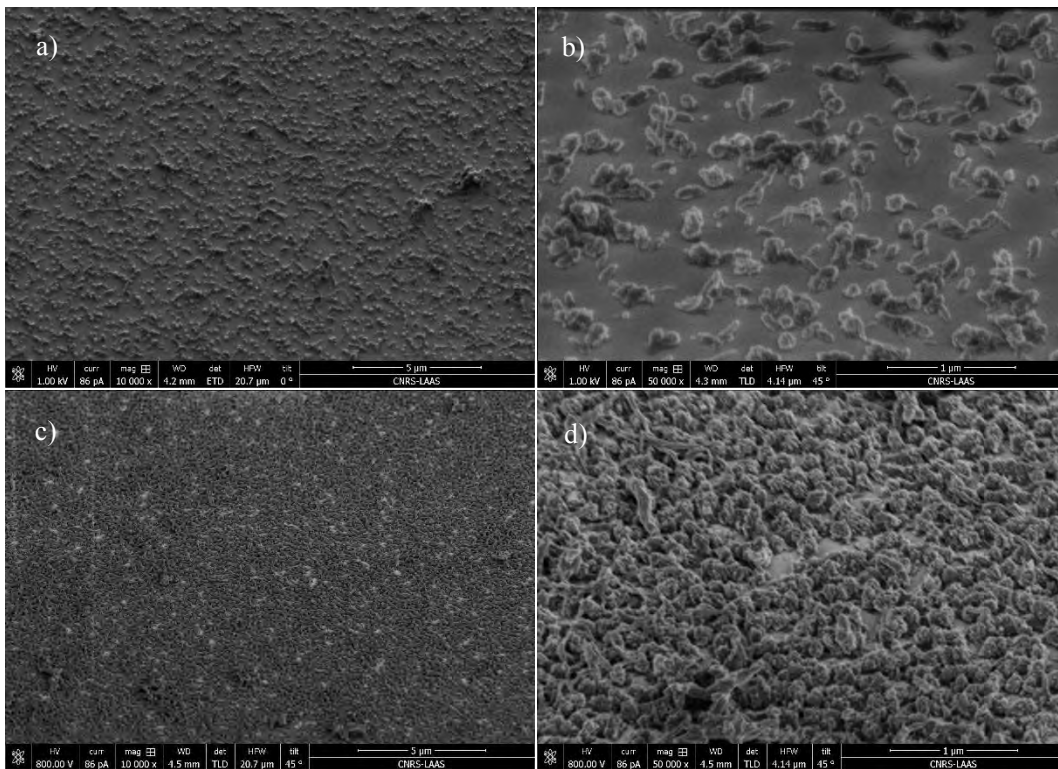


Figure 108. PANI coating produced in situ without (a,b) /with (c,d) an agitation of 80rpm.

A deposition test was also carried out on SU-8 surface, as our final goal is to coat PANI sensitive layer onto SU-8 microresonators. **Figure 109** shows a SEM comparison between the bare SU-8 surface which is dense, homogeneous and very smooth, while the PANI layer deposited on SU-8 exhibits high porosity with a typical grain size around 200nm. This porous structure of PANI film could be a real advantage to enhance the detection of ammonia gas as it offers a high specific surface. It should be noted that by adjusting the reaction time, the surface morphology of the PANI layers can be adjusted, as the roughness increases with the reaction time.

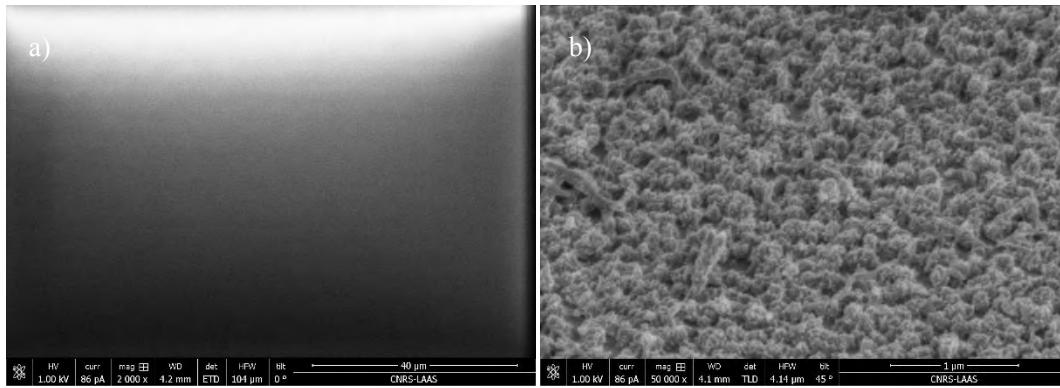


Figure 109. SU-8 surface without (a) / with (b) PANI coating.

In order to validate the in-situ approach for our microring resonators, a dummy SU-8 waveguide on a CYTOP lower cladding was used and exposed to the same coating method. The **Figure 110-a** shows that the PANI film coated well on the surface, here a 1 μm width SU-8 waveguide, which is very beneficial to our microsystem.

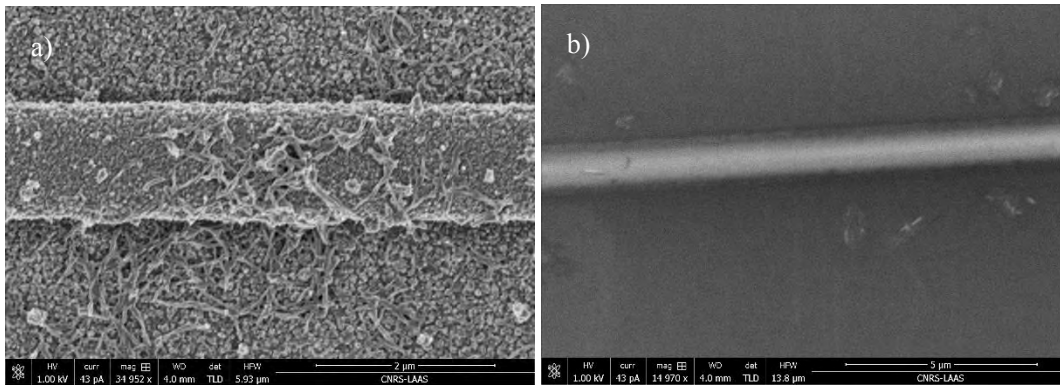


Figure 110. PANI coating on SU-8 waveguide which is deposited on the CYTOP lower cladding. a) PANI is coated by method in-situ. b) PANI is coated by method spin coating.

We then proceed to the characterization of the deposition of PANI by spin coating. The method proved to be somehow less convenient than the in-situ method, considering that: (i) the overall processing time is much longer than for the in-situ method, as it involves two vacuum drying steps of 48h each, and (ii) the amount of PANI coated on the SU-8 surface by this method is smaller as shown in **Figure 110-b**. While adjusting the spin-coating parameters, the drying steps, or the dilution ratio of the powder could lead to different results, we concluded that the in-situ deposition method was more suited to optimize our microsystem in terms of detection potential performances due to the relative convenience of adjusting the specific surface or the thickness. Another great advantage is that the samples can be functionalized individually after wafer dicing (with the help of shadow-masking for example), while this would be hard to achieve for spin-coating as it is not suited to small, square-shaped substrates.

V.2.2 PANI optical parameters upon NH₃ exposure

For the gas sensors using a sensitive coating, the coating material will react to the target gas and then change its optical parameters as refractive index n or absorption coefficient α . When PANI coating is exposed to the NH₃ vapor, the de-doping in PANI material occurs which affect the complex phase velocity of guided beam in the SU-8 waveguide below. This change can be quantitatively expressed as the change of the complex effective refraction index which includes a pure index change in real part (n) and an absorption change in imaginary part (α). Therefore, the changes of optical index and absorption coefficient of PANI layer can be detected, in our case at a working wavelength of around 850nm.

We prepared some glass substrates with a coating of PANI deposited with the aforementioned in-situ method and exposed them to NH₃ vapors for different times, ranging from 1 min to 3 hours, and then proceed to UV-VIS absorbance measurements using a Perkin-Elmer LAMBDA 650 spectrophotometer. It should be noted that while the exposure time of the PANI to the NH₃ vapors was controlled, the absorbance measurements could not be made in real time, as we required some time to load the samples in the spectrophotometer and run the measurements: during this time, we could visually see a change in the substrates color due to the desorption of NH₃, which while it confirms the benefit that the reaction is fully reversible at room temperature, led to an underestimation of the actual absorption directly after exposure. We try to keep the time between exposure and analysis constant for all the data shown in **Figure 111**.

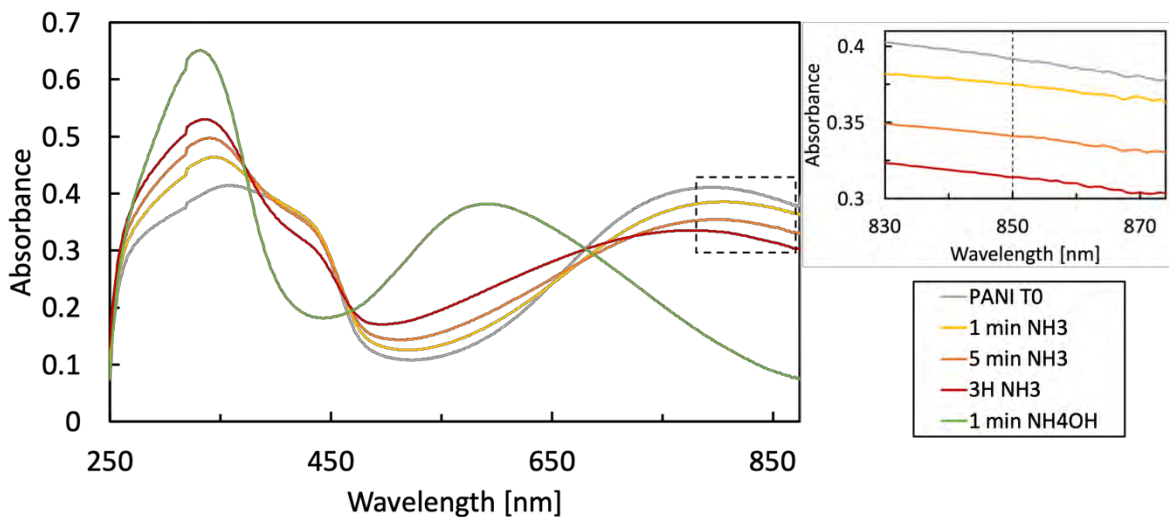


Figure 111. UV-VIS absorption spectra of PANI coated glass substrates upon different exposure times to NH₃ and NH₄OH. Inset focuses on the absorbance variation around 850 nm.

The absorbance spectrum is in good agreement with those reported in the literature and shows that, the absorbance of “homemade” PANI coating with the thickness targeted for our microsystem varies according to the duration of exposure to ammonia vapors. Even for the shortest exposure

time (1 minute), the inset allows to see a change rate around 5% since the absorbance value changes from $A = 0.39$ to 0.37 . After an exposure of 5 minutes, this value changes around 12.8% from 0.39 to 0.34 at our targeted 850 nm working wavelength. The full absorbance spectrum confirms that with operating wavelength is well suited to NH_3 sensing, as the amplitude of variations at this wavelength is relatively large compared to other parts of the spectrum. Since our goal is to develop optical gas sensors in the NIR range, changes in other bands are not in our focus.

While we also planned to measure the evolution of the PANI refractive index upon NH_3 exposure using ellipsometry, due to the constraints of the technique both in terms of measurement time and exposed area, this requires a specific measurement cell in order to keep the sample exposed to NH_3 during the measurement. We worked on a 3D-printed test cell to perform these measurements, but this work is still in progress and was not completed at the time of writing this manuscript. However, it should be emphasized that several results based on RI-sensors have shown that NH_3 causes significant changes in the refractive index of PANI [108]. In addition, reversibility is one of the advantages of PANI for a sensor application, associated with the fact that it works at room temperature whereas some many other gas sensors work well only at high temperature to favorize adsorption and desorption.

V.2.3 Towards an integrated optical NH_3 gas sensor

Our final goal during this work was to propose a complete sensing system, integrating the transducer, a microring resonator with a PANI sensitive layer, a miniature, inexpensive, collimated VCSEL with integrated optics as the excitation source, and a photodiode as a detector. One of the key challenges during this work was to propose an architecture that would not require complicated, expensive and bulky optomechanical components that are normally required for sub-micron optical waveguides and features: this was achieved by the design and integration of Al grating couplers, that can offer interesting performance in terms of coupling efficiency due to the high optical indices contrast compared to polymer gratings.

Figure 112 shows an overall view of the fully integrated system which is based around a 3D printed housing. The optical microring resonators are visible in the center and are exposed to the surrounding gases through an opening in the housing. This opening can be easily replaced by a microchannel for an integration in a gas line for example. The design shown here is based on the actual microring resonators photomasks and is dimensionally accurate; as such it comprises seven distinct waveguides and resonators with their corresponding input/output grating couplers. The VCSELs PCB integrates seven independents collimated VCSEL sources. Each PCB possess vias that are used for obtaining a precise alignment thanks to corresponding alignment pins that are built in the 3D printed housing.

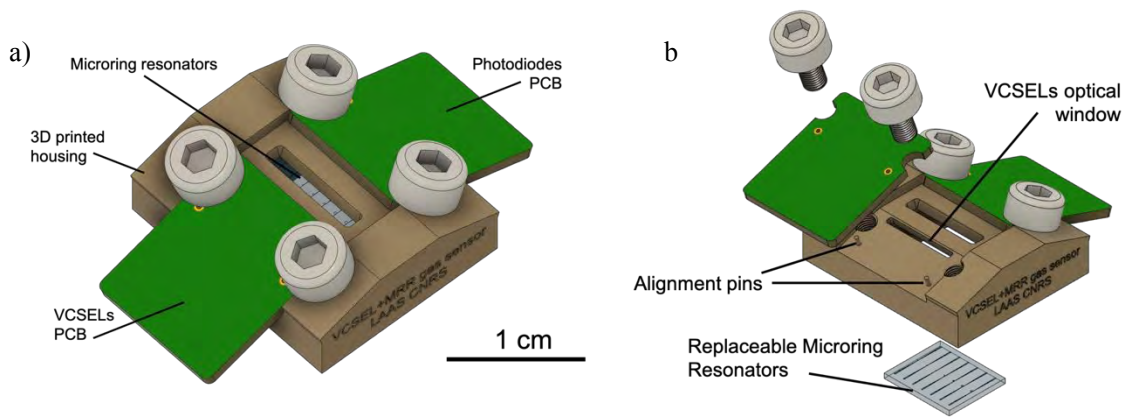


Figure 112. a) CAD rendering of the fully integrated optical gas sensor. b) Exploded view showing the alignment pins, the microring resonators chip, and the VCSEL optical window.

Common PCB manufacturers guaranty a via positioning precision < 1 mil ($1 \text{ mil} = 25.4 \mu\text{m}$), with high-precision PCBs that offers < 0.5 mil ($12.7 \mu\text{m}$) precision. The 3D printed housing has been designed to be fabricated with a Kloe Dilase 3D stereolithography that offers a $5 \mu\text{m}$ resolution [87]. Considering that the wafer dicing saw available at LAAS CNRS, a Disco DAD-321, offers a positioning precision of $3 \mu\text{m}$, it can be reasonably envisaged that with careful PCB design and VCSEL assembly, it is possible to obtain an alignment of the VCSEL collimated beam and the grating couplers of $\pm 20 \mu\text{m}$ maximum, without any optomechanical components like the micro-positioners typically required for such small optical structures.

Figure 113 gives some insight on the 3D printed housing, with an illustration of how the VCSELs are aligned according to the grating couplers, both in the XY plane thanks to the use of appropriate tolerances and alignment pins, and in the Z axis as the design guarantees the correct working distance between the VCSEL optics and the grating as well as the angle.

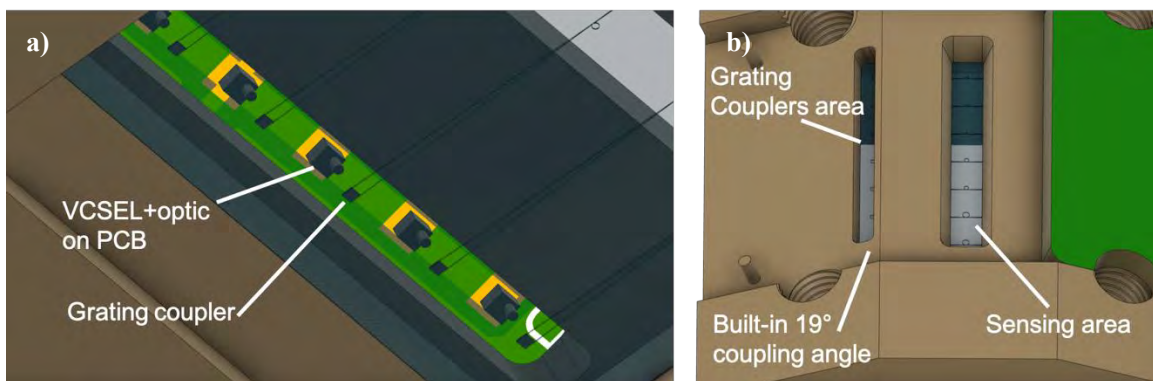


Figure 113. a) Detailed view of the collimated VCSEL matrix and the grating couplers observed from the bottom (through the Si substrate). b) Close-up view of the optical port showing the input grating couplers area, and the exposed sensing area with the microring resonators. A built-in slope of 19° ensures the injection angle is guaranteed.

Conclusion and perspectives

In this work, a compact guided wave optical gas sensor is designed basing on the use of low-cost polymer materials, a collective lithography technique, and a standard Si photodetector.

A collimated VCSEL source that can be easily integrated in this system is successfully fabricated using two different methods. Thanks to the 3D-printed polymer microlens fabrication method developed for the first time in this work, this process can be done in one step and in 10min, without any thermal step. The highlight is the micro lens for collimation can be fabricated directly on a $200\mu\text{m}\times 200\mu\text{m}$ chip already assembled and soldered on PCB and this leads to a spot size lower than $60\mu\text{m}$ on the coupling area, as aimed.

The fabrication process of the 800nm-period Aluminum grating couplers on CYTOP bottom cladding has been carefully optimized with stepper and a lift-off process. Our first tests indicate that this process can achieve good results in terms of period and with acceptable duty cycles. This CYTOP/SU-8/Al/CYTOP structure can accomplish desired coupling. Another fabrication process of 800nm-period Aluminum grating coupler on SiO_2 bottom cladding is also accomplished by using plasma etching. It has a higher yield compared with previous configuration. First measurements of the transmitted spectrum as a function of the emission wavelength and the coupling angle are made and still under study.

A highly adaptable optical test bench is established, with some replaceable low-cost fast-made components fabricated by 3D print technology. This feature makes it easier to adjust to an optimal light incident/exit angle, and can be extended to similar detections with another grating coupler dimension/material/working wavelength, etc. No pre-cutting process of wafer is required therefore this can prevent vibration and processing dust from damaging the sample, and a midway detection before the deposition of SU-8 microresonator is feasible, without affecting the subsequent stepper alignment process.

The methods of functionalization and deposition of chemically sensitive materials (PANI) are developed on SU-8 in order to obtain the sensitivity of integrated micro-resonators for optical gas sensor applications. A straightforward method for PANI deposition on the microresonator is successfully proposed.

In the end, an overall view of the fully integrated system was designed basing around a 3D printed housing. The light source part, grating coupler part, detection part can be easily replaced according to testing needs, each part can be adjusted to obtain a precise alignment thanks to alignment pins.

In the future, we will further optimize the light source part by exploiting the results of lens characterization and by proposing an optimized design of a VCSEL chip suited to lens integration. We will also optimize the fabrication of the sensitive layer part. In addition to the PANI sensitive layer, a multi-channel detector could be developed by carrying out research on a wide range of materials which are chemically sensitive on SU-8 as the basic material of the micro-resonator, such as CO₂, H₂, VOC and so on.

We will then mainly focus on the improvements on grating coupler, which determines the final energy efficiency of the entire system and brings us the most difficulties due to its tiny resolution. For the CYTOP surface, additional surface treatment processes will be tested to provide a better surface uniformity. For the SiO₂ surface, heating treatment under inert gas circumstance will be tried after plasma etching, to observe the surface improvement of Al grating coupler, other metal materials are also considered to work as grating coupler. The whole system will be then finished including the micro-ring and the integrated detector.

For the entire system, a 3D printed housing already designed will be developed with flexible adjustment pins, a multichannel sensor will be exploited.

References

- [1] A. Dey, "Semiconductor metal oxide gas sensors: A review," *Materials Science and Engineering: B*, vol. 229, pp. 206-17, 2018.
- [2] E. Bakker and M. Telting-Diaz, "Electrochemical sensors," *Analytical Chemistry*, vol. 74, p. 2781-800, 2002.
- [3] M. Cämmerer, T. Mayer, S. Penzel, M. Rudolph and H. Borsdorf, "Application of low-cost electrochemical sensors to aqueous systems to allow automated determination of NH₃ and H₂S in water," *Sensors (Switzerland)*, vol. 20, no. 10, p. 2814, 2020.
- [4] X. Liu, S. Cheng, H. Liu, S. Hu, D. Zhang and H. Ning, "A survey on gas sensing technology," *Sensors (Switzerland)*, vol. 12, pp. 9635-65, 2012.
- [5] H. Waechter, J. Litman, A. Cheung, J. Barnes and H.-P. Loock, "Chemical Sensing Using Fiber Cavity Ring-Down Spectroscopy," *Sensors*, vol. 10, pp. 1716-42, 2010.
- [6] J. Hodgkinson and R. Tatam, "Optical gas sensing: A review," *Measurement Science and Technology*, vol. 24, 2013.
- [7] V. Passaro, B. Troia, M. L. Notte and F. D. Leonardis, "Photonic resonant microcavities for chemical and biochemical sensing," *RSC Advances*, vol. 3, no. 1, pp. 25-44, 2013.
- [8] G. Besselink, R. Heideman, E. Schreuder and L. Wevers, "Performance of Arrayed Microring Resonator Sensors with the TriPleX Platform," *Journal of Biosensors & Bioelectronics*, vol. 7, 2016.
- [9] Y. Zhao, "Optical feedback sensing in microfluidics: design and characterization of VCSEL-based compact systems," Thesis, Institut National des Sciences Appliquées de Toulouse, 2017.
- [10] Y. Ma, A. Vicet and K. Krzempek, "State-of-the-Art Laser Gas Sensing Technologies," *Applied Sciences*, vol. 10, no. 2, p. 433, 2020.
- [11] D. Popa and F. Udrea, "Towards Integrated Mid-Infrared Gas Sensors," *Sensors*, vol. 19, no. 9, p. 2076, 2019.
- [12] A. Gutierrez-Arroyo, E. Baudet, L. Bodiou, J. Lemaitre, I. Hardy, F. Fajjan, B. Bureau, V. Nazabal and J. Charrier, "Optical characterization at 77 μm of an integrated platform based on chalcogenide waveguides for sensing applications in the mid-infrared," *Optics Express*, vol. 24, no. 20, pp. 23109-17, 2016.
- [13] D. Popa, R. Hopper and P. Carrington, "Special Issue "Low Cost Mid-Infrared Sensor Technologies"," 2020. [Online]. Available: https://www.mdpi.com/journal/sensors/special_issues/mid-infrared_sensor.
- [14] M. Gorodetsky, A. Savchenkov and V. Ilchenko, "Ultimate Q of optical microsphere resonators," *Optics Letters*, vol. 21, no. 7, pp. 453-55, 1996.
- [15] I. Grudin, V. Ilchenko and L. Maleki, "Ultrahigh optical Q factors of crystalline resonators in the linear regime," *Physical Review A - Atomic, Molecular, and Optical Physics*, vol. 74, pp. 1-9, 2006.
- [16] F. Vollmer, L. Yang and S. Fainman, "Label free detection with high Q microcavities: A review of biosensing mechanisms for integrated devices," *Nanophotonics*, vol. 1, pp. 267-91, 2012.
- [17] F. Vollmer and T. Rowland, "Label-free, high sensitivity detection of biomolecules using optical," *B.I.F. FUTURA*, vol. 20, pp. 239-44, 2005.
- [18] T. Yoshie, L. Tang and S. Y. Su, "Optical microcavity: Sensing down to single molecules and atoms," *Sensors*, vol. 11, pp. 1972-91, 2011.
- [19] F. Vollmer and S. Arnold, "Whisperin g gallery mode biosensing: Label free detection down to single molecules," *Nature Methods*, vol. 5, pp. 591-96, 2008.

- [20] F. Vollmer, D. Braun, A. Libchaber, M. Khoshshima, I. Teraoka and S. Arnold, "Protein detection by optical shift of a resonant microcavity," *APPLIED PHYSICS LETTERS*, vol. 80, no. 21, p. 4057, 2002.
- [21] A. Elmanova, P. An, V. Kovalyuk, A. Golikov, I. Elmanov and G. Goltsman, "Study of silicon nitride O-ring resonator for gas-sensing applications," *Journal of Physics: Conference Series*, vol. 1695, no. 012124, 2020.
- [22] P. Xing, D. Ma, K. Ooi, J. Choi, A. Agarwal and D. Tan, "CMOS-Compatible PECVD Silicon Carbide Platform for Linear and Nonlinear Optics," *ACS Photonics*, vol. 6, pp. 1162-7, 2019.
- [23] D. Cai, J. Lu, C. Chen, C. Lee, C. Lin and T. Yen, "High Q-factor microring resonator wrapped by the curved waveguide," *Scientific Reports*, vol. 5, pp. 1-8, 2015.
- [24] C. Y. Chao, W. Fung and L. J. Guo, "Polymer microring resonators for biochemical sensing," *IEEE Journal of Selected Topics in Quantum Electronics*, vol. 12, no. 1, pp. 134-42, 2006.
- [25] T. Ling, S. L. Chen and L. J. Guo, "Fabrication and characterization of High Q polymer micro ring resonator and its application as a sensitive ultrasonic detector," *Optics Express*, vol. 19, no. 2, p. 861, 2011.
- [26] X. Jiang, A. Qavi, S. Huang and L. Yang, "Whispering gallery microsensors: a review," 2018. [Online]. Available: <https://arxiv.org/abs/1805.00062>.
- [27] C. Delezoide, "Polymer microring resonators for optofluidic evanescent field sensors," Ecole normale superieure de Cachan, Cachan, 2012.
- [28] Y. Ma, B. Dong and C. Lee, "Progress of infrared guided-wave nanophotonic sensors and devices," *Nano Convergence*, vol. 7, no. 12, 2020.
- [29] V. Passaro, C. d. Tullio, B. Troia, M. L. Notte, G. Giannoccaro and F. D. Leonardis, "Recent advances in integrated photonic sensors," *Sensors (Basel, Switzerland)*, vol. 12, no. doi:10.3390/s121115558, p. 15558–98, 2012.
- [30] C. Ciminelli, C. Campanella, F. Dell'Olio, C. Campanella and M. Armenise, "Label-free optical resonant sensors for biochemical applications," *Progress in Quantum Electronics*, vol. 37, no. 2, pp. 51-107, 2013.
- [31] P. Girault, "Micro-résonateurs intégrés pour des applications," UNIVERSITÉ DE RENNES 1, Rennes, 2016.
- [32] G. Mi, C. Horvath, M. Aktary and V. Van, "Silicon microring refractometric sensor for atmospheric CO₂ gas monitoring," *Optics Express*, vol. 24, no. 2, pp. 1773-80, 2016.
- [33] M. Eryürek, Y. Karadag, S. Anand, N. Kilinç and A. Kiraz, "Hydrogen and humidity sensing based on WGMs of elastic polymer optical microresonators," in *Progress in Electromagnetics Research Symposium*, 2015.
- [34] G. Mi, C. Horvath and V. Van, "Silicon photonic dual-gas sensor for H₂ and CO₂ detection," *Optics Express*, vol. 25, no. 14, pp. 16250-9, 2017.
- [35] J. Tao, X. Wang, T. Sun, H. Cai, Y. Wang, T. Lin and D. Fu, "Hybrid Photonic Cavity with Metal-Organic Framework Coatings for the Ultra-Sensitive Detection of Volatile Organic Compounds with High Immunity to Humidity," *Scientific Reports*, vol. 7, p. 41640, 2017.
- [36] D. Chauvin, J. Bell, I. Leray, I. Ledoux-Raka and N. C.T., "Label-free optofluidic sensor based on polymeric microresonator for the detection of cadmium ions in tap water," *Sensors and Actuators B: Chemical*, vol. 280, pp. 77-85, 2018.
- [37] A. Airoudj, D. Debarnot, B. Bêche and F. Poncin-Epaillard, "Development of an optical ammonia sensor based on polyaniline/epoxy resin (SU-8) composite," *Talanta*, vol. 77, no. 5, pp. 1590-6, 2009.
- [38] A. Airoudj, B. Bêche, D. Debarnot, E. Gaviot and F. Poncin-Epaillard, "Integrated SU-8 photonic gas sensors based on PANI polymer devices: Comparison between metrological parameters," *Optics Communications*, vol. 282, no. 19, pp. 3839-45, 2009.

- [39] D. Kwak, Y. Lei and R. Maric, "Ammonia gas sensors: A comprehensive review," *Talanta*, vol. 204, pp. 713-30, 2019.
- [40] M. El-Sherif, L. Bansal and J. Yuan, "Fiber optic sensors for detection of toxic and biological threats," *Sensors*, vol. 7, pp. 3100-18, 2007.
- [41] M. D. Garcia, V. Raimbault, S. Joly, L. Oyhenart, L. Bilbao, C. Nguyen, I. Ledoux-Rak, L. Bechou, I. Obieta and C. Dejous, "Enabling patterning of polymer optical devices working at visible wavelength using thermal nano-imprint lithography," in *Symposium on Design, Test, Integration and Packaging of MEMS/MOEMS (DTIP)*, Bordeaux, IEEE, 2017.
- [42] F. Meziane, V. Raimbault, H. Hallil, S. Joly, V. Conédéra, J. Lachaud, L. Béchou, D. Rebière and C. Dejous, "Study of a polymer optical microring resonator for hexavalent chromium sensing," *Sensors and Actuators B: Chemical*, vol. 209, pp. 1049-56, 2015.
- [43] K. Rasmussen, S. Keller, F. Jensen and A. Jorgensen, "SU-8 etching in inductively coupled oxygen plasma," *Microelectronic Engineering*, vol. 112, p. 35-40, 2013.
- [44] C. Barrios and V. Canalejas-Tejero, "An analysis of the surface-normal coupling efficiency of a metal grating coupler embedded in a Scotch tape optical waveguide," *Optics Communications*, vol. 382, pp. 477-84, 2017.
- [45] S. Scheerlinck, J. Schrauwen, D. Taillaert, D. V. Thourhout and R. Baets, "Efficient broadband and compact metal grating couplers for Silicon-on-Insulator waveguides," *Optics Express*, vol. 15, pp. 9625-30, 2007.
- [46] T. Suni, K. Henttinen, I. Suni and J. Mäkinen, "Effects of Plasma Activation on Hydrophilic Bonding of Si and SiO₂," *Journal of The Electrochemical Society*, vol. 149, no. 6, 2002.
- [47] B. Agnarsson, J. Halldorsson, N. Arnfinnsdottir, S. Ingthorsson, T. Gudjonsson and K. Leosson, "Fabrication of planar polymer waveguides for evanescent-wave sensing in aqueous environments," *Microelectronic Engineering*, vol. 87, pp. 56-61, 2010.
- [48] M. R. El-Gewely, "Biotechnology annual review," *Elsevier*, vol. 9, 1996.
- [49] [Online]. Available: https://en.wikipedia.org/wiki/SU-8_photoresist.
- [50] R. Feng and R. Farris, "Influence of processing conditions on the thermal and mechanical properties of su8 negative photoresist coatings," *Journal of Micromechanics and Microengineering*, vol. 13, no. 1, pp. 80-88, 2002.
- [51] X. Wang, J. Sun, C. Chen, X. Sun, F. Wang and D. Zhang, "Thermal uv treatment on su-8 polymer for integrated optics," *Optical Materials Express*, vol. 4, no. 3, pp. 509-17, 2014.
- [52] Y. Shang, Q. Ni, D. Ding, N. Chen and T. Wang, "Fabrication of optical fiber sensor based on double-layer su-8 diaphragm and the partial discharge detection," *Optoelectronics Letters*, vol. 11, pp. 61-64, 2015.
- [53] M. Magnuson, J. Guo, S. Butorin and A. Agui, "The electronic structure of polyaniline and doped phases studied by soft X-ray absorption and emission spectroscopies," *The Journal of Chemical Physics*, vol. 111, no. 10, 2012.
- [54] J. Elizalde, H. Hu and J. Saniger, "Comparison of NO₂ and NH₃ gas adsorption on semiconductor polyaniline thin films," *Revista Mexicana de Fisica*, vol. 51, no. 5, pp. 482-7, 2005.
- [55] D. Aspnes, "Optical properties of thin films," *Science Direct*, vol. 89, no. 3, pp. 249-62, 1982.
- [56] A. Airoudj, "Etude de guides d'onde polymères fluorés par voie plasma et développement de nouveaux capteurs photoniques à base de polyaniline," Le Mans, 2007.
- [57] S. Christie, E. Scorsone, K. Persaud and F. Kvasnik, "Remote detection of gaseous ammonia using the near infrared transmission properties of polyaniline," *Sensors and Actuators B: Chemical*, vol. 90, pp. 163-9, 2003.
- [58] R. G. Gould, "The LASER, Light Amplification by Stimulated Emission of Radiation," in *The Ann Arbor Conference on Optical Pumping, the University of Michigan*, 1959.

- [59] H. Soda, K. Iga and C. Kitahara, "GaInAsP/InP Surface Emitting Injection," *Japanese Journal of Applied Physics*, vol. 18, no. 12, pp. 2329-30, 1979.
- [60] K. Iga, S. Ishikawa, S. Ohkouchi and T. Nishimura, "Room-temperature pulsed oscillation of," *Applied Physics Letters*, vol. 45, no. 4, pp. 348-50, 1984.
- [61] M. Ogura, W. Hsin, M.-C. Wu, S. Wang and J. R. Whiennery, "Surface-emitting laser diode with vertical GaAs/GaAJAs quarter-wavelength multilayers and lateral buried heterostructure," *Applied Physics Letters*, vol. 51, no. 21, 1987.
- [62] F. Koyama, S. Kinoshita and K. Iga, "Room-temperature continuous wave lasing characteristics of a GaAs vertical cavity surface-emitting laser," *Applied Physics Letters*, vol. 55, no. 3, pp. 221-2, 1989.
- [63] S. F. Yu, Analysis and Design of Vertical Cavity Surface Emitting Lasers, John Wiley & Sons, Inc., 2003.
- [64] D. L. Huffaker, D. G. Deppe, K. Kumar and T. J. Rogers, "Native-oxide defined ring contact," *Applied Physics Letters*, vol. 65, no. 1, pp. 97-9, 1994.
- [65] M. Ortsiefer, C. Neumeier, J. Roskopf, S. Arafin, G. Böhm, A. Hangauer, J. Chen, R. Strzoda and M.-C. Amann, "GaSb and InP-based VCSELs at 2.3 μm emission wavelength for tuneable diode laser spectroscopy of carbon monoxide," *Proc. SPIE 7945, Quantum Sensing and Nanophotonic Devices VIII*, p. 794509, 2011.
- [66] A. Larsson, "Advances in VCSELs for Communication and Sensing," *IEEE Journal of Selected Topics in Quantum Electronics*, vol. 17, no. 6, pp. 1552-67, 2011.
- [67] D. Kang, S.-M. Lee, Z. Li, A. Seyedi, J. O'Brien, J. Xiao and J. Yoon, "Compliant, Heterogeneously Integrated GaAs Micro-VCSELs towards Wearable and Implantable Integrated Optoelectronics Platforms," *Advanced optical materials*, vol. 2, no. 4, pp. 373-81, 2014.
- [68] K. Ebeling, R. Michalzik and H. Moench, "Vertical-cavity surface-emitting laser technology applications with focus on sensors and three-dimensional imaging," *Japanese Journal of Applied Physics*, vol. 57, no. 852, 2018.
- [69] X. Yu, "Developments for Improved-Performance Vertical-Cavity Surface-Emitting Lasers," KTH Royal Institute of Technology, Stockholm, Sweden, 2014.
- [70] V. Jayaraman, J. Jiang, H. Li, P. J. S. Heim, G. D. Cole, B. Potsaid, J. G. Fujimoto and A. Cable, "OCT Imaging up to 760 kHz Axial Scan Rate Using Single-Mode 1310nm MEMS-Tunable VCSELs with >100nm Tuning Range," *CLEO:2011 - Laser Applications to Photonic Applications, OSA Technical Digest (CD) (Optical Society of America, p. paper PDPB2*, 2011.
- [71] V. Bardinal, T. Camps, B. Reig, D. Barat, E. Daran and J. Doucet, "Collective micro-optics technologies for VCSEL photonic integration," *Invited Review Article in Advances in Optical Technologies*, vol. 2011, no. Article ID 609643, 2011.
- [72] Z. D. Popovic, R. A. Sprague and G. A. N. Connell, "Technique for monolithic fabrication of microlens arrays," *Applied Optics*, vol. 27, no. 7, pp. 1281-84, 1988.
- [73] H. Ottevaere, B. Volckaerts, J. Lamprecht, J. Schwider, A. Hermanne, I. Veretennicoff and H. Thienpont, "Two-dimensional plastic microlens arrays by deep lithography with protons: fabrication and characterization," *Journal of Optics A Pure and Applied Optics*, vol. 4, no. 4, p. 354, 2002.
- [74] W.-C. Chen, T.-J. Wu, W.-J. Wu and G.-D. J. Su, "Fabrication of inkjet-printed SU-8 photoresist microlenses using hydrophilic confinement," *Journal of Micromechanics and Microengineering*, vol. 23, no. 6, p. 065008, 2013.
- [75] C. Croutxé-Barghorn, O. Soppera and D. J. Lougnot, "Fabrication of microlenses by direct photo-induced crosslinking polymerization," *Applied Surface Science*, vol. 168, no. 1-4, pp. 89-91, 2000.
- [76] G. Giuliani, S. Bozzi-Pietra and S. Donati, "Self-mixing laser diode vibrometer," *Measurement Science and Technology*, vol. 14, no. 1, pp. 24-32, 2003.

- [77] M. Nikolid, Y. L. Lim, K. Bertling, T. Taimre and A. D. Rakid, "Multiple signal classification for self-mixing flowmetry," *Applied Optics*, vol. 54, no. 9, pp. 2193-98, 2015.
- [78] [Online]. Available: <https://en.wikipedia.org/wiki/Zemax>.
- [79] R. Michalzik, *Vcsels: Fundamentals, Technology and Applications of Vertical-cavity Surface-emitting Lasers*, Springer, 2011.
- [80] S. Abada, "Conception et réalisation de microsystèmes optiques (MOEMS) en polymère pour l'optique adaptative intégrée sur diodes laser verticales (VCSELs)," Thesis, Université Toulouse 3 Paul Sabatier, Toulouse, 2015.
- [81] S. Abada, L. Salvi, R. Courson, E. Daran, B. Reig, J. Doucet, T. Camps and V. Bardinal, "Comparative study of soft thermal printing and lamination of dry thick photoresist films for the uniform fabrication of polymer MOEMS on small-sized samples," *Journal of Micromechanics and Microengineering*, vol. 27, 12 April 2017.
- [82] Y. Zhao, Q. Li, J.-B. Doucet, P.-F. Calmon, F. Mesnilgrete, B. Reig, C. Tronche, T. Camps, J. Perchoux and V. Bardinal, "Implementation of Integrated VCSEL-Based Optical Feedback Interferometry Microfluidic Sensor System with Polymer Microoptics," *Applied Sciences*, vol. 9, no. 24, p. 5484, 2019.
- [83] [Online]. Available: <http://www.microfab.com>.
- [84] V. Bardinal, E. Daran, T. Leichle, C. Vergnenegre, C. Levallois, T. Camps, V. Conedera, J.-B. Doucet, F. Carcenac, H. Ottevaere and H. Thienpont, "Fabrication and characterization of microlens arrays using a cantilever-based spotter," *Optics Express*, vol. 15, no. 11, pp. 6900-7, 2007.
- [85] G. Comina, A. Suska and D. Filippini, "PDMS lab-on-a-chip fabrication using 3D printed templates," *Lab Chip*, vol. 14, pp. 424-30, 2014.
- [86] G. Comina, A. Suska and D. Filippini, "Low cost lab-on-a-chip prototyping with a consumer grade 3D printer," *Lab Chip*, vol. 14, pp. 2978-82, 2014.
- [87] A. Accardo, R. Courson, R. Riesco, V. Raimbault and L. Malaquin, "Direct laser fabrication of meso-scale 2D and 3D architectures with micrometric feature resolution," *Additive Manufacturing*, vol. 22, pp. 440-6, 2018.
- [88] P. Dietrich, M. Blaicher, I. Reuter, M. Billah, T. Hoose, A. Hofmann, C. Caer, R. Dangel, B. Offrein, U. Troppenz, M. Moehrle, W. Freude and C. Koos, "In situ 3D nanoprinting of free-form coupling elements for hybrid photonic integration," *Nature Photonics*, vol. 12, pp. 241-7, 2018.
- [89] [Online]. Available: <https://www.laas.fr/projects/MultiFAB/>.
- [90] P. Debernardi, J. M. Ostermann and R. Michalzik, "VCSEL polarization control by monolithic surface gratings: a survey of modelling and experimental activities," *Proc. SPIE 7009, Second International Conference on Advanced Optoelectronics and Lasers*, no. 700903, 5 March 2008.
- [91] Q. Li, V. Raimbault, P. Menini, T. Camps and V. Bardinal, "Design and fabrication of a compact gas sensor integrating a polymer microresonator and a 850nm VCSEL source," in *22nd Photonics North Conference*, Vancouver, Canada, 2020.
- [92] B. Boisnard, "Conception et réalisation d'une source VCSEL accordable pour un microsystème d'analyse de la peau par Tomographie par Cohérence Optique (OCT)," Thesis, Toulouse University, Toulouse, 2019.
- [93] [Online]. Available: <http://www.adtekphotomask.com/>.
- [94] M. Diez, "Patterning and characterization of polymer nanostructures for optical biosensing," Thesis, Bordeaux University, Bordeaux, 2018.
- [95] [Online]. Available: https://www.microchemicals.com/products/photoresists/az_eci_3012.html.
- [96] Microchemicals, [Online]. Available: https://www.microchemicals.com/products/photoresists/az_nlof_2020.html.
- [97] [Online]. Available: https://www.microchemicals.com/micro/tds_az_nlof2000_series.pdf.

- [98] [Online]. Available: https://amolf.nl/wp-content/uploads/2016/09/datasheets_LOR_datasheet.pdf.
- [99] R. Heideman, M. Hoekman and E. Schreuder, "TriPleX-Based Integrated Optical Ring Resonators for Lab-on-a-Chip and Environmental Detection," *IEEE Journal of Selected Topics in Quantum Electronics*, vol. 18, no. 5, pp. 1583-96, 2012.
- [100] "Anti-reflective coatings," MicroChemicals, [Online]. Available: https://www.microchemicals.com/technical_information/anti_reflective_coating_photoresist.pdf.
- [101] A. Lecestre, P. Dubreuil, S. Noblecourt, J. Tasselli and e. al., "Anisotropic Deep Reactive Ion Etching without Aspect Ratio Dependence Etching for silicon power devices," in *PESM (Plasma Etch and Strip in Microtechnology)*, Grenoble, France, 2014.
- [102] P. Dubreuil and D. Quirion, "Mise au point d'un procédé de gravure d'aluminium sur oxyde de silicium dans la plateforme de micro et nanotechnologies du LAAS-CNRS," LAAS, Toulouse, France, 2019.
- [103] S. Mikhaylov, N. A. Ogurtsov, N. Redon, P. Coddeville, J.-L. Wojkiewicz and A. A. Pud, "The PANI-DBSA content and dispersing solvent as influencing parameters in sensing performances of TiO₂/PANI-DBSA hybrid nanocomposites to ammonia," *RSC Advances*, vol. 6, no. 86, p. 82625-34, 2016.
- [104] J. Stejskal and I. Sapurina, "Polyaniline: Thin films and colloidal dispersions (IUPAC technical report)," *Pure and Applied Chemistry*, vol. 77, pp. 815-26, 2005.
- [105] A. Riede, J. Stejskal and M. Helmstedt, "In-situ prepared composite polyaniline films," *Synthetic Metals*, vol. 121, pp. 1365-6, 2001.
- [106] A. AIROUDJ, "Étude de guides d'onde polymères fluorés par voie plasma et développement de nouveaux capteurs photoniques à base de polyaniline," L'UNIVERSITE DU MAINE , Le mans, 07 Décembre 2007.
- [107] I. Sapurina, A. Riede and J. Stejskal, "In-situ polymerized polyaniline films - 3. Film formation," *Synthetic Metals*, vol. 123, pp. 503-7, 2001.
- [108] N. Menegazzo, B. Herbert, S. Banerji and K. Booksh, "Discourse on the utilization of polyaniline coatings for surface plasmon resonance sensing of ammonia vapor," *Talanta*, vol. 85, p. 1369-75, 2011.
- [109] D. Williams, "Conduction and gas response of semiconductor gas sensors," in *Solid State Gas Sensors*, 1987, p. chapter 4.
- [110] M. Singh, J. Truong, W. Reeves and J. Hahm, "Emerging Cytokine Biosensors with Optical Detection Modalities and Nanomaterial-Enabled Signal Enhancement," *Sensors*, vol. 17, p. 428, 2017.
- [111] S. Kaya, P. Rajan, H. Dasari, D. C. Ingram, W. Jadwisieniczak and F. Rahman, "A systematic study of plasma activation of silicon surfaces for self-assembly," *ACS Applied Materials & Interfaces*, vol. 45, no. 7, pp. 25024-31, 2015.
- [112] J. Poon, L. Zhu, G. DeRose and A. Yariv, "Polymer microring coupled-resonator optical waveguides," *Journal of Lightwave Technology*, vol. 24, no. 4, p. 1843, 2006.
- [113] T. Toyosaki. [Online]. Available: https://en.wikipedia.org/wiki/Atomic_force_microscopy#/media/File:AFM_conf.jpg.

LIST OF FIGURES

Figure 1. a) Schematic of a planar micro-resonator implemented in Silicon On Insulator technology [7].
b) Illustration of high density integration of micro ring resonators on a 1x1 cm chip using the TriPlex technology [8]. 12

Figure 2. Schematic diagram of scattering attenuation of light in the air and the absorption attenuation of light in the glass fiber in the near infrared range. 13

Figure 3. Absorption spectra of common gas molecules. [11] 15

Figure 4. Two detection modes of microresonator sensors. [28]..... 17

Figure 5. a) Specific wavelengths trapped by the micro resonator light path circulation. b) The presence of target molecules at the surface of the micro resonator will lead to a red shift in the resonance mode. 18

Figure 6. Schematic view of the optical micro-sensor for compact gas sensing 22

Figure 7. Image of a VCSEL chip mounted on a TO-46 header..... 22

Figure 8. Chemical structure of amorphous CYTOP™ 24

Figure 9. Schematic diagram of manufacturing process of SU-8 grating coupler by using stepper. ... 24

Figure 10. Contact angle of deionized water on the CYTOP surface. a) Water droplet before Al treatment.
b) Water droplet after Al treatment..... 25

Figure 11. a) Polymer grating coupler, needs to etch the upper cladding leaving gratings unprotected.
b) Al metallic grating coupler, where the grating is protected by both the waveguide and upper cladding. 26

Figure 12. Chemical structure of SU-8. 27

Figure 13. General structure of polyaniline. The term y denotes the degree of oxidation of the material. 27

Figure 14. Absorption spectra of the polyaniline with (a) and without (b) gaseous ammonia. [57] 28

Figure 15. Schematic view of a typical GaAs vertical cavity surface emitting laser (VCSEL) with a short cavity length ($\sim 1\mu\text{m}$) and a small, buried oxide aperture ($\sim 4\mu\text{m}$) respectively leading to longitudinal and transverse single mode confinement and single mode operation. 34

Figure 16. Schematic view of integrated polymer micro lens on VCSEL arrays..... 36

Figure 17. Dimensions involved in microlens design 37

Figure 18. Illustration of ray tracing for VCSEL beam shaping in ZEMAX. 39

Figure 19. Single 850nm VCSEL chip with shallow etched grating at its surface (Trumpf). 40

Figure 20. Illustration of the two kinds of PCB used in this study: the previous version on the top (green PCB) with a conventional thickness of 1.57 mm, and an optimized, thinner version at the bottom (purple PCB) with a lower thickness of 0.8 mm to fit the constraints of the Nanoscribe tray..... 41

Figure 21. Image of the set-up used for VCSEL characterization (L-I-V and spectrum)..... 42

Figure 22. Measurement of polarization selection of the VCSEL emission as a function of the applied current. 43

Figure 23. Measurement of the evolution of the emission spectrum of a typical single mode VCSEL chip according to the applied current.	43
Figure 24. Procedure of VCSEL based micro-optical system fabrication. [82]	45
Figure 25. View of the VCSEL chip assembled on a PCB is sandwiched by two elastic films. A sufficient vacuum is used to imprint dry film on the non-planar sample. A temperature detector is used to control the temperature in the pressure chamber.	46
Figure 26. Polymer pedestals formed on mounted VCSEL chips on PCB by soft imprint of several DF films and direct laser writing.	47
Figure 27. Schematic diagram of the inkjet printing setup [83]	48
Figure 28. Pedestals array for calibration of lens thickness.	49
Figure 29. Measurement of semi-liquid dimension of micro lens by confocal microscope.....	50
Figure 30. Measurement by confocal microscopy of the reduction rate of heights of micro lens as function of the baking time and number of jetted droplets.	50
Figure 31. Micro lens fabricated by ink jetting on VCSEL chips and general view after wire bonding.	51
Figure 32. Micro lens fabricated by inkjet of commercial material Prielex SU-8.	52
Figure 33. Inclined pedestal surface caused by the surface flatness defects under VCSEL chip during assembly.....	52
Figure 34. WBR film forming a « protection wall » to ensure the verticality of DF pedestal.	53
Figure 35. L(I) curve of VCSEL with and without collimation micro lens.....	54
Figure 36. Measurement set-up of the beam divergence of single mode VCSELS	55
Figure 37. a) Intensity profiles measured with the beam profiler (I=3mA). b) Divergence of VCSEL with or without micro lens fabricated by inkjet writing.	56
Figure 38. Comparison of one-photon polymerization and two-photon polymerization.	57
Figure 39. Working diagram of the 2-photon polymerization Nanoscribe 3D printing machine. The substrate (here a VCSEL mounted onto a PCB) is dipped into the photoresist which is in direct contact with the objective lens.....	58
Figure 40. Different sample holders provided by Nanoscribe.....	59
Figure 41. a). 3D CAD representation of the pedestal and micro lens over a dummy VCSEL die, highlighting the dimensions of the micro optical components compared to the VCSEL. b). Illustration of the STL file mesh to be used for the Nanoscribe 2PP equipment, comprising 22284 faces and 11414 vertices.	61
Figure 42. Calibration of exposure parameters for Nanoscribe writing.	62
Figure 43. Micro pedestal and micro lens fabricated by 3D printing in three different slice resolutions.	62
Figure 44. View of a VCSEL chip with a 3D printed lens in single step before (a) and after (b) wire bonding.	63
Figure 45. VCSEL with a 3D printed lens and buried on a PCB with a wiring done before lens fabrication.	64

Figure 46. a) L(I) curve of VCSEL with and without 3D printed micro lens. b) Polarization-resolved L(I) curve of VCSEL with 2PP 3D printed micro lens.	64
Figure 47. a) Beam profiles without and without microlens measured at 3mA. b) Divergence of VCSEL with or without micro lens fabricated by 2PP 3D printing.....	65
Figure 48. Evolution of the emission spectrum of VCSEL with 3D printing micro lens according to the applied current	66
Figure 49. Schematic of the microresonator, including tapered waveguides, grating couplers and a vertically coupled microring.	71
Figure 50. The 3-layer planar waveguide and its associated relative wave vectors.	72
Figure 51. Dispersion curves@850nm of TE_n and TM_n modes in a three-layer structure CYTOP/SU-8/CYTOP versus the guiding layer thickness.....	74
Figure 52. Top view of the guiding plane.....	74
Figure 53. Dispersion curves at 850nm of TE_{xm} and TM_{xm} modes in a three-layer structure CYTOP/SU-8/CYTOP. The thickness of layer SU-8 is less than 800nm.....	75
Figure 54. Schematic diagram of a simulated output grating coupler.	76
Figure 55. Schematic of the model simulated with Lumerical, showing the two input sources, and the position of the two detectors used in the simulation to optimize both output (Source 1 + Detector 1) and input (Source 2 + Detector 2) grating couplers.	77
Figure 56. Coupling efficiency of the grating coupler versus waveguide thickness.	78
Figure 57. The influence of the dimension ratio between light spot and grating coupler on coupling efficiency.....	79
Figure 58. Taper guide transmission efficiency as a function of the length to width ratio.....	80
Figure 59. Quantized resonance modes of a conventional micro resonator besides a mono-mode waveguide	81
Figure 60. Energy coupling schematic between a waveguide and a lateral micro resonator.....	82
Figure 61. Energy coupling curve of a micro resonator system for different gaps.	83
Figure 62. The variation of coupling efficiency versus CYTOP bottom cladding thickness.	83
Figure 63. Top view and side view of the detection area of the microsystem.....	84
Figure 64. Illustration of the size reduction from the reticle to the exposed wafer. Here the reticle features are designed at scale 5, and the reticle contains 9 patterns. [93]	85
Figure 65. Schematic representation of the five over nine areas available on the reticle. Each pattern will cover a 6.2x7.2mm ² on the wafer. A complete micro-resonator will be a combination of three areas of the reticle. Note: the polarity is not respected for better graphic rendering of the schematic.....	86
Figure 66. The small squares added on the corner in the simulation.	87
Figure 67. Simulation results obtained with GenISys for different additional square size and overlap with the waveguide extremity. The best configuration obtained at 0 μ m overlap and 0.2 μ m square size is highlighted.....	87
Figure 68. Resolution patterns.	91
Figure 69. Gradually baking process of CYTOP polymer.	94
Figure 70. First approach adopted for manufacturing the aluminum grating couplers.	95

Figure 71. a) Wave shaped ECI stripes after photolithography. b) Uneven pattern of grating coupler after photolithography.....	97
Figure 72. Bubbles that appear at the Al-CYTOP interface due to heating.....	97
Figure 73. Irregular aluminum grating coupler lines after wet etching.....	98
Figure 74. Aluminum grating coupler after Plasma etching.....	99
Figure 75. The manufacturing process flow of lift-off method.....	99
Figure 76. Coating thickness of nLOF 2000 series photoresists versus spin speed. [97].....	100
Figure 77. a) nLOF grating couplers after photolithography, without formed undercut. b) The evaporated Al forms a slice of film rather than separated stripes after etching.....	101
Figure 78. Aluminium grating couplers fabricated by lift-off process.....	102
Figure 79. Aluminium grating couplers with residuals of aluminium lines.....	102
Figure 80. Normal undercut form and functional interchangeable two-layer form for lift-off process.....	103
Figure 81. Distribution of different doses of exposure on the wafer during photolithography for the LOR+ECI lift-off process optimization.....	104
Figure 82. Underexposed (a) and overexposed (b) patterns of grating coupler after development....	104
Figure 83. Damage to the pattern of grating coupler caused by the flushing pressure from the machine of development.....	105
Figure 84. a) Grating coupler patterns in LOR+ECI obtained after photolithography with exposure doses between 1000 to 1100 J/m ² . b) Aluminium grating coupler obtained after completion of the lift-off process.....	105
Figure 85. Distortions and misalignments of SU-8 waveguides on CYTOP lower cladding.....	107
Figure 86. Upper left: SEM wide view of the tapered waveguide and the grating coupler realized over a CYTOP cladding. Upper right: Close-up view of the waveguide at its thinnest section (1µm width). Bottom: Tilted SEM image at the edge of the taper, highlighting the smoothness of the surface despite the presence of the Al grating coupler.....	108
Figure 87. a) Waveguide exit port by regular photolithography. b) Waveguide exit port improved by GenISys design.....	109
Figure 88. Typical configuration of an AFM.....	110
Figure 89. CYTOP surface before/after plasma oxygen etching.....	111
Figure 90. Two-point pressing method for wafer cutting without damaging the patterns.....	112
Figure 91. Optical bench for the characterization of the grating couplers.....	113
Figure 92. Incident light on the input grating (left) and output light obtained on the output grating (right) with an SU-8 waveguide covered on CYTOP lower cladding.....	114
Figure 93. The incident light reflected on the substrate has nearly the same intensity as before, it will interfere the final resolution of the photoresist pattern (a), while using an anti-reflective coating (BARC) on the substrate will markedly minimised this effect, to keep the final pattern as neat as possible....	116
Figure 94. Schema of plasma etching.....	117
Figure 95. ECI patterns after plasma etching, a) with electrostatic clamping to the substrate holder, and b) with thermal conductive adhesive on the substrate holder. The roughness after etching is much lower in b).....	118

Figure 96. Process workflow for the fabrication of Al grating couplers over the SiO ₂ lower cladding.	118
Figure 97. For the same material, the etch rate is lower on a smaller pattern during the plasma etching.	119
Figure 98. A 30s over etching time does not affect too much on the profile and duty cycle of pattern. a) Over etching time is 30s. b) Over etching time is 90s.	120
Figure 99. a) Protrusions appear next to grating coupler lines and pull the patterns to be distorted. b) A re-added plasma O ₂ disperse the residues and contaminates the surface of sample.	121
Figure 100. Grating coupler before stripping. a) A deionized water flow is used to avoid residue bumps. b) A chaining oxygen plasma without interruption of vacuum is used to avoid the formation of residue.	122
Figure 101. Illustration of the damages caused by (a) an ultrasonic bath with PG remover and (b) oxygen plasma on the nanometric features of the grating couplers.	123
Figure 102. Al grating coupler fabricated by plasma etching and then stripped by UV-Ozone.	123
Figure 103. Improved optical bench for characterization of components.	124
Figure 104. Upgraded optical bench for characterization of components.	125
Figure 105. Normalized coupling rate of semi-manufactured wafer for the performance testing of upgraded optical bench.	126
Figure 106. PANI undergoes a deprotonation process upon NH ₃ exposure [103].	129
Figure 107. The evolution in the thickness of the PANI layer, deposited on Si, SU-8 and glass substrates over deposition time.	131
Figure 108. PANI coating produced in situ without (a,b) /with (c,d) an agitation of 80rpm.	132
Figure 109. SU-8 surface without (a) / with (b) PANI coating.	133
Figure 110. PANI coating on SU-8 waveguide which is deposited on the CYTOP lower cladding. a) PANI is coated by method in-situ. b) PANI is coated by method spin coating.	133
Figure 111. UV-VIS absorption spectra of PANI coated glass substrates upon different exposure times to NH ₃ and NH ₄ OH. Inset focuses on the absorbance variation around 850 nm.	134
Figure 112. a) CAD rendering of the fully integrated optical gas sensor. b) Exploded view showing the alignment pins, the microring resonators chip, and the VCSEL optical window.	136
Figure 113. a) Detailed view of the collimated VCSEL matrix and the grating couplers observed from the bottom (through the Si substrate). b) Close-up view of the optical port showing the input grating couplers area, and the exposed sensing area with the microring resonators. A built-in slope of 19° ensures the injection angle is guaranteed.	136

LIST OF TABLES

Table 1. Materials involved in various optical waveguide gas sensors	19
Table 2. Initial design conception for microsystem.	29
Table 3. Wavelengths of several major Fraunhofer lines.....	37
Table 4. Optimal lens geometry configurations of different pedestal heights retrieved by ZEMAX optimization [9].....	38
Table 5. Comparison between main additive manufacturing technologies for polymeric materials (adapted from Nanoscribe Whitepaper “Additive manufacturing based on two-photon polymerization”).	57
Table 6. Comparison of different objects of Nanoscribe	60
Table 7. Comparison of performances between both methods	67
Table 8. Fabrication process of ECI protection pattern	96
Table 9. Fabrication process of Al grating couplers with nLOF dilution solution by lift-off method.	101
Table 10. Fabrication process of grating coupler by double layer lift-off method.	103
Table 11. Fabrication process of SU-8 waveguide and taper.....	106
Table 12. Fabrication process of grating coupler with relevant parameters.	119
Table 13. Etching parameters during ICP-RIE.....	119
Table 14. Selection of SEM characterization images after the stepper exposure and the ICP-RIE etching each step during the fabrication process. The duty cycle of grating coupler decreases as dose of stepper increases.....	121

